Tidal Evolution of Dwarf Spheroidal Satellites

by

Alexandra Borukhovetskaya
B.Sc., University of Wisconsin - Madison, 2019

A Dissertation Submitted in Partial Fulfillment of the
Requirements for the Degree of

DOCTOR OF PHILOSOPHY

in the Department of Physics and Astronomy

Tidal Evolution of Dwarf Spheroidal Satellites

by

Alexandra Borukhovetskaya
B.Sc., University of Wisconsin - Madison, 2019

Supervisory Committee

Dr. J. Navarro, Supervisor
(Department of Physics and Astronomy)

Dr. A. McConnachie, Departmental Member
(Department of Physics and Astronomy)

Dr. L. Rosenberg, Outside Member
(Department of Chemistry)

ABSTRACT

Dwarf spheroidal galaxies populate the faintest end of the galaxy luminosity function and yet they apparently reside in massive dark matter halos. With mass-to-light ratios as high as $M/L \sim 10^4$, they are the key to understanding the nature of dark matter on galactic scales. Of particular interest are nearby dwarf spheroidals that appear at odds with predictions from ΛCDM, the standard model of cosmological structure formation. These are galaxies which exhibit unusually large sizes and low line-of-sight velocity dispersions, suggestive of surprisingly underdense dark matter halos, perhaps occurring as a result of tidal interactions with the Milky Way.

In this dissertation I present a detailed study of three carefully selected such cases: the Fornax, Crater II and Antlia II dwarf spheroidal satellites of the Milky Way. Fornax is chosen for its relatively low mass-to-light ratio, which is suggestive of a lower mass halo than indicated by abundance matching. Crater II and Antlia II, termed 'feeble giants', are both chosen for their particularly low values of velocity dispersion, which are especially anomalous given their large half-light radii and low luminosities. Using N-body simulations, we investigate the evolution of these objects under the effects of Galactic tides imparted by the Milky Way potential.

Our study leads us to conclude that the low measured velocity dispersions of these dwarf galaxies are indeed consistent with a tidal interpretation in the context of predictions put forth by cosmological simulations of the Local Group and recent measurements of the galaxies' sky positions, proper motions, distances, and radial velocities. The large sizes of Crater II and Antlia II are much more difficult to reconcile in this scenario, however these are still possible to reproduce under the effect of Galactic tides, provided that initially the stellar binding energy distributions had a minimum "cutoff". Such a limit, which may have been imposed by baryonic effects during the formation of the galaxy, or by the presence of a constant density dark matter core, leads to transient stages with large sizes and low velocity dispersions comparable to those of Crater II and Antlia II. Detailed observations of galaxies' density profiles, corresponding logarithmic slopes, and velocity dispersion profiles may help provide insight into the likelihood of such a formation scenario for Crater II, Antlia II, and the emerging population of other feeble giant galaxies.

Contents

List of Tables

List of Figures

ACKNOWLEDGEMENTS

It is difficult to adequately express the extent of the joined labour and effort that over the course of many years compounded this dissertation. It is more difficult still to express my immense gratitude to those without whose support this work would fail to exist. Nevertheless, I will try.

First and foremost, I would like to extend my utmost thanks to my advisor, Julio Navarro, for his unyielding support, wise counsel, and patient guidance throughout my doctorate. From him I have learned a tenacity and unique mindset that have given me strength and confidence both in research and in life.

A thousand and one thanks to Raphaël Errani, whose unfaltering kindness, confidence, and mentorship supported me through countless times of struggle. Above all, thank you for always seeing the scientist in me, even when I myself did not.

My thanks to Azi Fattahi, from whom I learned much. Thank you for your many words of encouragement and support, and for being a role model to me in the early days of my graduate program.

My eternal love and gratitude to my friends. To Bobby, Rory, Nic, Mallory, and Ryan, for laughing in the good times, commiserating in the bad, and believing in me through it all. To Doug, for being my anchor in the storm. And last, but not least, to Lisbon and Michael, who have known me since long before I decided to become a scientist, and have loved me throughout.

And finally, a list of acknowledgements would never be complete without including my parents, Witek and Marina, who nurtured my curiosity for the world from a young age and always helped me with my math homework.

О сколько нам открытий чудных
Готовят просвещенья дух
И опыт, сын ошибок трудных,
И гений, парадоксов друг,
И случай, бог изобретатель.

А. С. Пушкин - 1829

Chapter 1

Introduction

The leading theory for gravity - Einstein's theory of general relativity - fails to reproduce the motion of stars and gas on galactic scales when accounting for observable matter alone. This led to the idea that the Universe is composed of both ordinary 'baryonic' matter and an unseen second component, *dark matter* (DM), which dominates over baryonic matter on cosmological scales, at least 1:5. Our current understanding of cosmology relies on dark matter as the dominant matter component in regulating the expansion of the Universe and playing an essential role in the formation and evolution of the structure we observe today.

1.1 The standard model of cosmology

The broad objective of cosmology is to develop a mathematical model to describe the various observed properties of the Universe. The standard model of cosmology, Λ Cold Dark Matter (ΛCDM) characterises dark matter as essentially 'cold' and 'dark', i.e. the particle making up dark matter is assumed to interact only gravitationally and was already non-relativistic at the time of its decoupling.

1.1.1 Hierarchical assembly and galaxy formation

In ΛCDM, matter forms structure through gravitational collapse, echoing in pattern the primordial density fluctuations of the early universe. Small clumps of cold dark matter form and interact with one another, merging to form a hierarchy of haloes and subhaloes. Galaxies form subsequently from gas which is accreted onto and cools in the deep potential wells of these dark matter haloes (White and Rees, 1978). The formation of structure

in a cold dark matter universe, then, may be thought of as a 'bottom-up' process, where the smallest structures combine to form the largest structures. Consequently, large haloes are often host to a rich substructure of smaller dark matter clumps, or 'subhaloes', which have been accreted onto their larger host halo and are in the process of coalescing.

1.1.2 Dark matter halo density profiles

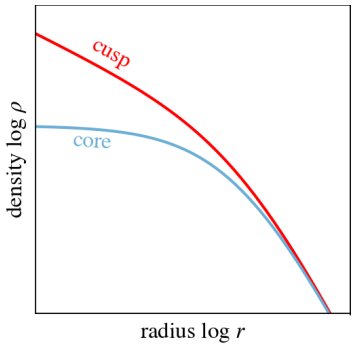

Figure 1.1: Illustration of centrally divergent, 'cuspy' (red) and constant density, 'cored' (blue) dark matter density profiles.

The structure of the resulting dark matter haloes is roughly spherical and their density is well parametrised by the centrally cuspy Navarro et al. (1997) (hereafter NFW) profile,

$$\rho_{\rm NFW}(r) = \frac{\rho_{\rm s}}{(r/r_{\rm s})(1+r/r_{\rm s})^2}, \tag{1.1}$$

which goes as $\rho \propto r^{-1}$ at small radii and $\rho \propto r^{-3}$ at large radii. Here, $r_{\rm s}$ denotes a scale radius, and defining $M_{\rm s}$ as the mass enclosed within $r_{\rm s}$, with

$$M(<r) = 4\pi\rho_{\rm s} r_{\rm s}^3[\ln((r+r_{\rm s})/r_{\rm s}) - r/(r_{\rm s}+r)], \tag{1.2}$$

the scale mass and density are related by

$$M_{\rm s} = 4\pi\rho_{\rm s} r_{\rm s}^3[\ln(2) - 1/2]. \tag{1.3}$$

This profile is fully specified by two parameters; in equation 1.1 the profile is written in terms of the scale radius and scale density, however one may also write the above in terms of a virial mass[1], M_{200}, and concentration, $c \equiv r_{200}/r_{\rm s}$, or, alternatively, by a maximum circular velocity, $V_{\rm max}$, and the radius at which it is reached, $r_{\rm max}$. These are related as $V_{\rm max} \approx 1.64 r_{200}/c\sqrt{G\rho_{\rm s}}$, where r_{200} is the the radius containing M_{200}. The maximum circular velocity is often used as an analogue for the mass of the dark matter halo, and due to the nature of galaxy assembly, correlates strongly with the stellar mass, $M_\star$, of the galaxy it is host to. This correlation between stellar and halo mass is recovered by many cosmological simulations; throughout our study we rely on the results for isolated galaxies from the APOSTLE suite of Local Group simulations (Fattahi et al., 2018), detailed in chapter 2. The advantage of using simulations for this purpose is that they track the

[1]We define virial quantities as those within a sphere of mean density equal to 200 times the critical density for closure, $\rho_{\rm crit} = 3H_0^2/8\pi G$

evolution of galaxies and halos across time, providing positions, velocities, star formation histories and other physical properties for each system. However, some of our best constraints on the stellar mass-halo mass relation, particularly at the faint end, come from abundance-matching techniques, where galaxies of given stellar mass are linked to their dark matter halos by matching observed galaxy luminosity functions to simulated halo mass functions assuming a unique and monotonic relation between galaxy luminosity and halo mass (Conroy et al., 2006; Guo et al., 2010; Behroozi et al., 2013).

Galaxies are born as gas falls into the deep gravitational potential well of its dark matter halo where it is able to cool and form stars. The central accumulation of baryonic material may have an effect on the density profile of a dark matter halo. The condensation of baryons within a dark matter halo may also pull the dark matter inwards, leading to a more centrally concentrated dark matter distribution (Gnedin et al., 2004). Alternatively, gravitational heating through baryonic substructures (see, for e.g., Nipoti and Binney, 2015) and violent or repeated supernova feedback (Navarro et al., 1996a; Read and Gilmore, 2005a; Pontzen and Governato, 2012; Di Cintio et al., 2014; Oñorbe et al., 2015) may serve to dissolve central density cusps, forming a central constant-density core (see fig. 1.1).

1.2 Dwarf galaxies and the Local Group

The Local Group is a grouping of nearby galaxies, which includes our own Milky Way (MW) galaxy, its closest massive neighbour, Andromeda (M31), and over a hundred fainter dwarf galaxies within a region of radius ~ 2 Mpc. The Local Group is a relatively isolated and gravitationally bound system, where the Milky Way and Andromeda are in the process of approaching one another in their first orbit (Li and White, 2008).

Within the Local Group, dwarf spheroidal galaxies (dSph), with luminosities spanning between $10^2 \lesssim L/L_\odot \lesssim 10^8$, constitute the majority of Milky Way satellites. These objects include in their ranks the faintest and most dark matter dominated (dynamical mass-to-light ratios of up to $\langle M/L \rangle \sim 10^4$) systems known to date, and the latter is exactly what makes them so perfectly suited to studies of the properties of dark matter on kpc scales (McConnachie, 2012; Simon, 2019).

DSph galaxies are also notably devoid of gas, exhibit little to no sign of rotational support, and are mainly composed of old stars with very few signs of recent or ongoing star formation. The preferential clustering of dSphs[2] near massive objects, such as the

[2]With some exceptions, for example Cetus and Tucana, which are located far from both the Milky Way

giant spirals of the Local Group, offers insight into the formation paths which gave rise to these gas-poor objects. The effect of a larger galaxy in close proximity is to not only shield nearby dSphs from accretion of any intergalactic material that may be used to fuel star formation, but also to strip any existing gas through tidal effects and ram-pressure stripping[3].

The luminosities and velocity dispersions of dSph galaxies are comparable to globular clusters, but these objects differ significantly, mainly on account of the large amounts of dark matter present in dSphs and lacking in globular clusters. Unfortunately, because of their low luminosities, studies of dSphs are limited almost exclusively to the Local Group. However, with continuously improving photometric and spectroscopic surveys, recent years have seen discoveries of increasingly faint Milky Way dwarfs and a more complete picture of dwarf positions and kinematics. The availability of this data puts us in the privileged position of being able to examine in detail the current properties of these unique objects as well as to extend our analysis to probe their evolutionary histories and the nature of dark matter itself.

1.2.1 Mass estimators

Estimates for the dynamical masses for objects such as dwarf spheroidals arise as a result of manipulating the virial theorem or the Jeans equation for a collisionless, dispersion-supported, spherically symmetric system in equilibrium. Defining the anisotropy parameter[4] as

$$\beta = 1 - \frac{\bar{v_\theta^2} + \bar{v_\phi^2}}{2\bar{v_r^2}}, \tag{1.4}$$

the Jeans equation may be manipulated into an estimate for the enclosed mass of the system:

$$M(<r) = -\frac{r\bar{v_r^2}}{G}\left(\frac{d\ln\nu}{d\ln r} + \frac{d\ln\bar{v_r^2}}{d\ln r} + 2\beta\right), \tag{1.5}$$

where ν is the spatial number density of particles and $\bar{v}$ refers to the mean of the squares of their velocity components. Wolf et al. (2010) show that for each dispersion-supported

and M31 likely as a result of ejection onto a highly energetic orbit following multiple satellite accretion into the Local Group (Sales et al., 2007; Ludlow et al., 2009; Santos-Santos et al., 2023)

[3] As a satellite orbits through the hot atmosphere of a host halo, it may experience ram pressure forces which are capable of efficiently stripping away the hot atmospheres of satellite galaxies, a mechanism termed ram pressure stripping.

[4] This parameter ranges $-\infty \leq \beta \leq 1$. The system is isotropic when $\beta = 0$, radially biased when $\beta > 0$, and tangentially biased when $\beta < 0$.

galaxy, there exists a radius where the enclosed mass of the system is insensitive to the anisotropy parameter[5], allowing one to derive a 'mass estimator' which gives the mass enclosed within this radius,

$$M_{1/2} = 3G^{-1}\langle\sigma^2_{\rm los}\rangle r_{1/2}, \tag{1.6}$$

where this radius is taken to be $r \sim r_{1/2}$ ($r_{1/2}$ is the 3D deprojected half-light radius) and $\langle\sigma^2_{\rm los}\rangle$ is the luminosity-weighted square of the line-of-sight velocity dispersion (see also, Walker et al., 2009; Errani et al., 2018). Inserting the above into the definition of the circular velocity, $V_c^2 = GM/r$, one may additionally obtain a simple expression to estimate the circular velocity at the half-light radius:

$$V_{1/2} = \sqrt{\frac{GM_{1/2}}{r_{1/2}}} = \sqrt{3}\sigma_{\rm los}. \tag{1.7}$$

Interestingly, galaxies in the Local Group exhibit a wide range of velocity dispersions, which when applying to equation 1.7, appear to indicate that they are hosted within dark matter haloes that are far less massive than we expect given their respective stellar masses (as described in section 1.1.2) (McConnachie, 2012; Fattahi et al., 2018).

1.3 Tidal interactions of subhaloes and dSphs

This thesis focuses on the evolution of satellite galaxies and subhaloes in the presence of a larger host galaxy - the Milky Way. The following sections discuss the dynamical effect a host potential such as this may have on nearby satellites.

1.3.1 Dynamical friction

When an object, such as a dwarf galaxy, moves within a background density field, it experiences a drag force opposite of its direction of motion. Analytically, this process is approximately described by Chandrasekhar (1943): for a mass M moving in a homogeneous background medium, in the limit where the mass under consideration is far greater than the mass, m, of the objects composing the background density field, the effect on

[5]Notably, the anisotropy of a system is very difficult to measure, and the dependence of equation 1.5 on this parameter, along with the mass density of the system, gives rise to the famous *mass-anisotropy degeneracy*.

the primary object may be written as

$$\frac{d\mathbf{v}_M}{dt} = -\frac{4\pi \ln\Lambda G^2 \rho M}{v_M^3}\left[\mathrm{erf}(X) - \frac{2X}{\sqrt{\pi}}e^{-X^2}\right]\mathbf{v}_M. \tag{1.8}$$

Here, $\ln\Lambda$ is the Coulomb logarithm[6], ρ is the overall background density, and $X \equiv v_M/(\sqrt{2}\sigma)$, where σ is the dispersion of the homogeneous Maxwellian distribution of background velocities. Over time, this drag force will cause satellites to decelerate and sink closer to the centre of their hosts, the timescale of which depends strongly on the velocity of the sinking object, its mass, and the density of the background medium, as illustrated in equation 1.8. This process plays a central role in several phenomena, including the orbital decay of globular clusters, the evolution of supermassive black holes in merging galaxies, and the eventual orbital decay of satellites such as the Magellanic Clouds.

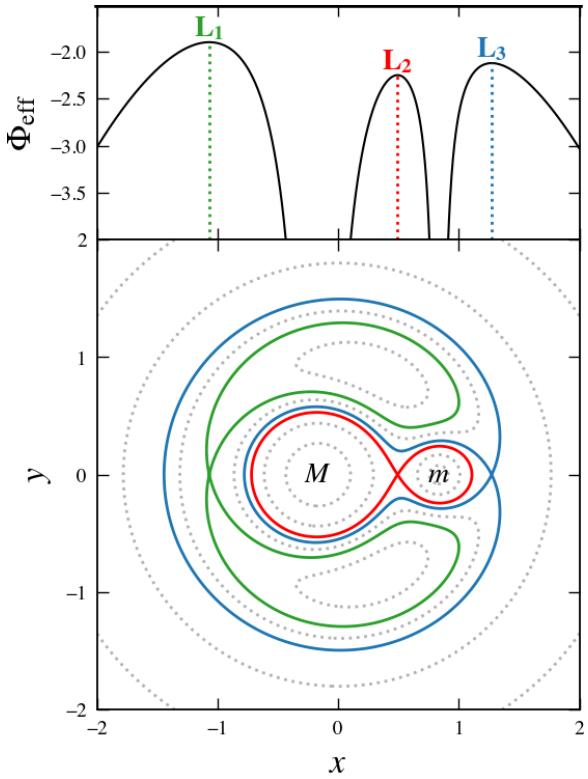

Figure 1.2: *Top:* Effective potential for a point mass m orbiting in a circular orbit around a larger point mass M, where $M = 5m$. Three Lagrange points, L_1, L_2, L_3, are labelled. *Bottom:* Contours of equal effective potential. Separatrices corresponding to $\Phi_{\rm eff}(L_1)$, $\Phi_{\rm eff}(L_2)$, and $\Phi_{\rm eff}(L_3)$ are shown in colour.

1.3.2 Tidal stripping

As satellites orbit in proximity of a host galaxy, they experience the effects of tidal forces due to the gradient of the gravitational potential across the satellite. As a consequence to these tidal forces, the orbiting satellite may lose matter - a phenomenon termed *tidal stripping*. The strength of the tidal forces and the satellite's susceptibility to mass loss increase with greater proximity to the centre of the host. As such, dynamical friction often works in congruence with tidal stripping, drawing satellites onto smaller orbits where they are more sensitive to tides. The influence of tides depends also on the structure of the host and satellite. The effective potential,

[6]The Coulomb logarithm refers to the logarithm of the ratio between the maximum and minimum impact parameters of the encounters between the primary object and the background particles.

Φ_{eff}, can be written in terms of the potential, Φ, of the system and the angular momentum, L_z:

$$\Phi_{\text{eff}} \equiv \Phi(R,z) + \frac{L_z^2}{2R^2}. \tag{1.9}$$

Figure 1.2 shows contours of constant effective potential, for a system of two orbiting point masses in a circular orbit, one of mass m and the other of mass $M = 5m$. The Lagrange points (the first three of which are labelled in this figure as L_1...L_3[7]) correspond to the extrema of this surface. Particles orbiting here are restricted to regions where $E_{\text{J}} > \Phi_{\text{eff}}$[8] and the curves bounding these areas are called the zero-velocity curves, as in the rotating frame where the two particles are at rest, orbits can only reach these curves if their velocities in the (R,z) plane are instantaneously zero. Note in figure 1.2 that near each of the two bodies, the zero-velocity curves are centred on each of the bodies, while further away from the system, the curves surround both masses. The location of L_2 aligns with the last closed zero-velocity curve to surround m, and as such, the distance from m to L_2 marks the radius r_J within which particles are considered bound to the satellite. The radius r_J, called the Jacobi radius[9], is evaluated to be

$$r_J = \pm\left(\frac{m}{3M}\right)^{\frac{1}{3}} D, \tag{1.10}$$

where D is the distance between the two point masses. Though not a perfect analogue, r_J may be used as a reasonable estimate of where one might expect a star orbiting a satellite to become unbound.

Because systems of orbiting satellites are extended, rather than point masses, equation 1.10 is often rewritten to relate the mean density of the satellite within a 'tidal radius', r_{t}, to the mean density of the host within the satellite's pericentre:

$$\langle \rho_{\text{satellite}} \rangle_{\text{r}_{\text{t}}} = 3 \langle \rho_{\text{host}} \rangle_{\text{r}_{\text{peri}}} \tag{1.11}$$

(Peñarrubia et al., 2008).

Systems on eccentric orbits that pass in close proximity to dense regions of the Galaxy experience a strong tidal shock and may lose a significant fraction of mass with each pericentre passage. Particles that become unbound escape primarily through the L_2 or L_3 points and form a leading or trailing *tidal tail* respectively, and depending on the orbit may

[7] Note that different authors use different conventions for the numbering of the Lagrange points.
[8] E_{J} is the Jacobi integral, which in this case may be written as $E_{\text{J}} = v^2/2 + \Phi_{\text{eff}}(\mathbf{x})$
[9] Also Jacobi limit, Hill radius, and Roche radius.

go on to form another tidal feature called a shell. Presence of tidal features such as tails surrounding an observed galaxy is a strong observational indicator that a galaxy has been stripped by its host halo. In addition, tidal shocks, though relatively brief, leave potentially observable, transient features in the outer density profile of the bound satellite remnant. At pericentre, particles in the satellite system get a kick in energy and are boosted onto new, less bound (or even unbound) orbits. As the satellite moves away from pericentre and gradually relaxes, these outward-moving particles form an excess (illustrated in figure 1.3) outside the radius where the local crossing time equals the time elapsed since pericentre. In projection, this radius, termed the break radius, R_b, is defined by Peñarrubia et al. (2009) as

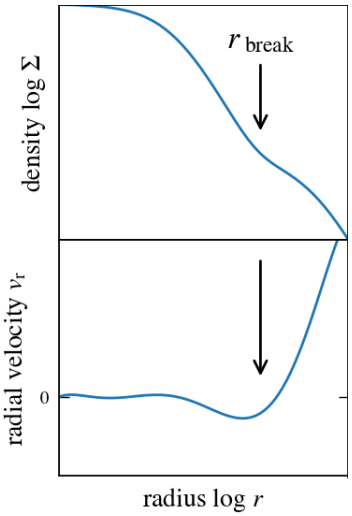

Figure 1.3: Illustration of break radius in sample profiles of density and radial velocity.

$$R_b = C\sigma_0(t - t_p), \tag{1.12}$$

where σ_0 is the central line-of-sight velocity dispersion, $t - t_p$ is the time elapsed since pericentre, and C is a constant measured empirically to be 0.55 ± 0.03. In essence, the break radius marks the location at which the system transitions from a region where equilibrium has already set in to a region still dominated by the outward motion of particles that gained energy during the pericentric passage. With time, as the particles continue to move outward, the location of the break radius will move further out into the outskirts of the satellite, becoming gradually more and more difficult to detect.

1.4 Numerical modelling

The formation and evolution of structure is a highly nonlinear process and thus numerical simulations play an essential role in studies of galaxy structure and formation. Numerical methods are likewise critical on smaller scales, such as modelling the orbital evolutions of $N > 2$ particles, for which there is no generalised theoretical description. These simulations do not include hydrodynamics, radiative processes or models for galaxy formation; the only force under consideration is gravity acting on collisionless cold dark matter particles. This is appropriate for the case of dwarf galaxies since they are dark matter dominated and typically devoid of gas.

For the purpose of my dissertation, I treat the Milky Way host as a static and analytic

potential and each individual dSph satellite as a full N-body system. N-body particles here represent dark matter, and stars are 'painted' over the existing dark matter particle distribution, without adding additional N-body particles. In the case of Fornax, where we study also its globular clusters, each globular cluster is modelled as an additional N-body particle with the appropriate corresponding mass. Details of the implementation are given below.

1.4.1 *GADGET-2*

GADGET-2 is a massively parallel TreeSPH code designed for simulating the dynamics of gravitating astrophysical systems, computing gravitational interactions using hierarchical multipole expansion and gas dynamics by means of the smoothed particle hydrodynamics (SPH) method (Springel, 2005). SPH is based on the idea of representing a fluid as a collection of tracer particles, each with a set of properties such as mass, position, velocity, and other fluid properties such as density, pressure, and viscosity. These particles interact with each other via a smoothing kernel that allows for a smooth and continuous representation of the fluid. To achieve necessary spatial adaptivity, GADGET-2 uses a hierarchical multipole expansion approach, often termed a tree algorithm. This method works by dividing the particles in the system into groups, and then approximating the interactions between the groups using multipole expansions. The groups are then divided into subgroups, and the process is repeated until a sufficient level of accuracy is achieved. Modelling forces using tree algorithms has the computational advantage of requiring only $\mathcal{O}(N \log N)$ interactions (Barnes and Hut, 1986), or more recently $\mathcal{O}(N)$ (Dehnen, 2002), compared to the $\mathcal{O}(N^2)$ required were we to compute the force with a direct-summation approach.

1.4.2 Host model

In the numerical simulations run with GADGET-2 for chapters 2, 3, and 4, the Milky Way host galaxy potential is represented as a static, analytical model composed of three components: a spherical bulge, a two-component axisymmetric disk, and a spherical dark matter halo. These components are parametrised with Hernquist (1990), Miyamoto and Nagai (1975), and Navarro et al. (1997) models, respectively, with specific parameters of each component chosen such that the total potential ($\Phi_{\rm MW}(R,z) = \Phi_{\rm bulge}(r) + \Phi_{\rm disk}(R,z) + \Phi_{\rm halo}(r)$) approximates that which is estimated for the Milky Way by McMillan (2011). These parameters are summarised in table 1.1.

1.4.2.1 Bulge

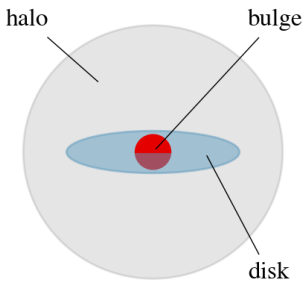

Figure 1.4: Illustration of the three components of the Milky Way host potential modelled.

The Hernquist (1990) bulge potential is written in terms of a scale radius a and total mass M:

$$\Phi_{\rm bulge}(r) = -\frac{GM}{r+a}$$

1.4.2.2 Disk

The two-component disk is modelled as a combination of a Miyamoto and Nagai (1975) thin and thick disk. These are written in terms of a scale length a, scale height b, and total mass M of each disk:

$$\Phi_{\rm disk}(R,z) = -GM\left[R^2 + (a+\sqrt{b^2+z^2})^2\right]^{-1/2}$$

1.4.2.3 Halo

The Milky Way dark matter halo is written here as an NFW profile with a scale radius and scale mass:

$$\Phi_{\rm halo}(r) = -\frac{GM_{\rm s}}{r}\frac{1}{\ln(2)-\frac{1}{2}}\ln\left(1+\frac{r}{r_{\rm s}}\right)$$

Table 1.1: Parameters of the analytical, static Milky Way potential used in this study. The model is a spherical re-parametrisation of the McMillan (2011) model, as discussed in Errani and Peñarrubia (2020).

Component	Functional form			
Disk (thin)	Miyamoto and Nagai (1975)	$M = 5.9\times10^{10}\,\mathrm{M}_\odot$	$a_{\rm d} = 3.9\,\mathrm{kpc}$	$b_{\rm d} = 0.31\,\mathrm{kpc}$
Disk (thick)	Miyamoto and Nagai (1975)	$M = 2.0\times10^{10}\,\mathrm{M}_\odot$	$a_{\rm d} = 4.4\,\mathrm{kpc}$	$b_{\rm d} = 0.92\,\mathrm{kpc}$
Bulge	Hernquist (1990)	$M = 2.1\times10^{10}\,\mathrm{M}_\odot$	$a = 1.3\,\mathrm{kpc}$	
DM Halo	Navarro et al. (1997)	$M_{200} = 1.15\times10^{12}\,\mathrm{M}_\odot$	$r_{\rm s} = 20.2\,\mathrm{kpc}$	$c = r_{200}/r_{\rm s} = 9.5$

1.4.3 Stellar models

The stellar components of dwarf galaxies are modelled under the assumption that they contribute negligibly to the total gravitational potential of the dwarf. This assumption is well motivated by the high mass-to-light ratios of most dwarf galaxies, as detailed in section 1.2. Assuming, in addition, that stellar and dark matter density distributions

are both spherical and isotropic, this allows us to implement the method of Bullock and Johnston (2005) to 'paint' a stellar population over an existing N-body model of a dark matter halo.

First, we define the phase-space distribution function, $f(E) = \mathrm{d}N/\mathrm{d}\Omega$, which determines the number, N, of particles of energy E per phase space volume element $\mathrm{d}\Omega = \mathrm{d}^3r\,\mathrm{d}^3v$. This function may be obtained from the density $\rho(r)$ and the spherical potential $\Phi(r)$ using Eddington inversion (Eddington, 1916). Given $f(E)$, the differential energy distribution follows: $\mathrm{d}N/\mathrm{d}E = f(E)g(E)$, where $g(E)$ is the density of states. Because we assume the dwarf galaxy's potential is sourced by the dark matter only, $g_\star(E) = g_{\mathrm{DM}}(E)$. Thus, the densities cancel out and the probability of a given N-body particle with energy E of representing a star becomes proportional to the ratio of the two distribution functions:

$$\mathscr{P}_\star(E) \propto \frac{(\mathrm{d}N/\mathrm{d}E)_\star}{(\mathrm{d}N/\mathrm{d}E)_{\mathrm{DM}}} = \frac{f_\star(E)}{f_{\mathrm{DM}}(E)}$$

Using this approach, stellar components are modelled with Einasto (1965) profiles:

$$\rho_{\mathrm{Einasto}}(r) = \rho_0 \exp\left[-(r/a_{\mathrm{E}})^\alpha\right],$$

where a_{E} is the scale radius and $\alpha = 1$ corresponds to an exponential sphere.

1.5 Thesis Outline

This thesis presents the tidal evolutions of a few notable and singularly distinct Milky Way satellites.

Chapter 2 details the evolution of one of the brightest companions of the Milky Way – the Fornax dwarf spheroidal galaxy. In particular, therein I detail how the tidal field of a Milky Way host affects the structure and kinematics of the dark matter and stellar components of Fornax. I review also the effect that the presence of a tidal field imparts on the radial decay of the five globular clusters which reside within the Fornax dark matter halo.

In chapter 3, I move to discuss one of the most peculiar dwarf galaxies observed in the Local Group – Crater II, interesting on account of its exceptionally large size despite a relatively low surface brightness and low velocity dispersion. Here I will show that, assuming a fairly massive initial halo as for Fornax, and independent of initial extent, the size of a stellar population closely follows the characteristic size of the dark matter

subhalo in which it is embedded. For the case of Crater II, this means that by the time the system is stripped sufficiently to reproduce the observed velocity dispersion, the stellar component has been reduced to sizes far smaller than those observed.

In chapter 4, I present a possible scenario by which large, and yet dynamically cold, galaxies such as these may arise despite this challenge, focusing on the specific case of the Antlia II dSph.

Chapter 5 contains a summary of my overall conclusions and an overview of future prospects.

Chapter 2

The tidal evolution of the Fornax dwarf spheroidal and its globular clusters

Text from this chapter was originally published in Monthly Notices of the Royal Astronomical Society: 2022, vol. 509, issue 4, pp 5330-5339. Published by Oxford University Press on behalf of the Royal Astronomical Society.

https://doi.org/10.1093/mnras/stab2912

Authors: Alexandra Borukhovetskaya[1], Raphaël Errani[2], Julio F Navarro[1], Azadeh Fattahi[3], and Isabel Santos-Santos[3]

2.1 Abstract

The dark matter content of the Fornax dwarf spheroidal galaxy inferred from its kinematics is substantially lower than expected from LCDM cosmological simulations. We use N-body simulations to examine whether this may be the result of Galactic tides. We find that, despite improved proper motions from the Gaia mission, the pericentric distance of Fornax remains poorly constrained, mainly because its largest velocity component is roughly anti-parallel to the solar motion. Translating Fornax's proper motion into a Galactocentric velocity is thus sensitively dependent on Fornax's assumed distance: the observed distance uncertainty, ±8%, implies pericentric distances that vary between $r_{\rm peri} \sim 50$ and $r_{\rm peri} \sim 150\,$kpc. Our simulations show that for $r_{\rm peri}$ in the lower range

[1]Department of Physics and Astronomy, University of Victoria, Victoria, BC V8P 5C2, Canada
[2]Université de Strasbourg, CNRS, Observatoire astronomique de Strasbourg, UMR 7550, F-67000 Strasbourg, France
[3]Institute for Computational Cosmology, Department of Physics, University of Durham, South Road, Durham DH1 3LE, UK

of that estimate, a LCDM subhalo with maximum circular velocity $V_{max} = 40\,km\,s^{-1}$ (or virial mass $M_{200} \approx 10^{10} M_{\odot}$, as expected from LCDM) would be tidally stripped to $V_{max} \sim 23\,km\,s^{-1}$ over 10 Gyr. This would reduce the dark mass within the Fornax stellar half-mass radius to about half its initial value, bringing it into agreement with observations. Tidal stripping affects mainly Fornax's dark matter halo; its stellar component is affected little, losing less than 5% of its initial mass in the process. We also explore the effect of Galactic tides on the dynamical friction decay times of Fornax's population of globular clusters (GC) and find little evidence for substantial changes, compared with models run in isolation. A population of GCs with initial orbital radii between 1 and 2 kpc is consistent with the present-day spatial distribution of Fornax GCs, despite assuming a cuspy halo. Neither the dark matter content nor the spatial distribution of GCs of Fornax seem inconsistent with a simple model where Fornax inhabits a tidally-stripped cuspy cold dark matter halo.

2.2 Introduction

The standard model of cosmology, Lambda Cold Dark Matter (LCDM), predicts structures to form hierarchically. In this paradigm, large self-bound structures (haloes) form through the accretion and mergers of smaller ones (subhaloes), which in turn form from small scale density perturbations in the early Universe (White and Rees, 1978). Massive haloes allow stars to form in their centres from cooling of accreted gas: the more massive the host halo, the more stars it is able to form. In low-mass haloes ($\lesssim 10^9 M_{\odot}$), however, cosmic reionization and energetic feedback from stellar evolution reduce substantially a halo's ability to form stars (Bullock et al., 2000; Benson et al., 2002; Somerville, 2002).

This implies that a steep non-linear relation between the dark matter masses of the smallest haloes and their stellar masses is expected in LCDM, a prediction that has been supported by both semianalytic techniques such as "abundance-matching" (Guo et al., 2010; Moster et al., 2013; Behroozi et al., 2013), and by direct cosmological hydrodynamical simulations (e.g., the Illustris and EAGLE simulations, Vogelsberger et al., 2014; Schaye et al., 2015, respectively).

More specifically, on the scale of dwarf galaxies, simulations predict that galaxies with stellar masses $M_{str} \sim 2.4 \times 10^7\, M_{\odot}$, like the Fornax dwarf spheroidal (dSph) (see Table 2.2), should form in a halo with a virial[4] mass of at least $M_{200} \approx 10^{10}\, M_{\odot}$ (Wang et al., 2015;

[4]We define the virial mass as the mass enclosed within the radius of overdensity 200 times the critical density required for closure, $\rho_{crit} = 3H^2/8\pi G$, where $H(z)$ is Hubble's constant and $H_0 = H(0) =$

Fattahi et al., 2018; Garrison-Kimmel et al., 2019; Munshi et al., 2021).

In LCDM, where the dark matter halo mass distribution is adequately approximated by Navarro-Frenk-White profiles (Navarro et al., 1996a, 1997, hereafter NFW), this virial mass corresponds to a halo with maximum circular velocity, $V_{\rm max} = 39.6\,{\rm km\,s^{-1}}$, for a "concentration" parameter $c = 12.5$ (Ludlow et al., 2016). The mass profile of such a halo is fully specified, enabling predictions of the dark mass enclosed within the galaxy stellar half-mass radius[5], where observational constraints are tightest (Walker et al., 2009; Wolf et al., 2010). In the case of the Fornax dSph, $r_{1/2} \approx 1\,{\rm kpc}$, and observations suggest a total enclosed mass of $M_{\rm tot}(< r_{1/2}) \approx 9 \times 10^7\,M_\odot$ (or, equivalently, a circular velocity of $V_c(r_{1/2}) \approx 20\,{\rm km\,s^{-1}}$), much larger than the mass in the stellar component (Fattahi et al., 2016b; Read et al., 2019).

For an NFW halo of average concentration, the latter constraint implies $V_{\rm max} \sim 25\,{\rm km\,s^{-1}}$, substantially below that expected from the cosmological simulations referenced above. The disagreement is amplified by the steep non-linear dependence of stellar mass on halo mass in this regime. Indeed, in LCDM haloes with $V_{\rm max} \sim 25\,{\rm km\,s^{-1}}$ are expected to harbour dwarfs with $M_{\rm str} \sim 10^6\,M_\odot$, more than an order of magnitude less luminous than Fornax. If such low-mass haloes were to harbour galaxies as massive as Fornax, one would expect nearly an order of magnitude more Fornax-like dwarfs than observed in the Local Group.

The unexpectedly low dark matter content of Fornax is often cited as suggesting the presence of a constant-density "core" in the inner halo density profile (see, e.g., Walker and Peñarrubia, 2011; Amorisco et al., 2013). Such cores may result from the supernova-driven cycling of baryons in and out of the inner regions of a halo during galaxy formation (see; e.g., Navarro et al., 1996a; Read and Gilmore, 2005b; Pontzen and Governato, 2012; Di Cintio et al., 2014), but their occurrence is not universally accepted.

In the absence of cores, one would need to argue that the dark matter content of Fornax has been eroded somewhat by Galactic tides. Fornax's stellar component shows no obvious sign of tidal disturbance, however, but tidal stripping is expected to affect mainly the more extended dark matter component (see; e.g., Peñarrubia et al., 2008). Tidal stripping may thus lead to a reduction of the dark matter content of a dwarf without affecting much the stellar component. This has been argued by Genina et al. (2020), for example,

67.74 km Mpc^{-1} s^{-1} (Planck Collaboration et al., 2016)

[5]We shall use uppercase $R_{1/2}$ to denote projected half-mass radii and lowercase $r_{1/2}$ to denote deprojected, 3D, radii. We shall usually assume $R_{1/2} = (3/4)\,r_{1/2}$, as appropriate for spherical systems, unless otherwise noted.

who selected dwarf galaxies with orbital properties similar to Fornax in the APOSTLE simulations, and showed that many such satellites lose more than half of their mass from within their innermost ~ 1 kpc.

Although plausible, the main obstacle to this tidal-stripping interpretation is Fornax's large Galactocentric distance (~ 149 kpc Pietrzyński et al., 2009), together with early estimates of its orbital eccentricity, which suggested a low-eccentricity orbit (see; e.g., Piatek et al., 2002; Dinescu et al., 2004; Battaglia et al., 2015, and references therein). At such distance, it would be unlikely for Fornax to have been affected much by Galactic tides if it was on a nearly circular orbit.

Besides its unexpectedly low dark matter content, Fornax has long been argued to pose an additional problem for LCDM. This relates to its globular cluster (GC) spatial distribution, which seems inconsistent with the fact that their dynamical friction orbital decay timescales appear to be much shorter than their ages (Tremaine, 1976; Hernandez and Gilmore, 1998). Goerdt et al. (2006) proposed that the problem could be resolved if the structure of the Fornax dark halo had a sizeable constant density core, a result echoed in subsequent work (see; e.g., Read et al., 2006; Cole et al., 2012; Petts et al., 2015).

More recent work, however, has argued for a different explanation that does not require a core. Meadows et al. (2020), for example, report that GCs have similar dynamical friction timescales in both cuspy *and* cored halos normalized to match observed constraints on $M_{\rm tot}(< r_{1/2})$. More precisely, in either case GCs are driven by dynamical friction to well-defined terminal radii in about the same time. The difference is where they end up: GCs are driven close to the centre in the case of a cusp but "stall" at about one-third of the core radius[6] (~ 300 pc for a ~ 1 kpc core). Because there is no clearcut evidence for such characteristic common radius for GCs in Fornax, this suggests that, if dynamical friction has indeed affected GC orbits, its effects have been mild and might still be ongoing.

In this interpretation, Fornax GCs were likely formed or accreted into Fornax on orbits with radii somewhat larger than where they are today (Angus and Diaferio, 2009; Boldrini et al., 2019). Indeed, dynamical friction timescales depend sensitively on orbital radius, and it is relatively easy to accommodate the present-day configuration of GCs if their initial radii were just outside Fornax's half-light radius, $r_{1/2}$ (Meadows et al., 2020). Would such clusters survive stripping by Galactic tides if the latter are indeed responsible

[6]The core radius is defined here as the distance where the projected density of the halo drops to 1/2 of its central value. Since this convention is not always followed, care is needed when comparing quantitative results for the "stall radius" from different authors.

for the low dark matter content of Fornax?

A further alternative is that GC orbital decay may have been affected by the "dynamical stirring" and halo mass loss that could arise from Galactic tides (Oh et al., 2000). If so, the effect of Galactic tides could, in principle, serve to solve the two problems at once, reconciling the low dark matter content of Fornax, as well as the unexpectedly long decay timescales of its GCs, with the predictions of LCDM.

We explore these questions here using a series of controlled, high-resolution *N*-body simulations of the tidal evolution of Fornax. This paper is structured as follows: in section 2.3 we discuss our numerical setup, with section 2.3.1 detailing our Milky Way host model, section 2.3.2 describes our choice of orbital parameters, and sections 2.3.3 - 2.3.4 detail our halo model and *N*-body realisations. Section 2.4 presents our results, beginning with the dynamical evolution of dark matter in section 2.4.1 and ending with the effect of tides on the stellar component (section 2.4.2) and globular clusters (section 2.4.3). We conclude with a summary of our conclusions in Sec. 2.5.

2.3 Numerical Setup

This section outlines the numerical setup of the *N*-body simulations used to follow the tidal evolution of our Fornax model in the gravitational potential of the Milky Way.

2.3.1 Galaxy model

The Milky Way is modelled as an analytical, static potential, consisting of an axisymmetric two-component Miyamoto and Nagai (1975) disk, a Hernquist (1990) bulge and an NFW dark matter halo. These models and their parameters are as summarised in section 1.4.2.

2.3.2 Orbits

The orbit of Fornax in the Milky Way potential is specified by its present-day Galactocentric position and velocity, as inferred from its sky position, radial velocity, distance, and proper motion. Of these, the sky position and radial velocity $v_r = 55.3 \pm 0.3\,\mathrm{km\,s^{-1}}$ have negligible uncertainties (see; e.g., Fritz et al., 2018) . The heliocentric distance and proper motions, on the other hand, are known to $\sim 10\%$ accuracy: $d = 147 \pm 12.0\,\mathrm{kpc}$ (Pietrzyński et al., 2009), and $\mu_{\alpha^*} = 0.374 \pm 0.035$ mas/yr, $\mu_\delta = -0.401 \pm 0.035$ mas/yr

Table 2.1: Current observational constraints, as well as parameters of the three orbits explored using N-body simulations in this study. Orbit 2 is the orbit corresponding to the median observed quantities. The current positions and velocities of Fornax corresponding to orbits 1, 2 and 3, expressed as 6D Cartesian coordinates, lie each within at most one standard deviation of the ones derived by Gaia Collaboration et al. (2018). Pericentres and apocentres are computed for the Milky Way potential model discussed in section 2.3.1, while heliocentric and galactocentric coordinates are computed with solar parameters of Schönrich et al. (2010).

observation	α	δ	distance (kpc)	μ_{α^*} (mas yr^{-1})	μ_δ (mas yr^{-1})	v_r (km s^{-1})
	$2^h39^m59.3^s$ (1)	$-34°26'57''$ (1)	147 ± 12.0 (2)	0.374 ± 0.035 (3)	-0.401 ± 0.035 (3)	55.3 ± 0.3 (3)
	X (kpc)	Y (kpc)	Z (kpc)	V_X (km s^{-1})	V_Y (km s^{-1})	V_Z (km s^{-1})
heliocentric	−32.9	−50.9	−134	29.3	−377	75.5
galactocentric	−41.2	−50.9	−134	40.4	−125	82.8

(1) McConnachie (2012) , (2) Pietrzyński et al. (2009), (3) Fritz et al. (2018)

model parameters	pericentre (kpc)	apocentre (kpc)	distance (kpc)	μ_{α^*} (mas yr^{-1})	μ_δ (mas yr^{-1})	v_r (km s^{-1})
orbit 1	53.1	137	137	0.384	-0.382	55.1
orbit 2	90.5	155	147	0.374	−0.401	55.3
orbit 3	128	189	158	0.390	-0.376	55.4

(Fritz et al., 2018)[7].

These uncertainties result in a fairly broad distribution of possible pericentric and apocentric distances. This is shown in Fig. 2.1, where we plot in the top two panels, as a function of the assumed distance, the resulting pericentric and apocentric distances in the potential described in Sec. 2.3.1. The pericentric distance, the parameter most critical in respect to the effect of Galactic tides, ranges from ~ 50 kpc at the 16th percentile to ~ 130 kpc at the 84th percentile of the distribution obtained by varying all parameters within their uncertainty range. In other words, a $\sim 10\%$ uncertainty in distance translates into more that a factor of two uncertainty in pericentric distance.

This striking sensitivity of the pericentric distance on assumed distance is due to Fornax's direction of motion, which lies approximately anti-parallel to the solar motion around the Galaxy. As a result, Fornax's velocity in the heliocentric frame is mainly tangential and quite large, ~ 350 km s^{-1}, far exceeding Fornax's total speed in the Galactocentric reference frame (see Table 2.1).

Since proper motions are measured in the heliocentric frame, an $\sim 8\%$ uncertainty in distance implies a large tangential velocity uncertainty, roughly 21% in terms of the Galactocentric tangential velocity. This is shown in the bottom panel of Fig. 2.1, where

[7]Where with μ_{α^*} we designate the proper motion in α including the $\cos(\delta)$ factor.

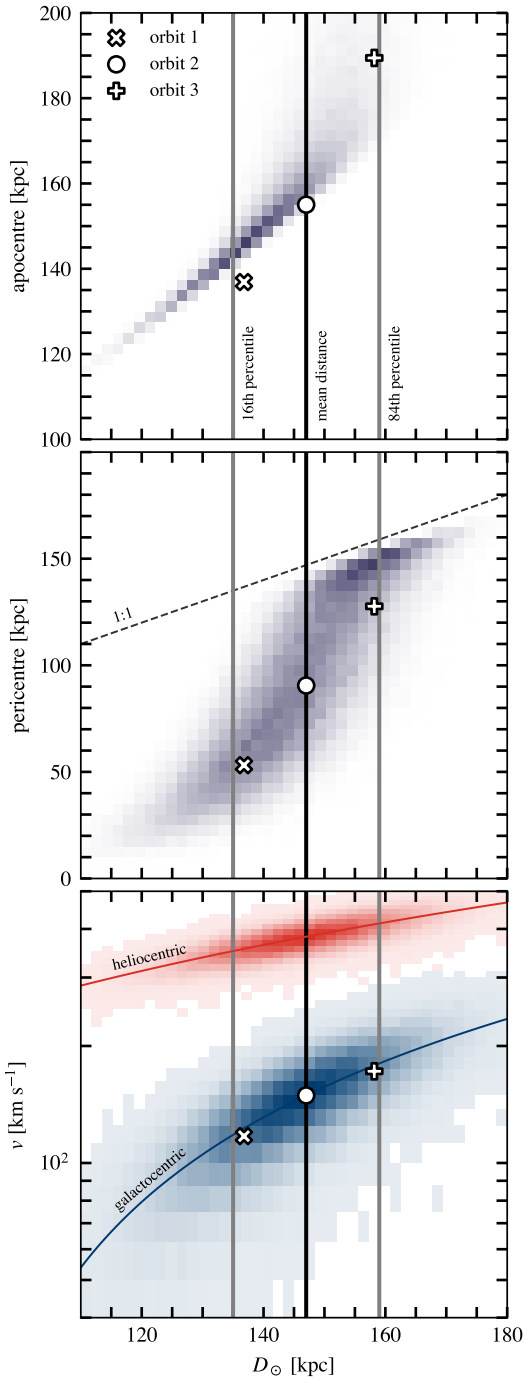

Figure 2.1: The apocentric (top panel) and pericentric (central panel) distance of Fornax as a function of heliocentric distance, varying the proper motions and radial velocity within the observed uncertainties. The properties corresponding to the three orbits of Table 2.1 are highlighted in each panel using white symbols (x, ∘, +). Vertical lines correspond to the median measured distance (black) as well as the 16th and 84th percentile (grey). The bottom panel shows the heliocentric (red) and galactocentric (blue) tangential velocities. Note that the distance uncertainty propagates to a large uncertainty in the Galactocentric velocity.

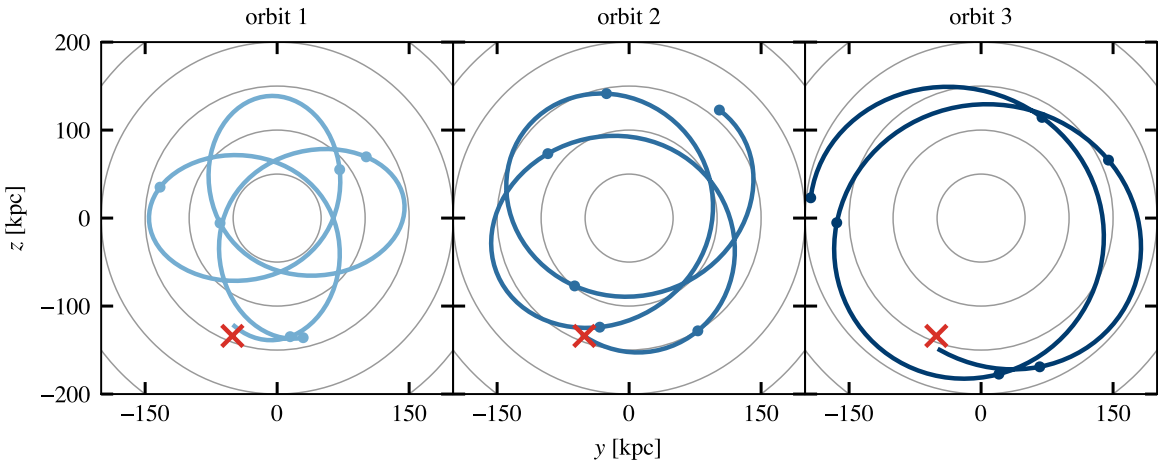

Figure 2.2: Projected trace on the Y, Z plane of the three orbits considered in this study (see Table 2.1). The current position of Fornax is indicated by a red cross. Intervals of 2 Gyr along the orbit are shown using filled circles.

we show the effect of distance on the inferred heliocentric and Galactocentric tangential velocities of Fornax. Because the Galactocentric tangential velocity is not tightly constrained, the orbital pericentre is likewise poorly determined.

Because of this uncertainty, we have explored three different orbits, with orbital properties as given by the open symbols in Fig. 2.1. These orbits have notably different pericentric distances, $r_{\rm peri} = 53.1$, 90.5, and 128 kpc, and the corresponding orbits are hereafter referred to as orbits 1, 2 and 3, respectively, with main parameters listed in Table 2.1. Initial conditions for the N-body runs are obtained by integrating those orbits backwards in time for 10 Gyr. The shape of the resulting orbits are shown in Fig. 2.2. Note that the three orbits are nearly polar, and close to the Y-Z plane[8].

2.3.3 Fornax model

We model the Fornax dSph halo as an equilibrium N-body realisation of an NFW density profile,

$$\rho_{\rm NFW}(r) = \frac{M_{200}}{4\pi r_s^3} \frac{(r/r_s)^{-1}(1+r/r_s)^{-2}}{[\ln(1+c) - c/(1+c)]}. \tag{2.1}$$

This profile is fully specified by two parameters; e.g., a virial mass, M_{200}, and concentration, c, or, alternatively, by a maximum circular velocity, $V_{\rm max}$, and the radius at which it is achieved, $r_{\rm max}$. The latter is often favoured since, unlike the former, it is defined

[8] We use a co-ordinate system where the Sun is located at $(X, Y, Z)_\odot = (-8.3{\rm kpc}, 0, 0)$, and the velocity of the local standard of rest is in the positive Y direction.

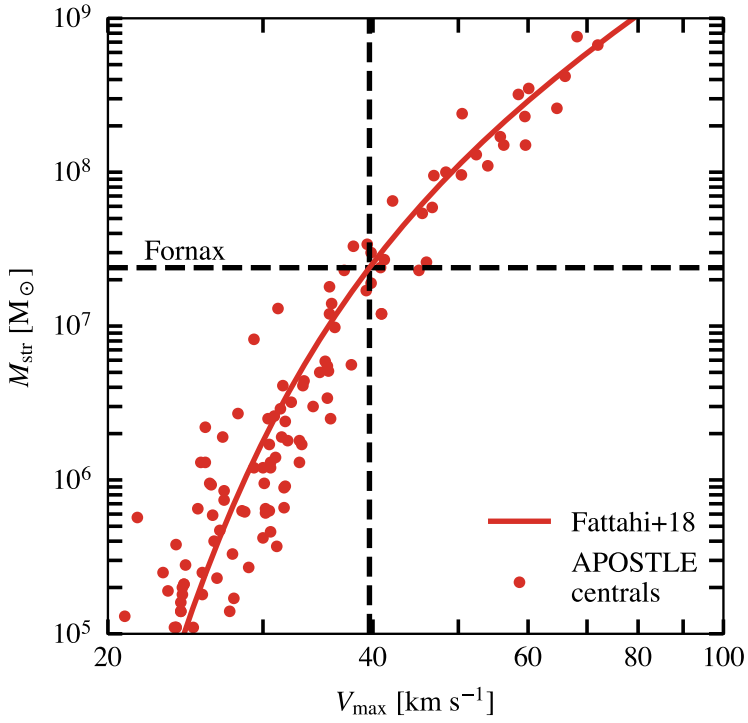

Figure 2.3: Stellar mass, M_{str}, versus maximum circular velocity, V_{max}, of central galaxies from the highest resolution level (L1) runs in the APOSTLE simulations as described in Fattahi et al. (2018). The red solid line is the average relation from that work (Eq. 2.2). Dashed lines indicate stellar mass and derived V_{max} for Fornax as listed in Table 2.2.

independently of redshift and may be more directly compared with observations.

Cosmological hydrodynamical simulations have shown that V_{max} correlates strongly with galaxy stellar mass, M_{str}, as shown, for example, in Fig. 2.3 for results from the APOSTLE suite of Local Group simulations (Sawala et al., 2016; Fattahi et al., 2016a).

We use the empirical fit from Fattahi et al. (2018),

$$M_{str}/\mathrm{M}_\odot = m_0 v^\alpha \exp(-v^\gamma) \tag{2.2}$$

where $v = V_{max}/50\,\mathrm{km\,s^{-1}}$, and $(m_0, \alpha, \gamma) = (3.0 \times 10^8, 3.36, -2.4)$. This fit is shown in Fig. 2.3, along with measured stellar masses and maximum circular velocities of isolated galaxies in the APOSTLE simulation.

We adopt a stellar mass for Fornax of $M_{str} = 2.39 \times 10^7\,\mathrm{M}_\odot$, computed from the apparent V-band luminosity as in Irwin and Hatzidimitriou (1995), the distance modulus of Pietrzyński et al. (2009) and the stellar mass-to-light ratio of Woo et al. (2008). Equation 2.2 then suggests a maximum circular velocity of $V_{max} = 39.6\,\mathrm{km\,s^{-1}}$. This assumes that

Table 2.2: Current properties of Fornax ($M_{str}, V_{1/2}, r_{1/2}$) and inferred structural parameters at infall (V_{max}, r_{max}). The stellar mass is derived from the distance modulus of Pietrzyński et al. (2009), the V-band magnitude of Irwin and Hatzidimitriou (1995), and the stellar mass-to-light ratio of Woo et al. (2008). The maximum circular velocity at infall V_{max} is estimated from the stellar mass through Eq. 2.2, and the corresponding r_{max} is chosen to match the Ludlow $z = 0$ mass-concentration relation (Ludlow et al., 2016). Half-light radius $r_{1/2}$ and circular velocity $V_{1/2}$ at the half-light radius are as in Fattahi et al. (2018).

M_{str} ($10^7\,M_\odot$)	$V_{max,infall}$ (km s^{-1})	$r_{max,infall}$ (kpc)	$V_{1/2}$ (km s^{-1})	$r_{1/2}$ (kpc)
2.39	39.6	7.99	20.2 ± 2.8	$0.949^{+1.06}_{-1.00}$

tides have not affected Fornax's stellar mass – an assumption which we shall see justified by our results, as discussed in Sec. 2.4.2.

The radius where the circular velocity peaks, r_{max}, may be calculated from the Ludlow et al. (2016) parametrisation of the LCDM halo mass-concentration relation at redshift $z = 0$. As listed in Table 2.2, the resulting NFW profile has $V_{max} = 39.6\,\mathrm{km\ s^{-1}}$ and $r_{max} = 8.0\,\mathrm{kpc}$, or, in terms of virial mass and concentration, $M_{200} = 1.04 \times 10^{10}\,M_\odot$ and $c = 12.5$. This initial virial mass is roughly a factor of two lower than the average halo mass inferred for galaxies which host as many GCs as Fornax, but well within the scatter of that relation (see; e.g., Forbes et al., 2018; Shao et al., 2020).

The N-body realisation of the halo model is constructed with 10^6 particles (10^7 in some cases, as specified in section 2.4.3) using the `Zeno`[9] software package developed by Joshua Barnes at the University of Hawaii. This software provides routines for Monte Carlo sampling a given distribution function whereby a system in virial equilibrium may be generated. In order for the system to fully relax prior to introducing an external potential, the halo is run in isolation for 6 Gyr using the publicly available `GADGET-2` simulation code (Springel, 2005), as detailed below.

2.3.4 Simulation code

We use the N-body code `GADGET-2` (Springel, 2005) to evolve of our N-body models. This code implements a hierarchical tree algorithm to compute gravitational interactions. Forces between particles are smoothed with a Plummer-equivalent softening length of $\epsilon_p = 40\,\mathrm{pc}$ for $N = 10^6$ and $\epsilon_p = 13\,\mathrm{pc}$ for $N = 10^7$ particles. For each of the orbits

[9] http://www.ifa.hawaii.edu/faculty/barnes/zeno/

described in section 2.3.2, the N-body model is evolved on the respective orbit in the potential of Section 2.3.1 for ~ 10 Gyr. We have also evolved the same N-body models in isolation to identify the smallest radius for which our mass profiles are numerically converged. Defining this as the innermost radius where circular velocities deviate by less than $\sim 1\%$ from the target NFW profile, we consider our results converged outside $r_{\rm conv} = 450$ pc and $r_{\rm conv} = 140$ pc for our 10^6 or 10^7-particle runs, respectively.

2.4 Results

We present below the results of the evolution of our Fornax N-body model in the Galactic potential for each of the three orbits discussed above. We discuss first the stripping of dark matter, followed by a discussion of the stripping of a hypothetical embedded stellar component that matches Fornax's light distribution. We end with a discussion of how Galactic tides may affect the orbital decay of Fornax GCs.

2.4.1 Dark matter stripping

Dashed lines in Fig. 2.4 show the evolution of the maximum circular velocity of our Fornax haloes for the three simulated orbits. Consistent with the findings of Hayashi et al. (2003) and Peñarrubia et al. (2008), as tides strip the system, $V_{\rm max}$ decreases continuously, with abrupt changes corresponding to pericentric passages.

As expected, the smaller the pericentre the stronger the tidal forces and thus the more significant the mass loss. For orbit 1 ($r_{\rm peri} = 53$ kpc), the circular velocity at the half-light radius, $V_{1/2} \equiv V_{\rm c}(r_{1/2} = 1\,{\rm kpc})$, drops enough after just 4 Gyr to fall within the 1-σ interval around the observational estimate, $20.2 \pm 2.8\,{\rm km\,s^{-1}}$, shown as a grey band in Fig. 2.4 (Fattahi et al., 2016b). For orbit 1, even after ~ 10 Gyr, $V_{1/2}$ is still consistent with the observed value. The remnant halo in this case retains only 6% of its initial dark mass (yet still fairly well resolved, with more than 2×10^4 particles within $r_{\rm max}$), and its $V_{\rm max}$ has dropped from $\sim 40\,{\rm km\,s^{-1}}$ to roughly $23\,{\rm km\,s^{-1}}$. (The snapshots that match best the current Galactocentric distance of Fornax after ~ 10 Gyr of evolution are indicated by symbols in Fig. 2.4.)

On the other hand, models on orbits 2 and 3 ($r_{\rm peri} = 91$ and 134 kpc) do not lose enough mass for $V_{1/2}$ to reach the 1-σ error band of the observationally inferred value, even after ~ 10 Gyr of evolution.

The final circular velocity profiles are shown for the three orbits in Fig. 2.5. As shown

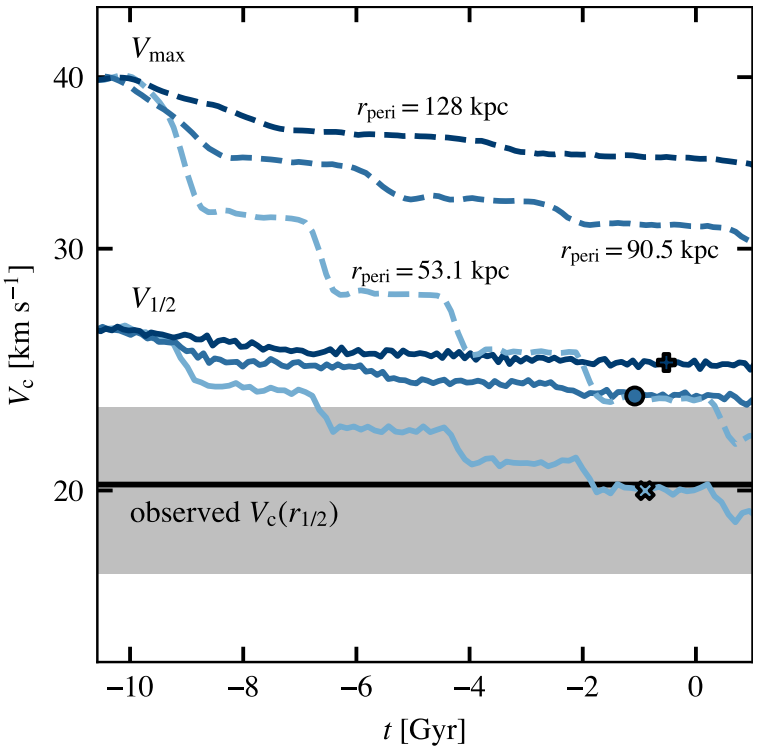

Figure 2.4: Evolution of the circular velocity of the Fornax halo for the three different orbits, shown in different shades of blue. Lighter shades correspond to smaller pericentres, as labelled. Solid lines show the circular velocity at the half-light radius, $r_{1/2}$, and dashed lines at the radius of maximum circular velocity, r_{max}. Symbols indicate the snapshot closest to $t = 0$ which matches the current galactocentric distance of Fornax. The black solid line and grey shaded region correspond to the observational constraint on $V_{1/2}$ as well as the $\pm 1\sigma$ uncertainty interval as in Fattahi et al. (2018).

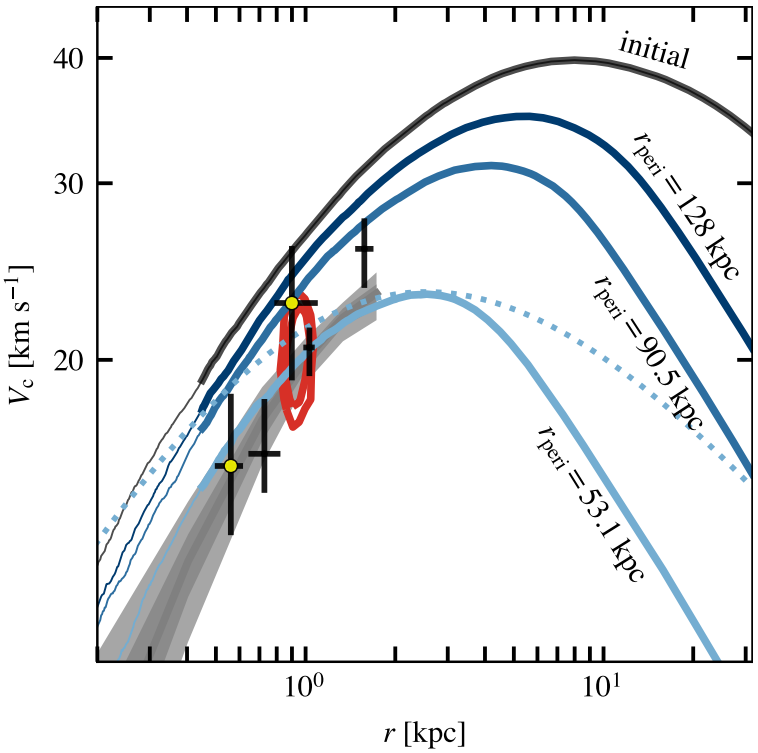

Figure 2.5: Initial and final circular velocity profiles of the Fornax halo for the three simulated orbits. The red contours are constraints on the enclosed mass within ~ 1 kpc, derived from the stellar velocity dispersion and density profiles (see Fattahi et al. (2016b), for details). The grey band corresponds to the kinematic analysis of Read et al. (2019). Error bars with yellow centres show the estimates of Walker and Peñarrubia (2011), while the remaining three errorbars show the estimates of Amorisco et al. (2013). The dotted line shows an NFW profile with $V_{\rm max}$ and $r_{\rm max}$ as in the final circular velocity profile of orbit 1. The transition from thick to thin lines indicate $r_{\rm conv}$, the convergence radius defined in Sec. 2.3.4.

in this figure, the final V_c profile of the tidally-stripped halo on orbit 1 matches well not only the Fattahi et al. (2016b) constraints on the mass enclosed within ~ 1 kpc (red contours), but also – within 2 sigma – the mass profile of Read et al. (2019) derived from a kinematic analysis of Fornax's stellar component (shaded band). Tighter observational constraints at small radii should help to further assess the viability of the tidally-driven scenario proposed here.

Note, in particular, that the mass profile of the stripped halo differs from the NFW shape: the dotted curve in Fig. 2.5 shows an NFW profile with the same $r_{\rm max}$ and $V_{\rm max}$ as the final Fornax model profile on orbit 1 (see; e.g., Errani and Navarro, 2021, for details). The orbit 1 final profile is also in reasonable agreement with mass estimates from Walker and Peñarrubia (2011) and Amorisco et al. (2013), shown by the symbols with error bars in Fig. 2.5.

We conclude that tidal effects may very well reconcile the observed low dark matter content of Fornax with the relatively massive halo suggested by current LCDM cosmological hydrodynamical simulations. This requires that Fornax is on an eccentric orbit with $r_{\rm peri}$ as small as ~ 50 kpc, and that it has orbited the Milky Way potential for at least 4-5 Gyr. This is consistent with the observed proper motions if Fornax's current distance is of order 140 kpc or less, a value well within the error bar on the current estimate of 147 ± 12 kpc. Tighter constraints on Fornax's distance would help to verify this prediction.

2.4.2 Stellar component stripping

As discussed in the previous section, Galactic tides are capable of substantially altering the internal distribution of dark matter in the Fornax dSph. We study next to what extent the same tides may affect Fornax's stellar population, limiting this analysis to orbit 1, which is subject to the strongest tides.

To begin, we shall assume that stars are collisionless tracers of the underlying dark matter potential. This is well motivated by the large dark-to-stellar mass ratio of Fornax, as discussed in Sec. 2.2. We use the approach introduced by Bullock and Johnston (2005) to assign stellar probabilities to each dark matter particle, using the publicly available[10] implementation of Errani and Peñarrubia (2020).

[10] https://github.com/rerrani/nbopy

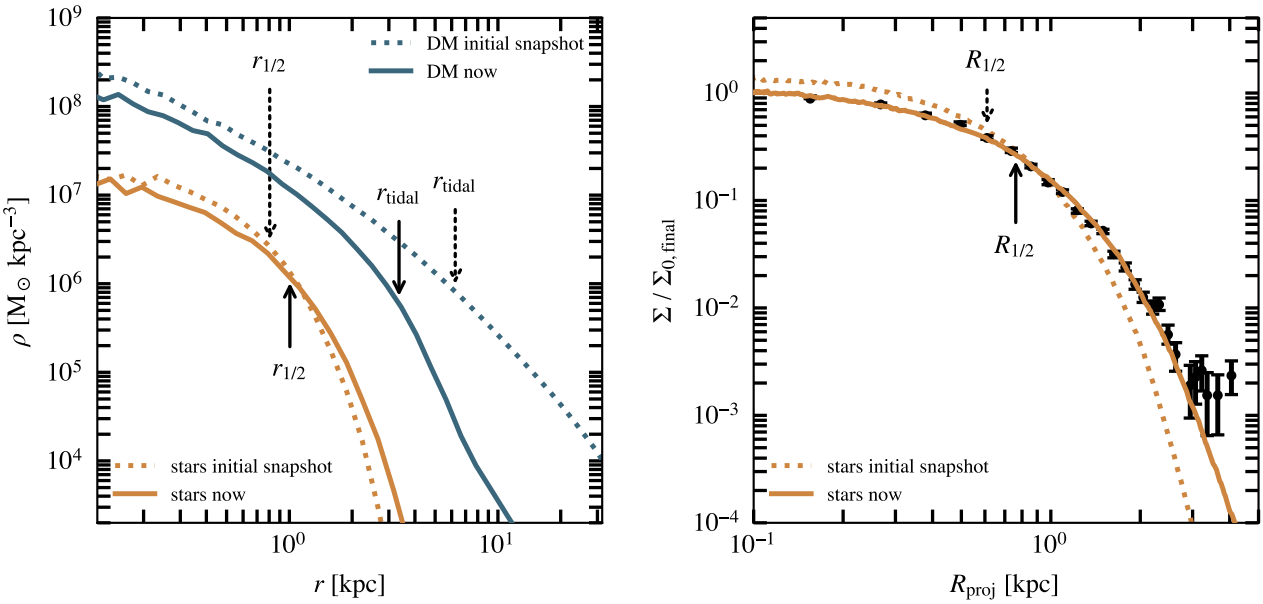

Figure 2.6: Left: Dark matter (blue) and stellar (orange) density profiles at infall (dotted curves) and after ~ 10 Gyr on orbit 1 (solid curves). 3D half-mass and tidal radii are shown using arrows. Right: Surface brightness (orange curves, normalized to the final central value) profiles obtained from the N-body simulations, compared against the observational data by Coleman et al. (2005) (black data points). The projected (2D) half-light radii are shown using arrows. The stellar profile, being deeply embedded in the Fornax dark matter halo, is less affected by tides than the dark matter.

The initial stellar density profile is modelled as an Einasto profile (Einasto, 1965),

$$\rho_{\rm E}(r) = \rho_{\rm E0} \exp\left[-(r/a)^{1/n}\right], \tag{2.3}$$

with index $n = 0.81$ and scale radius $a = 0.44$ kpc. (The central density $\rho_{\rm E0}$ depends on the stellar mass-to-light ratio assumed, but it should be inconsequential provided the system is dark matter dominated throughout.)

These parameters have been chosen so that after ~ 10 Gyr of evolution, the simulated stellar distribution of the remnant matches the currently observed stellar density profile. The initial and final stellar density profiles are shown in Fig. 2.6. The left panel shows the simulated profiles in 3D, whereas the right panel shows them in projection. These Sersic (1968) profiles fit very well the observed surface density of Fornax (circles with error bars, normalized to the central value) taken from Coleman et al. (2005).

While tides have a significant effect on the dark matter content of Fornax, the effect of tides on the stellar density distribution is minor. More than 95% of the initial stellar mass remains bound, and its half-mass radius increases only by $\sim 25\%$ over 10 Gyr of evolution. Battaglia et al. (2015) reached a similar conclusion, wherein more than 99% of stellar particles remain bound, although they assumed a lower initial Fornax halo mass, and orbits with larger pericentric distances. The marginal stellar mass loss corroborates our earlier assumption in section 2.3.3: the current stellar mass of Fornax is essentially unchanged by the Galactic tides, and may thus be used to estimate the halo mass at infall.

Fig. 2.7 shows the distribution of stars in the Fornax model as projected on the sky [11]. The left panel shows an area of $5^\circ \times 5^\circ$ centred on Fornax, and shows no obvious signature of tidal effects, consistent with the recent analysis of Wang et al. (2019), who report no tidal signature in the innermost 2°. Only far from the main body of the galaxy do signs of tidal distortions become evident. This becomes apparent when plotting a larger area around the dwarf (right-hand panel of Fig. 2.7), which shows the presence of a very faint stellar tidal stream, with a surface brightness more than $1000\times$ fainter than the central surface brightness of Fornax. The total stellar mass outside a sphere of radius 2 kpc is only $2.6 \times 10^6\,{\rm M}_\odot$, or approximately a tenth of Fornax's initial stellar mass.

We conclude that, despite the large losses of dark matter due to stripping, the stellar component remains relatively undisturbed, and should show no obvious signatures of tidal disturbance. Signs of past tidal interaction may be present in the form of very low

[11] An implementation of the tessellation method used to generate the surface brightness map is publicly available at `https://github.com/asya-b/voronoi`.

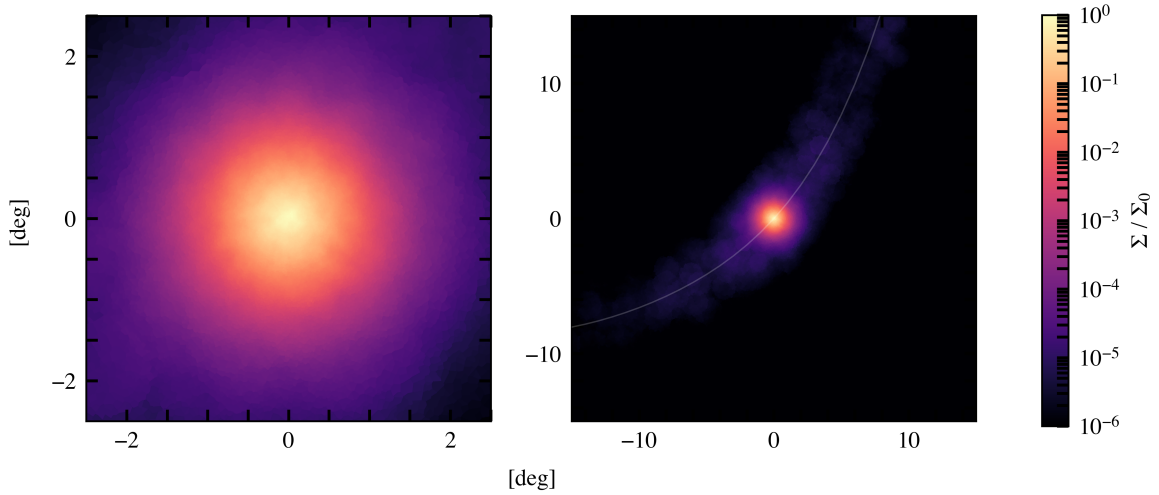

Figure 2.7: Surface brightness of the evolved Fornax model on orbit 1. At a heliocentric distance of 137 kpc, one degree in this figure corresponds to 2.4 kpc. The left panel shows an area of 25 deg^2 centred on Fornax. Deviations from spherical symmetry in the surface brightness become only evident in regions where the surface brightness drops below 1/1000 of its central value. The panel on the right shows a larger 900 deg^2 areas and suggest the presence of a faint stellar stream. The line passing along the tidal stream in the right-hand panel indicates the orbital path of Fornax.

surface brightness tidal tails around the Fornax dwarf aligned roughly in the direction of the orbital motion, as shown by the curve in the right-hand panel of Fig. 2.7. The discovery of such stars would provide strong support for the idea that tidal effects have played an important role in the dynamical evolution of Fornax.

2.4.3 Globular cluster orbital decay

We now focus our attention on the potential effects of tides on the orbital decay of the five globular clusters associated with the Fornax dSph. Meadows et al. (2020) have recently used N-body simulations to model the orbital decay of globular clusters in Fornax, modelled as a cuspy NFW halo. These authors argue that the globular clusters commonly referred to as GC3 and GC4 (see Table 2.3) are expected to sink to the centre of Fornax within the next ~ 2 Gyr due to dynamical friction, while the remaining three clusters (GC1, GC2, and GC5) are too far from the centre of Fornax or have too little mass to decay, even in a time span as long as 15 Gyr. In agreement with earlier work (Angus and Diaferio, 2009; Cole et al., 2012), these authors also conclude that even if GC3 and GC4 have experienced dynamical friction in a cuspy NFW halo for ~ 10 Gyr, they could have avoided sinking to the centre if their initial orbital radii was 1-2 kpc.

The models of Meadows et al. (2020), however, neglect the effect of Galactic tides and assume a relatively low halo mass for Fornax, namely an NFW halo with $V_{\rm max} = 25\,{\rm km\,s^{-1}}$, rather than the $40\,{\rm km\,s^{-1}}$ suggested by LCDM simulations. It is therefore important to explore whether their conclusions are robust to changes in the assumed halo mass, as well as to the inclusion of Galactic tides.

To this end we add globular clusters to our Fornax models with 10^7 particles, including them as single softened point masses, with masses chosen to match the present-day mass of Fornax GCs, between 3.7×10^4 and $36 \times 10^4\,{\rm M}_\odot$ (Mackey and Gilmore, 2003). The Plummer-equivalent softening length chosen for all GC particles is $\epsilon_{\rm P} = 13$ pc. Following Meadows et al. (2020), these clusters are placed on circular orbits at radii between 1 and 2 kpc and evolved first in isolation for 10 Gyr.

The orbital decay of these objects in isolation is shown by the grey lines in Fig. 2.8. GC1, GC2, and GC5 evolve very little over 10 Gyr, so choosing initial orbital radii consistent with their present-day projected radii (indicated by the horizontal dashed lines) results in good agreement with their observed position after 10 Gyr. No appreciable orbital decay is expected for any of these three GCs, at least when Fornax is evolved in isolation.

Table 2.3: Selected properties of Fornax globular clusters. Both projected radii and masses are taken from (Mackey and Gilmore, 2003).

Name	R [kpc]	$\log M$ [$M_\odot$]
GC 1	1.60	4.57 ± 0.13
GC 2	1.05	5.26 ± 0.12
GC 3	0.43	5.56 ± 0.12
GC 4	0.24	5.12 ± 0.24
GC 5	1.43	5.25 ± 0.20

The situation is different for GC4 and GC3, the two clusters closest (in projection) to the centre of Fornax. Their deprojected 3D distance is shown by the bottom horizontal dashed lines in the left and right panels of Fig. 2.8, respectively. Because of their proximity to the centre and their relatively large masses, GC3 and GC4 decay more quickly, and they need to have started their orbital evolution at ~ 1.6 kpc and ~ 1.0 kpc, respectively, in order to match their present-day position after ~ 10 Gyr.

How does including Galactic tides change these conclusions? We explore this by evolving each GC again, but placing the Fornax model in orbit around the Milky Way. We focus here on orbit 1, where the effects of tides are strongest. The resulting evolution of each cluster is shown by the coloured lines in Fig. 2.8. Cluster orbits are significantly affected by Galactic tides; however, the main effect is to increase the GCs' orbital eccentricity, while their orbital decay timescales remain much the same as in isolation. These results thus suggest that Galactic tides have only a minor effect on the dynamical friction evolution of GCs in Fornax over 10 Gyr, even in the case of a Galactic orbit with rather small pericentric distance.

The conclusions of Meadows et al. (2020) therefore appear to hold. Only GC3 and GC4 are expected to be affected by dynamical friction; their present-day positions are readily explained if their initial orbital radii was between 1-2 kpc. This is enough to reconcile the present-day radial distribution of GCs around Fornax with the cuspy dark matter halo profile expected in LCDM.

2.5 Summary and Conclusions

We have used N-body simulations to study the evolution of the Fornax dSph in the Galactic potential. Our main goal is to explore whether Galactic tides may help (i) to explain the relatively low dark matter content of Fornax compared with that expected from LCDM

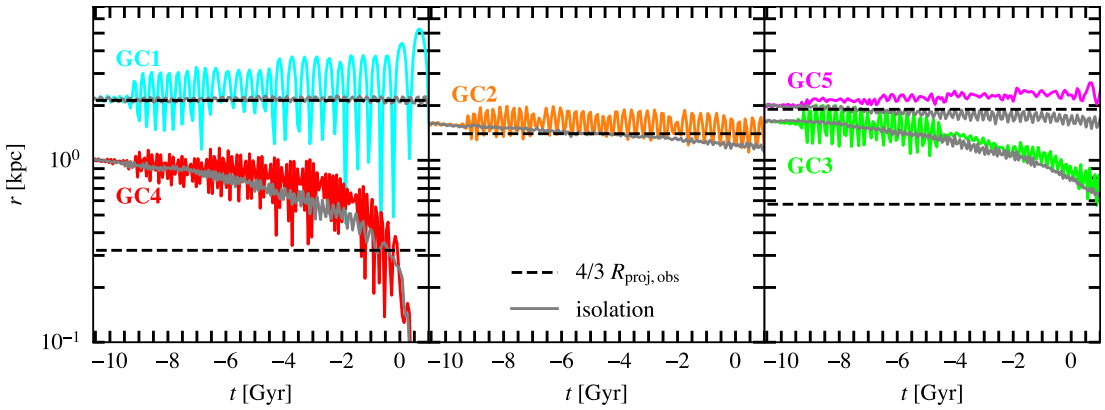

Figure 2.8: The evolution of the distance to the centre of Fornax for the five GCs. Coloured lines show the evolution in the presence of tides (orbit 1); grey curves correspond to runs in isolation. Initial radii are chosen so that in absence of tides, the GCs have decayed to approximately their currently observed projected radii in about 10 Gyr. The main effect of tides is to increase the GC orbital eccentricities (they are initially set on circular orbits); their effect on the orbital decay timescales seems minor at best.

cosmological hydrodynamical simulations of dwarf galaxy formation, and (ii) to reconcile the spatial configuration of its globular clusters with their apparently short dynamical friction orbital decay timescales. Our model assumes that Fornax is a dark-matter dominated system embedded in a cuspy NFW halo. Our main conclusions may be summarized as follows.

Using the latest available data on Fornax's sky position, distance, radial velocity and proper motions, together with a Galactic potential model that matches the most recent dynamical constraints, we conclude that the pericentric distance of Fornax's orbit is only loosely constrained. The main reason for this is the particular direction of Fornax's orbital velocity at present, which is anti-parallel to the Sun's Galactocentric velocity. This implies a large heliocentric tangential velocity, which translates into a sensitive dependence of Fornax's inferred Galactocentric velocity on its assumed distance. Indeed, a $\pm 8\%$ error in the distance translates into pericentric distances that may vary between ~ 50 and 130 kpc.

Assuming a pericentric distance at the small end of that range, our models suggest that a Fornax NFW halo model with $M_{200} = 1 \times 10^{10}\,\mathrm{M}_\odot$ (or, equivalently, $V_{\rm max} = 40\,\mathrm{km\,s^{-1}}$, consistent with the results of the APOSTLE suite of LCDM Local Group simulations) would be stripped of most of its dark mass over ~ 10 Gyr of evolution (over 4 full orbits in the assumed Galactic potential). The tidal mass loss would reduce $V_{\rm max}$ to roughly $\sim 23\,\mathrm{km\,s^{-1}}$, and the total enclosed mass within half-light radius of Fornax ($r_{1/2} \approx 1$ kpc) by $\sim 42\%$, bringing it into agreement with observational estimates.

Our models also indicate that most of the mass lost to stripping is *dark*, and that the total stellar component of Fornax is far less affected. Indeed, a stellar tracer modelled as a Sérsic model with $n = 0.81$ and $R_{1/2} = 0.61$ kpc (which matches fairly well the observed light profile of Fornax) would be hardly affected, losing less than 5% of its mass in the process. Stripped stars would form tidal tails around Fornax, but with an average surface brightness more than 1000 times fainter than Fornax's central value and therefore extremely challenging to detect. Our models show that the stellar component of Fornax inside at least ~ 3 kpc would show no obvious evidence of any tidal disturbance, again consistent with observations.

Similarly, the effect of Galactic tides on the dynamical friction decay times of Fornax's population of globular clusters is minor compared with models run in isolation. Thus a population of globular clusters with initial orbital radii between 1 and 2 kpc is consistent with their present-day spatial distribution, despite assuming a cuspy NFW halo.

All models implemented here assume tidal stripping in Fornax due to the gravitational

influence of the Milky Way only. We note that a massive nearby satellite as the LMC could have a non-negligible contribution to the gravitational potential felt by Fornax, modifying its orbital evolution from that presented here (see e.g., Erkal et al., 2019; Patel et al., 2020). Further uncertainties may arise from the still undetermined total mass of the Milky Way; the total mass considered in this work ($M_{200} \sim 1.15 \times 10^{12}\,\mathrm{M}_{\odot}$, McMillan (2011)) lies slightly above recent estimates provided by studies based on LMC analogues in cosmological simulations of the Local Group (Santos-Santos et al., 2020a) or stellar halo kinematics (Deason et al., 2021). We plan to consider these effects in future work.

We conclude that both the low dark matter content measured for the Fornax dSph and the radial distribution of its GC population are consistent with a scenario where Galactic tides are solely responsible for stripping a cuspy NFW halo with virial mass $10^{10}\,M_{\odot}$, as expected from abundance-matching arguments. Note that this scenario does not require a "core" but it does require a relatively small pericentric distance (~ 50 kpc) for tides to operate effectively. This is possible if Fornax's true Galactocentric distance is slightly lower than, but within the uncertainty of, current estimates. A tighter distance estimate would therefore provide a helpful check to the validity of this scenario. A further check could be provided by tighter constraints on the innermost mass profile. In the tidal scenario proposed here Fornax's halo is still cuspy; probes of the mass profile within a couple of hundred parsecs would be especially helpful in order to settle questions about the presence of a core or a cusp in the Fornax dSph.

Acknowledgements

This work used the DiRAC@Durham facility managed by the Institute for Computational Cosmology on behalf of the STFC DiRAC HPC Facility (www.dirac.ac.uk). The equipment was funded by BEIS capital funding via STFC capital grants ST/K00042X/1, ST/P002293/1, ST/R002371/1 and ST/S002502/1, Durham University and STFC operations grant ST/R000832/1. DiRAC is part of the National e-Infrastructure.

RE acknowledges support provided by a CITA National Fellowship and by funding from the European Research Council (ERC) under the European Unions Horizon 2020 research and innovation programme (grant agreement No. 834148).

AF is supported by a UKRI Future Leaders Fellowship [grant number MR/T042362/1] and Leverhulme Trust.

ISS is supported by the Arthur B. McDonald Canadian Astroparticle Physics Research Institute.

Chapter 3

Galactic tides and the Crater II dwarf spheroidal: a challenge to LCDM?

Text from this chapter was originally published in Monthly Notices of the Royal Astronomical Society: 2022, vol. 512, issue 4, pp 5247-5257. Published by Oxford University Press on behalf of the Royal Astronomical Society.

https://doi.org/10.1093/mnras/stac653

Authors: Alexandra Borukhovetskaya[1], Julio F Navarro[1], Raphaël Errani[2], and Azadeh Fattahi[3]

3.1 Abstract

The unusually low velocity dispersion and large size of Crater II pose a challenge to our understanding of dwarf galaxies in the Lambda Cold Dark Matter (LCDM) cosmogony. The low velocity dispersion suggests either a dark halo mass much lower than the minimum expected from hydrogen cooling limit arguments, or one that is in the late stages of extreme tidal stripping. The tidal interpretation has been favoured in recent work and is supported by the small pericentric distances consistent with available kinematic estimates. We use *N*-body simulations to examine this interpretation in detail, assuming a Navarro-Frenk-White (NFW) profile for Crater II's progenitor halo. Our main finding is that, although the low velocity dispersion can indeed result from the effect of tides, the

[1]Department of Physics and Astronomy, University of Victoria, Victoria, BC V8P 5C2, Canada
[2]Université de Strasbourg, CNRS, Observatoire astronomique de Strasbourg, UMR 7550, F-67000 Strasbourg, France
[3]Institute for Computational Cosmology, Department of Physics, University of Durham, South Road, Durham DH1 3LE, UK

large size of Crater II is inconsistent with this hypothesis. This is because galaxies stripped to match the observed velocity dispersion are also reduced to sizes much smaller than the observed half-light radius of Crater II. Unless its size has been substantially overestimated, reconciling this system with LCDM requires that either (i) it is not bound and near equilibrium (unlikely, given its crossing time is shorter than the time elapsed since pericentre), or that (ii) its progenitor halo deviates from the assumed NFW profile. The latter alternative may signal that baryons can affect the inner halo cusp even in extremely faint dwarfs or, more intriguingly, may signal effects associated with the intimate nature of the dark matter, such as finite self-interactions, or other such deviations from the canonical LCDM paradigm.

3.2 Introduction

The Crater II dwarf spheroidal (dSph) is a distant Milky Way (MW) satellite discovered in imaging data from the ATLAS survey at the VLT Survey Telescope by Torrealba et al. (2016). Its unusual properties were immediately apparent. Although its total luminosity ($M_V \sim -8$) is comparable to that of the faintest "classical" dSphs, such as Draco and Ursa Minor, Crater II's enormous size (projected half-light radius, $R_{1/2} \sim 1$ kpc, and spanning nearly 5° across the sky) is comparable to that of Fornax, a dSph more than 100 times more luminous. Indeed, Crater II is one of the lowest surface brightness galaxies ever discovered, several decades fainter than the ultra-diffuse galaxy population identified by surveys such as Dragonfly (Van Dokkum et al., 2015).

These unusual photometric properties are compounded by equally unusual kinematics. The most recent estimates put the velocity dispersion of its stars at $\sigma_{\rm los} \approx 2.3\,{\rm km\,s^{-1}}$, one of the lowest amongst all known dSphs but still large enough to imply the presence of large amounts of dark matter ($M/L \approx 50$: Caldwell et al. (2017); Fu et al. (2019); $M/L \approx 30$: Ji et al. (2021)). Such uncommon properties point to atypical formation paths. Suggestions include the possibility that Crater II formed in a halo of unusually low density (Amorisco, 2019), or that its structure was severely affected by Galactic tides after formation, or both.

The latter explanation is currently the most popular. Frings et al. (2017) and Applebaum et al. (2021), for example, report simulations of satellites whose properties are similar to those of Crater II after undergoing severe tidal stripping. Similar conclusions were reported by Sanders et al. (2018), who cautioned, however, that it was difficult to account simultaneously for the velocity dispersion and size of Crater II in cuspy dark matter halos

such as those expected in the Lambda Cold Dark Matter (LCDM) cosmogony (Navarro et al., 1996b, 1997). Fattahi et al. (2018) extrapolated the "tidal tracks" of Peñarrubia et al. (2008) and Errani et al. (2015) to reach a similar conclusion, noting that explaining Crater II through tidal stripping implied the rather extreme case of a progenitor which had lost more than 99% of its initial stellar content to tides.

Despite these difficulties, consensus for a tidal interpretation of the unusual properties of Crater II (and for those of Antlia II, another "feeble giant" MW satellite; Torrealba et al., 2019) seems to have emerged. In the case of Antlia II, the case for tides has been strengthened by the detection of a clear velocity gradient aligned with the orbital path indicated by the latest proper motions from Gaia (Ji et al., 2021).

No such gradient, however, is clearly present in Crater II, at least over the area surveyed spectroscopically. This is perhaps not surprising: Crater II's negative Galactocentric radial velocity suggests that it is at present just past apocentre; together with its large distance (~ 120 kpc), this implies that its most recent pericentric passage must have occurred about ~ 1 Gyr ago. As discussed[4] by Peñarrubia et al. (2009), the inner regions of a bound tidal remnant relax quickly, pushing all signatures of tidal disturbance to regions where the local crossing time exceeds the time elapsed since pericentre, $t - t_p$ (see their Eq. 5). Assuming $(t - t_p) \sim 1$ Gyr, and using the measured velocity dispersion, this implies that the inner $R \lesssim 1.3$ kpc should be close to dynamical equilibrium. This region is similar to the area over which radial velocities are available (~ 0.65 deg from the dwarf's centre; Ji et al., 2021).

This insight simplifies considerably the analysis, as it disfavours interpretations where the singular properties of Crater II are due to large, transient departures from equilibrium. If Galactic tides have indeed been responsible for shaping Crater II, then its properties must be consistent with the structure of the remnants of tidally stripped LCDM subhalos, an issue that has been studied extensively over the years using N-body simulations (see; e.g., Hayashi et al., 2003; Peñarrubia et al., 2008; Errani et al., 2015). The latest work suggests that LCDM subhalos, if well approximated by cuspy Navarro-Frenk-White (hereafter NFW, see Navarro et al., 1996b, 1997) profiles, should almost always leave behind a bound remnant (Peñarrubia et al., 2010; Van Bosch and Ogiya, 2018; Van Bosch et al., 2018). The remnant properties are fully specified by the initial characteristic crossing time of the subhalo, by the number of orbits completed, and by the orbital time at pericentre (Errani and Navarro, 2021).

This discussion thus calls into question whether Crater II is actually a stellar system

[4] See also earlier work by Aguilar and White (1986) and Navarro (1990).

inhabiting a subhalo nearing full tidal disruption. Are the peculiar size and kinematics of Crater II actually consistent with the tidal remnants of LCDM halos?

We address this issue here using N-body simulations of the tidal evolution of NFW subhalos in orbits chosen to match the observed present-day position and velocity of Crater II in the MW halo potential. We choose cuspy NFW halos for this work not only because this is one of the best tested LCDM predictions, but also because the halo inner structure of galaxies as faint as Crater II should be relatively unaffected by the effects of baryons, which could in principle alter the inner density cusp in more massive galaxies (see; e.g., Navarro et al., 1996a; Read and Gilmore, 2005a; Pontzen and Governato, 2012; Di Cintio et al., 2014, and references therein).

This paper is organized as follows. We first summarize the observed properties of Crater II, as well as our numerical setup, in Sec. 3.3. The results of the simulations, for both dark matter and stellar tracers, are analysed and presented in Sec. 3.4. We end with a brief summary and a discussion of our results in a cosmological context in Sec. 3.5.

3.3 Observations and Simulations

This section summarises the observed properties of Crater II, and outlines the numerical setup of the N-body simulations used to model the tidal evolution of Crater II in the gravitational potential of the Milky Way.

3.3.1 Observed properties of Crater II

The photometric properties of Crater II were estimated by Torrealba et al. (2016) in its discovery paper. These authors estimate a projected half-light radius of order $R_{1/2} \sim 1.066$ kpc by fitting a Plummer model to star counts. We reproduce their published data in the left panel of Fig. 3.1, which shows that the number density profile spans only a factor of ~ 2 in density before becoming dominated by foreground stars. This results in large uncertainties in estimates of the half-light radius, depending on the assumed profile shape. This is illustrated by the grey and dark red lines in Fig. 3.1, which both fit the observations fairly well although their half-light radii (as marked by triangles) differ by a factor of ~ 3. A much better constrained parameter is the core radius, $R_c \approx 700$ pc, defined as the radius where the surface brightness of a galaxy drops by a factor of two from the central value.

Stellar half-light radii are also difficult to measure in numerical simulations, partic-

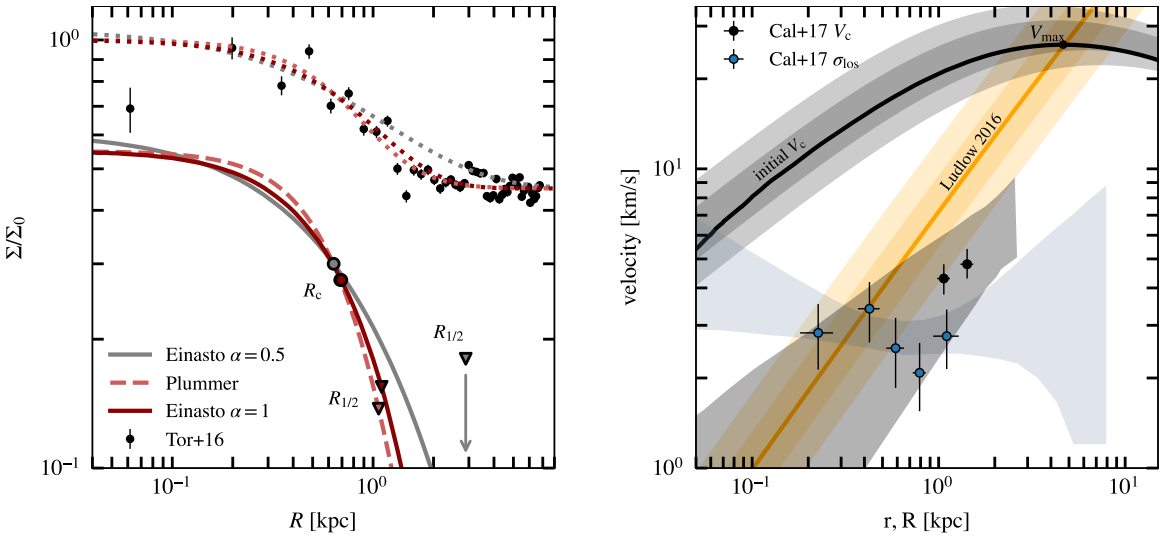

Figure 3.1: Observed structural parameters of Crater II. The left panel shows the observed surface brightness taken from Torrealba et al. (2016) together with fits adopting different models for the density profile of the stellar component. Light red curves correspond to a Plummer (1911) fit with the parameters of Torrealba et al. (2016). Dotted profiles include the contribution of a constant background level equal to 0.45× the central surface brightness, Σ_0. Dark red curves correspond to an $\alpha = 1$ Einasto profile (Eq. 3.2), which fits the Plummer projected density profile quite well. Grey curves show an $\alpha = 0.5$ Einasto profile with similar core radius, R_c (circles), but a much larger half-light radius ($R_{1/2}$, triangles) than the other profiles. All seem to provide acceptable fits to the data, implying that, unlike R_c, Crater II's $R_{1/2}$ is not well constrained. The right panel shows the measured velocity dispersion of Crater II (blue circles, and shaded area) as well as corresponding estimates for the circular velocity , taken from Caldwell et al. (2017). The black line (and shaded area) shows the circular velocity profile of our Crater II NFW model before stripping, motivated by results from the APOSTLE simulation for galaxies of similar stellar mass (Fattahi et al., 2018). The yellow line shows the r_{max}-V_{max} relation for LCDM halos at $z = 0$ from Ludlow et al. (2016). The inner shaded bands correspond to ±1-sigma scatter in concentration and the outer, fainter bands to ±2-sigma.

ularly in cases where tides have led to substantial amounts of mass loss. In these cases, estimated $R_{1/2}$ values depend critically on which stars are included in the analysis. Including weakly bound, or escaping, stars, for example, typically results in poorly-defined estimates vulnerable to sizeable transient fluctuations. Because of this, we shall adopt R_c (marked with circles in the left panel of Fig. 3.1) rather than $R_{1/2}$ (triangles) as the characteristic photometric radius of Crater II, although our main conclusions do not depend critically on this choice. For a Plummer model, which is often adopted in observational studies to fit the stellar density profile, $R_c \approx 0.6\, R_{1/2}$.

The right-hand panel of Fig. 3.1 summarizes some of the kinematic information available for Crater II, compiled from Caldwell et al. (2017). (We shall hereafter use lowercase r to denote 3D radii and uppercase R for projected radii.) The observed velocity dispersion profile is shown in grey-blue. The black circles indicate corresponding circular velocity estimates obtained using the Wolf et al. (2010) and Walker et al. (2009) mass estimators [5].

For comparison, we show with a thick black curve the (NFW) circular velocity profile expected for an *isolated* dwarf galaxy of stellar mass comparable to that of Crater II (assumed to be $M_\star \approx 2.56 \times 10^5\, \mathrm{M}_\odot$, see Sec. 3.3.4 for details). According to the results of the APOSTLE cosmological hydrodynamical simulations (Fattahi et al., 2018), galaxies like Crater II are expected to form in halos with peak circular velocity $V_{\rm max} \sim 26\, \mathrm{km\, s^{-1}}$, or a virial[6] mass $M_{200} \sim 2.7 \times 10^9\, \mathrm{M}_\odot$. For such model to be viable, it is clear from Fig. 3.1 that Galactic tides must have led to a large depletion of the original dark matter content of Crater II.

3.3.2 Milky Way potential model

The Milky Way is modelled as an analytical, static potential, consisting of an axisymmetric two-component Miyamoto and Nagai (1975) disk, a Hernquist (1990) bulge and an NFW dark matter halo. These models and their parameters are as summarised in section 1.4.2.

3.3.3 Orbits

The orbit of Crater II in the assumed Milky Way potential may be estimated from its present-day Galactocentric position and velocity, as inferred from its sky position, radial

[5] These mass estimates are supported by the full Jeans modelling of Caldwell et al. (2017) (shaded region).

[6] We define virial quantities as those within a sphere of mean density equal to 200 times the critical density for closure, $\rho_{\rm crit} = 3H_0^2/8\pi G$. We use the subscript "200" to indicate virial quantities.

Table 3.1: Current observational constraints, as well as parameters of the three orbits explored using N-body simulations in this study. The Fritz et al. (2018) proper motions are followed first by the statistical error and second by the systematic error. Orbits 1 and 2 are the orbits corresponding to the 16th and 84th percentile of the distribution in pericentres obtained with the proper motions of Kallivayalil et al. (2018). Orbit 3 is the orbit corresponding to the median observed quantities of McConnachie and Venn (2020). Pericentres and apocentres are computed for the Milky Way potential model discussed in section 3.3.2.

observation	α	δ	distance (kpc)	μ_{α^*} (mas yr^{-1})	μ_δ (mas yr^{-1})	v_r (km s^{-1})
	$11^h49^m12^s$ (1)	$-18°24'0''$ (1)	117.5 ± 1.1 (1)	-0.246 ± 0.052 (3)	-0.227 ± 0.026 (3)	87.5 ± 0.4 (2)
				$-0.184 \pm 0.061 \pm 0.035$ (4)	$-0.106 \pm 0.031 \pm 0.035$ (4)	
				-0.07 ± 0.02 (5)	-0.11 ± 0.01 (5)	

(1) Torrealba et al. (2016), (2) Caldwell et al. (2017), (3) Kallivayalil et al. (2018), (4) Fritz et al. (2018), (5) McConnachie and Venn (2020)

model parameters	pericentre (kpc)	apocentre (kpc)	distance (kpc)	μ_{α^*} (mas yr^{-1})	μ_δ (mas yr^{-1})	v_r (km s^{-1})
orbit 1	4.23	130	116	-0.169	-0.267	87.8
orbit 2	15.5	133	117	-0.102	-0.225	87.2
orbit 3	37.4	139	118	-0.07	-0.11	87.5

velocity, distance, and proper motion, assuming that the effects of dynamical friction can be neglected. Of the observed parameters (summarised in Table 3.1), the proper motions contribute the majority of the uncertainty budget.

Assuming $\mu_{\alpha^*} = -0.246 \pm 0.052$ mas yr^{-1}, $\mu_\delta = -0.227 \pm 0.026$ mas yr^{-1}(Kallivayalil et al., 2018)[7], for example, these uncertainties result in a fairly broad distribution of possible pericentric and apocentric distances, shown by the pink histograms in Fig. 3.2. Different estimates for the proper motion will, of course, yield different orbits. We show also in Fig. 3.2 the pericentric and apocentric distributions corresponding to proper motion estimates from McConnachie and Venn (2020) and Fritz et al. (2018), illustrating that a wide range of orbits are permissible given the current data.

Because of the large allowed range, we have explored three different orbits, varying mainly the orbital pericentric distance (the most critical parameter for tidal effects), $r_{\rm peri} =$ 4.2, 16, and 37 kpc. The corresponding orbits are hereafter referred to as orbits 1, 2 and 3, respectively, with parameters summarised in Table 3.1. Initial conditions for the orbits of N-body runs are obtained by integrating them backwards in time for 10 Gyr. The shape of the resulting orbits are shown in Fig. 3.8 in a co-ordinate system where the Sun is located at $(X, Y, Z)_\odot = (-8.3, 0, 0)$ kpc, and the velocity of the local standard of rest is in the positive Y direction.

[7]Where with μ_{α^*} we designate the proper motion in α including the $\cos(\delta)$ factor.

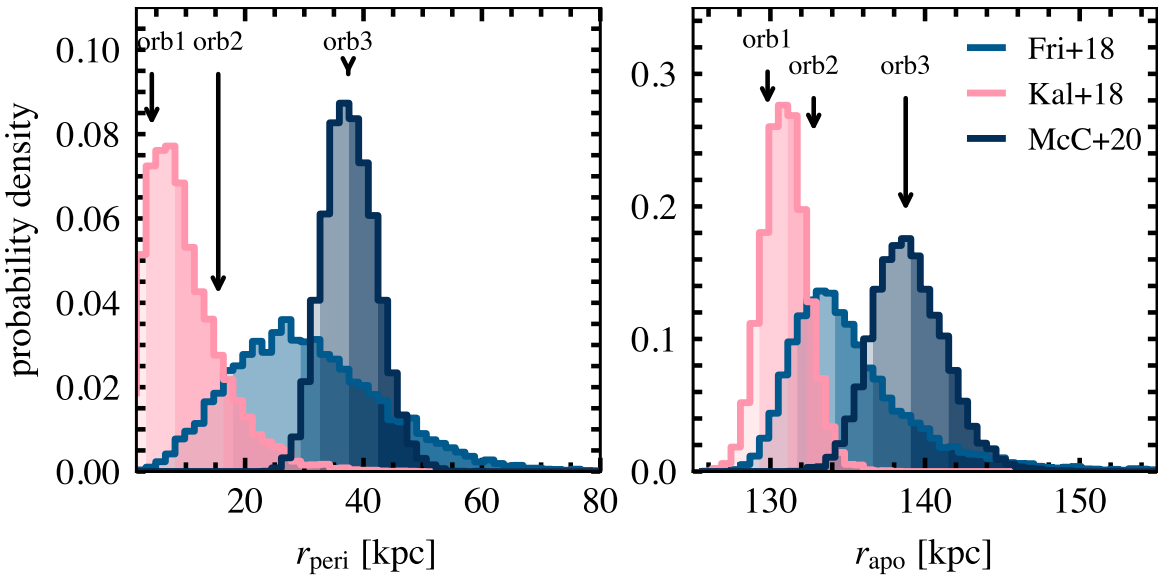

Figure 3.2: The probability distributions of Crater II pericentric (left panel) and apocentric (right panel) distances obtained from the proper motions, distance, and radial velocity, together with their reported uncertainties. Each colour corresponds to different proper motion estimates, from Kallivayalil et al. (2018, pink), Fritz et al. (2018, blue), and McConnachie and Venn (2020, black). The three orbits selected to explore the available parameter space are shown with arrows pointing down. Regions beneath the histograms darken at the 16th, 50th, and 84th percentile.

3.3.4 Crater II model

3.3.4.1 Dark matter component

The Crater II halo is modelled as an equilibrium N-body realisation of the NFW density profile,

$$\rho_{\rm NFW}(r) = \frac{M_{200}}{4\pi r_s^3} \frac{(r/r_s)^{-1}(1+r/r_s)^{-2}}{[\ln(1+c) - c/(1+c)]}. \tag{3.1}$$

This profile is fully specified by two parameters; e.g., a virial mass, M_{200}, and concentration, $c = r_{200}/r_s$, or, alternatively, by a maximum circular velocity, $V_{\rm max}$, and the radius at which it is reached, $r_{\rm max}$.

Cosmological hydrodynamical simulations, such as the APOSTLE suite of Local Group simulations (Sawala et al., 2016; Fattahi et al., 2016a), have shown that $V_{\rm max}$ correlates strongly with galaxy stellar mass, $M_\star$ (see also Santos-Santos et al., 2021, for a recent compilation). We adopt a stellar mass for Crater II of $M_\star = 2.56 \times 10^5\,{\rm M}_\odot$, computed from the absolute magnitude of Torrealba et al. (2016) and assuming $M_\star/L_V = 1.6$, typical of dwarf galaxies in the Local Group (Woo et al., 2008).

Table 3.2: Current properties of Crater II ($M_\star, V_{1/2}, r_{1/2}$) and inferred structural parameters at infall of the dark matter halo (V_{max}, r_{max}) and stellar component ($\alpha, R_{core}, M_\star$). Half-light radius $r_{1/2}$ and circular velocity $V_{1/2}$ at the half-light radius are as in Caldwell et al. (2017), taking $r_{1/2} = 4/3R_{1/2}$.

observation	$M_\star$ ($10^5\,M_\odot$)	$V_{1/2}$ (km s^{-1})	$r_{1/2}$ (kpc)
	2.56	$4.8^{+0.6}_{-0.5}$	1.421 ± 0.112

initial halo	V_{max} (km s^{-1})	r_{max} (kpc)
	25.9	4.70

initial stars	α	R_{core} (kpc)
E1	1	0.46
E2	1	0.91
E3	1	1.79

As in Borukhovetskaya et al. (2022a), we estimate V_{max} (before tidal effects) using the empirical fit[8] to the $M_\star$-V_{max} correlation in APOSTLE from Fattahi et al. (2018). The characteristic radius r_{max} then follows from the Ludlow et al. (2016) parametrisation of the LCDM halo mass-concentration relation at redshift $z = 0$. As listed in Table 3.2, the resulting NFW profile has $V_{max} = 25.9$ km s^{-1} and $r_{max} = 4.7$ kpc, or, in terms of virial mass and concentration, $M_{200} = 2.72 \times 10^9\,M_\odot$ and $c = 13.6$. The corresponding circular velocity profile is shown in the right-hand panel of Fig. 3.1.

3.3.4.2 Stellar component

The stellar component of Crater II is modelled assuming that it contributes negligibly to the total gravitational potential. We consider, in particular, stellar components modelled as Einasto profiles (Einasto, 1965),

$$\rho_E(r) = \rho_{E0} \exp[-(r/r_E)^\alpha], \tag{3.2}$$

with $\alpha = 1$ (i.e., exponential spheres) and three different core radii: $R_c = 0.5$, 0.9, and 1.7 kpc. These values have been chosen to bracket the observed present-day core radius

[8] $M_\star = M_0 v^\alpha \exp(-v^\gamma)$, where $v = V_{max}/50$ km s^{-1} , and $(M_0, \alpha, \gamma) = (3.0 \times 10^8\,M_\odot, 3.36, -2.4)$.

of Crater II, which is ~ 0.7 kpc. These three stellar models are hereafter referred to as E1, E2, and E3 respectively, and their parameters are summarised in Table 3.2. Core radii are related to the Einasto scale radius, $r_{\rm E}$, by the relation $R_{\rm c} \approx 1.24\, r_{\rm E}$. In practice, stars are modelled[9] by attaching a probability to each dark matter particle, following the appropriate distribution function (see; e.g., Bullock and Johnston, 2005). Using this approach, the probability of each N-body particle to represent a star relates the dark matter and stellar energy distributions as

$$P(E) \propto (\mathrm{d}N/\mathrm{d}E)_{\star}/(\mathrm{d}N/\mathrm{d}E). \tag{3.3}$$

The underlying energy distributions are computed numerically as outlined in Errani and Peñarrubia (2020). These probabilities are computed at infall and followed throughout the orbit, where at any point the stellar structure and kinematics may be recovered from the dark matter distribution by applying the individual stellar probabilities as weights.

3.3.5 Simulation code

We use 10^7-particle N-body realisations of NFW halos, computed using the `Zeno`[10] software package developed by Joshua Barnes at the University of Hawaii. This software uses Monte Carlo sampling of a given distribution function to generate systems in virial equilibrium.

We allow the halo to fully relax prior to introducing it into the MW potential, by running it first in isolation for 5 Gyr using the publicly available `GADGET-2` simulation code (Springel, 2005). Once the halo has relaxed, the N-body model is evolved on each of the orbits described in section 3.3.3 and in the potential of Section 3.3.2 for ~ 10 Gyr. Forces between particles are smoothed with a Plummer-equivalent softening length of $\epsilon_{\rm P} = 7$ pc and we consider our results converged outside $r_{\rm conv} = 84$ pc[11].

3.4 Results

Having introduced our numerical setup, we examine next the tidal evolution of Crater II. We discuss first the evolution of the dark matter (Sec. 3.4.1), before discussing the evolution of embedded stellar components in Sec. 3.4.2.

[9] For details see the publicly available implementation of Errani and Peñarrubia (2020): `https://github.com/rerrani/nbopy`

[10] `http://www.ifa.hawaii.edu/faculty/barnes/zeno/`

[11] We define the radius of convergence, $r_{\rm conv}$, as the innermost radius where the initial circular velocities deviate by less than $\sim 1\%$ from the target NFW profile.

3.4.1 Tidal effects on the dark matter component

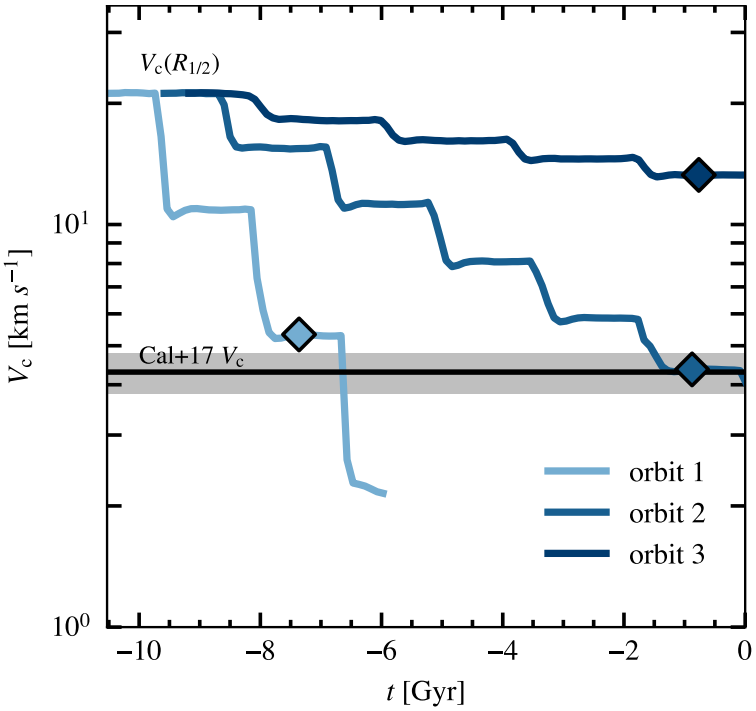

Figure 3.3: Evolution of the circular velocity at the estimated half-light radius of Crater II (i.e., V_c at $r = R_{1/2} = 1.066$ kpc) for our halo model in each of the three different orbits explored in this work; lighter shades correspond to smaller pericentres. The horizontal black solid line and grey shaded region represent the observational constraint on V_c, as well as the $\pm 1\sigma$ uncertainty interval, taken from Caldwell et al. (2017). Diamonds indicate the snapshot(s) we identify for comparison with observational data. Note that, on orbit 3, our chosen halo does not get stripped enough to bring the system into agreement with the observed constraint after orbiting for ~ 10 Gyr.

The evolution of the circular velocity within $R_{1/2} = 1.066$ kpc of our Crater II halo models is shown in Fig. 3.3. Different colors correspond to different orbits. A horizontal black line indicates, for reference, the estimated circular velocity from Caldwell et al. (2017).

As tides strip the system, the circular velocity decreases continuously, with abrupt drops corresponding to subsequent pericentric passages. The magnitude of the decrease is heavily dependent on the assumed pericentric distance. We see that for a pericentre as large as ~ 40 kpc (orbit 3), tidal effects are not enough to reduce the circular velocity enough to match the observational estimate.

The mass loss on orbits 1 and 2, with pericentres of 4 and 16 kpc, respectively, seems

large enough to bring the initial halo into agreement with the observed estimate in less than 10 Gyr. This happens after only 2 pericentric passages for orbit 1, but it takes 5 full orbits for orbit 2. We note that bringing the assumed halo into agreement with the observed V_c implies a dramatic amount of mass loss: only 0.2% of the initial dark mass remains bound when $V_c(R_{1/2})$ approaches the observed value of $\sim 4\,\mathrm{km\,s^{-1}}$.

We conclude that it is in principle possible to explain the unusually low velocity of Crater II if the dSph is placed on orbits with pericentric distances of order ~ 15 kpc or less. This value is consistent with current observational estimates, though tighter constraints on the allowed pericentres should be able to rule out this scenario if larger pericentres are found to be favoured.

3.4.2 Tidal effects on the stellar component

The stellar components are also affected by tidal losses, to an extent that depends on the assumed initial density profile and radial segregation of stars relative to the dark matter (see Errani et al., 2022, for a more detailed discussion). We focus here on models E1, E2, and E3 – exponential spheres which differ mainly in their initial core/half-light radii (see Sec. 3.3.4 for details). We limit our analysis to the evolution on orbit 2, but very similar results are obtained for orbit 1, albeit on a compressed timescale.

We begin by tracking the evolution of the core radius, R_c, and of the line-of-sight velocity dispersion, σ_{los}, of the stars (averaged within R_c) in Fig. 3.4. Results for E1, E2, and E3 are shown with different coloured tracks, starting with the initial conditions (triangles) and ending, after 5 pericentric passages, on the coloured circles highlighted in black. Each small circle along the tracks indicates a subsequent apocentric passage. The "target" Crater II core radius and velocity dispersion inside the core radius are shown by a red circle with a blue error bar.

Interestingly, none of the stellar tracks seems to approach the observed location of Crater II in the R_c-σ_{los} plane. As the system loses mass, the velocity dispersions decrease, but so do the core radii of the stars. By the time the velocities approach the observed value, the core radii are almost 4 times smaller than observed. This result applies to all 3 stellar models, regardless of their initial radius.

Because of this discrepancy, reproducing the observed surface density profile of stars in Crater II is not possible, as shown in the left-hand panel of Fig. 3.5. The solid curves in that figure indicate the final density profile of bound stars in orbit 2, normalized to match approximately the central observed value for Crater II with background. Dotted curves

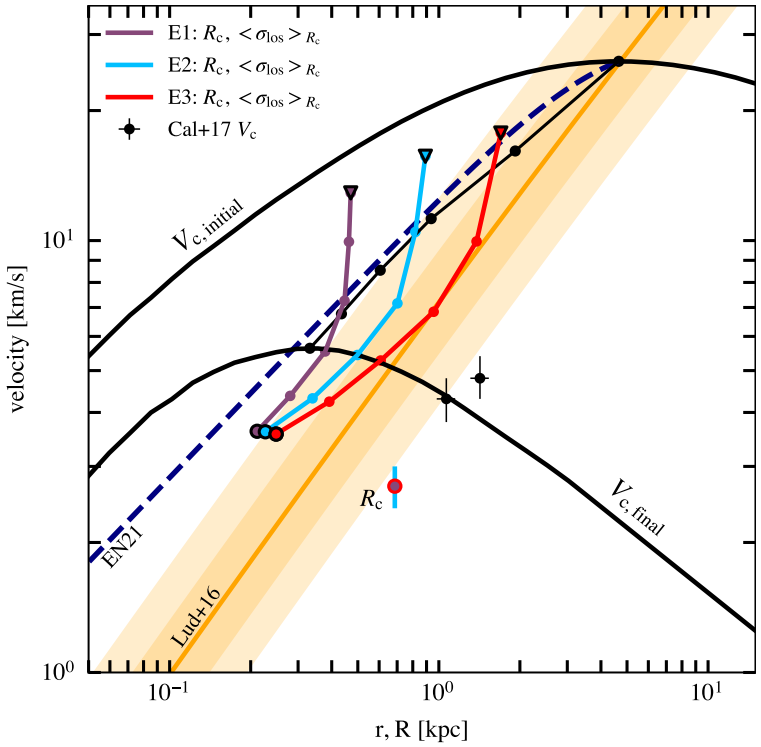

Figure 3.4: Evolution of the core radius, R_c, and line-of-sight velocity dispersion, σ_{los}, for three different stellar component models (E1, E2, E3) on orbit 2. Triangles indicate the initial values, and coloured circles the values at the final snapshot. The coloured lines trace the evolution of these parameters as a function of time; each small circle marks subsequent apocentric passages. The orange line shows the r_{max}-V_{max} relation (plus 1σ and 2σ scatter bands in concentration) expected for LCDM halos at $z = 0$ (Ludlow et al., 2016, in orange). The initial and final circular velocity of the assumed Crater II progenitor halo is shown by the solid black curves. Black circles with error bars show the observed V_c constraint from Caldwell et al. (2017). The blue-red circle indicates the observed values of R_c and σ_{los} for Crater II. The dashed curve shows the "tidal track" of Errani and Navarro (2021), which traces quite well the evolution of r_{max} and V_{max} of the halo (shown as a solid black line with circles at each apocentric passage) as a function of time.

in Fig. 3.5 show the same profiles after adding a constant background of $\Sigma_{bck} = 0.45\Sigma_0$. The bound stellar remnant has a similar size in all cases, and is clearly too small to match the observed profile for Crater II.

This result is general, and not just particular to our choices of density profile, or initial radial segregation. This may be seen by noticing that, after substantial mass loss, the stellar tracks of all three systems follow the tidal track of the remnant dark matter component, indicated by the dashed black line in Fig. 3.4.This track follows the evolution of the remnant's r_{max} and V_{max} characteristic parameters which, by the end of the simulation

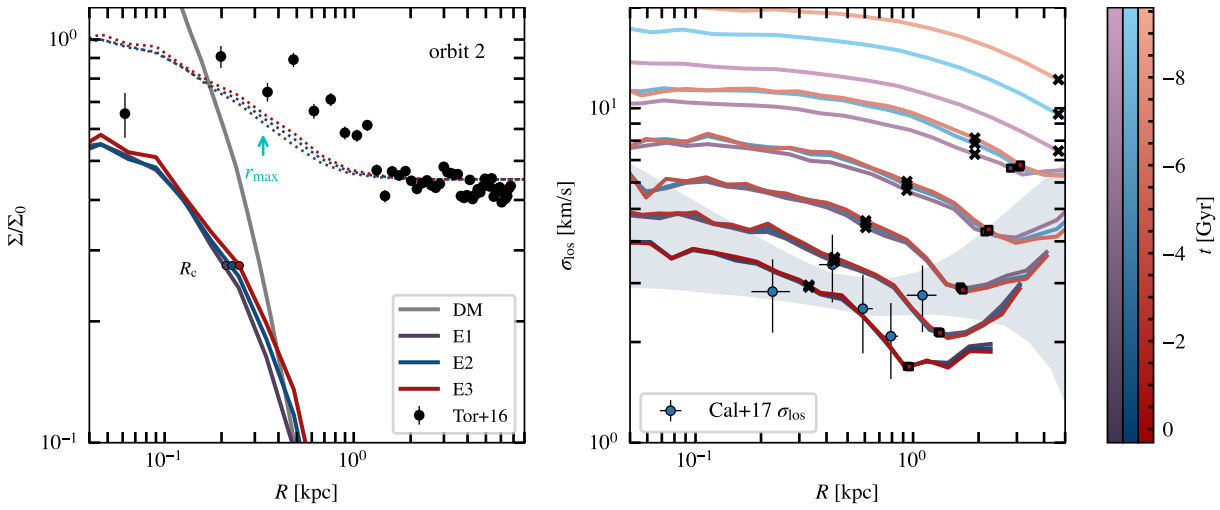

Figure 3.5: *Left:* Surface density profile of the bound remnant of stellar component models E1, E2, and E3, at the final snapshot identified for orbit 2, normalized to match the observed central density, Σ_0. Note that the core radii are much smaller than observed, despite the wide range of initial core radii ($\sim$ 400 pc to $\sim$ 2 kpc) sampled by the E1, E2, and E3 models. The characteristic radius of the remnant halo, r_{max}, shown by an arrow, is a good indicator of the tidal truncation radius of the system. The dark matter halo projected density is drawn for reference in grey. *Right:* Line-of-sight velocity dispersion profiles for the bound constituents of the E1, E2, E3 models, at each subsequent apocentric passage (see colour coding, where $t = 0$ is the "final" snapshot of orbit 2). Model velocities roughly match the observed values at the final time (bottom profiles), although the sharp tidal truncation results in a sharp decline in σ_{los} outside r_{max} (marked with an "X" on each curve). The upturn in the outer regions is due to escaping stars moving away from the remnant. Squared symbols in each profile identify the location of that feature with the radius where the local crossing time equals the time elapsed since pericentre. See text for more details. Blue circles are observed values of σ_{los} for Crater II, taken from Caldwell et al. (2017).

on orbit 2, has seen its V_{max} decrease by a factor of 5 and its r_{max} by a factor of 14. More importantly, as discussed by Errani and Navarro (2021), the remnant subhalo approaches a mass profile that is well approximated by an "exponentially truncated cusp", with r_{max} roughly delineating a "tidal truncation" radius.

The tidal truncation is easy to spot in the right-hand panel of Fig. 3.5, where we plot the line-of-sight velocity dispersion profiles of the bound stellar remnants at various times during the evolution. Velocity dispersions are roughly constant in the inner regions, but drop sharply outside r_{max}, the location of which is marked with an "X" symbol on each curve. The decline is reversed and the velocity dispersion rises in the outermost parts because of the presence of weakly-bound stars moving radially outward. The position

of this upturn approximately coincides with the location where the local crossing time equals the time elapsed since the previous pericentric passage, as discussed by Peñarrubia et al. (2009). The locations of this "break radius", computed[12] as $R_b = C\,\sigma_0\,(t - t_p)$ (where $C = 0.35$ and σ_0 is the central line of sight velocity dispersion computed as the average within $1/2\ r_{max}$), are indicated by small squares on each of the curves shown in the right-hand panel of Fig. 3.5.

In other words, in these late stages of tidal stripping, the size of the stellar component cannot exceed r_{max} because there is little bound mass left outside r_{max} (see, also, Kravtsov, 2010; Errani and Navarro, 2021). Indeed, an exponential cusp profile has only $\sim 13\%$ of mass outside $2\,r_{max}$, and just $\sim 3\%$ outside $3\,r_{max}$. This also readily explains why all three stellar models converge to a remnant with the same R_c and σ_{los}, regardless of their initial size. We emphasize that this is a general result; the results for other orbits are shown in Fig. 3.9 and results for an alternate density profile in Fig. 3.10. We discuss next our results in the context of earlier work, as well as the implications of our findings for the interpretation of satellites like Crater II in a cosmological context.

3.4.3 Comparison with earlier work

The findings discussed above seem to contradict the results of Frings et al. (2017) and of Applebaum et al. (2021), who used simulations of tidally stripped satellites in a cosmological context to argue that it is possible to form Crater II-like satellites in LCDM cosmological simulations. We examine the reasons for the disagreement next, but emphasize that the discussion of their work relates *only* to their claims regarding Crater II-like systems. This discussion is not meant as wholesale criticism of their work, but rather as seeking a plausible explanation of why our conclusions differ from theirs on this particular topic.

We begin our discussion with an analysis of the results reported by Frings et al. (2017). Their "satellites I and II", in particular, seem to increase substantially in size as their halos are tidally stripped, at odds with our results. This "tidal expansion", however, occurs only when the orbit chosen leads to extreme tidal stripping (orbit V in the notation of Frings et al., 2017).

Satellite I inhabits a halo with a pronounced "core" in the density profile, and thus differs from the NFW halo models studied here (Macciò et al., 2017). For "cored" halos, tidal expansion of its stellar component under extreme tidal stripping is actually expected

[12]Note that the value of the constant $C = 0.35$ used here differs from the $C = 0.55$ value of Eq.5 in Peñarrubia et al. (2009) because in that paper R_b refers to the location of an upturn in the surface brightness profile, whereas here we refer to an upturn in the σ_{los} profile.

(see; e.g., Errani et al., 2015; Sanders et al., 2018). Furthermore, satellite I is a fairly massive satellite with a final velocity dispersion of $\sim 8\,\mathrm{km\,s^{-1}}$, much higher than Crater II, so there is no obvious conflict with our conclusions.

Satellite II, on the other hand, is less massive, and its halo has a less obvious core after being subjected to tides. This satellite also "tidally expands" when subject to extreme stripping (i.e., orbit V), leaving behind a stellar remnant with $M_\star \sim 2.1 \times 10^4\,\mathrm{M_\odot}$, $\sigma_{\rm los} \sim 2.5\,\mathrm{km\,s^{-1}}$, and a large half-light radius, $r_{\rm h} \sim 1.2\,\mathrm{kpc}$ (see Fig. 4, 9 in Frings et al., 2017). At face value, these properties are comparable to the properties of Crater II, and the large size[13], in particular, seems at odds with our results.

However, satellite II on orbit V is stripped so severely that the reported structural properties of the stellar component are unlikely to be robust. Evidence for this comes from apparent inconsistencies between the properties of the stellar and dark matter components. For example, the total circular velocity at the stellar half-light radius is only $\sim 1\,\mathrm{km\,s^{-1}}$ (see Fig. 11 in Frings et al., 2017), over a factor of 4 smaller than the $V_{\rm c}(r_{\rm h}) \sim \sqrt{3}\,\sigma_{\rm los} \approx 4.3\,\mathrm{km\,s^{-1}}$ expected from simple mass estimators (see; e.g., Wolf et al., 2010). A discrepancy this large is not expected with or without a core, and suggests that the reported properties of the stellar component are likely affected by either limited numerical resolution or substantial departures from equilibrium. Limited numerical resolution is certainly a possibility: a circular velocity of $1\,\mathrm{km\,s^{-1}}$ implies a total mass of $\sim 2.8 \times 10^5\,\mathrm{M_\odot}$ within $r_{\rm h}$, which corresponds to fewer than ~ 200 dark matter particles.

Another possibility is that the estimated values of $\sigma_{\rm los}$ or $r_{\rm h}$ have been inflated by the inclusion of escaping or un-relaxed, weakly-bound particles. If this were the case, then satellite II could not be compared with Crater II, whose inner regions are likely in dynamical equilibrium (see our earlier discussion). Unfortunately, there are not enough details in Frings et al. (2017) to fully track down the origin of the discrepancy with our results, but we stand by our conclusion that Crater II's properties are inconsistent with those of a stellar component inhabiting the equilibrium tidal remnant of a cuspy NFW halo.

Limited resolution also helps to explain the findings of Applebaum et al. (2021), who report a number of simulated satellites with stellar mass ($\sim 10^5\,\mathrm{M_\odot}$), velocity dispersion ($\sim 3\,\mathrm{km\,s^{-1}}$), and size ($\sim 1\,\mathrm{kpc}$) comparable to Crater II, again apparently at odds with our findings. Cores cannot be invoked as an explanation here, since, according to these

[13] We note that "matching the half-light radius" is no guarantee that the actual density profile will be matched. Including weakly bound particles would result in large estimates of $r_{\rm h}$ but it would still fail to fit the density profile, unless the core radius is matched too. See discussion in Sec. 3.3.1.

authors, cored halo profiles are only produced in their simulations in systems with $M_\star > 10^7\,M_\odot$.

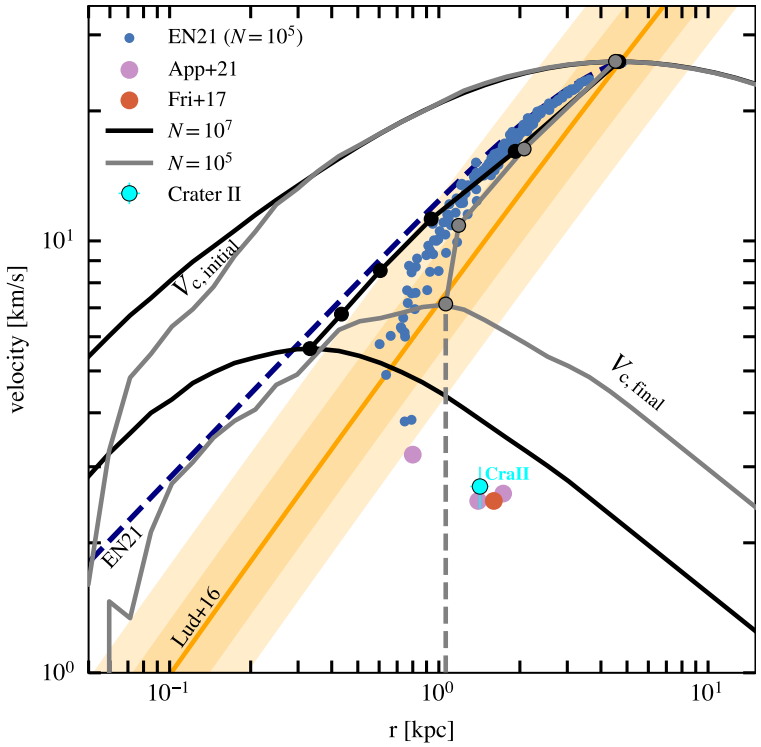

Figure 3.6: A comparison of tidal tracks of 10^5- and 10^7-particle realizations of the same NFW halo (solid grey and black curves, respectively). Circles along each track mark subsequent apocentric passages on orbit 2. Also shown are the quoted values of $r_{1/2}$ and σ_{los} from Applebaum et al. (2021) (purple) and Frings et al. (2017) (orange) for Crater II-like candidates, as well as those for Crater II (Caldwell et al. (2017); cyan symbol with error bar). Note that unlike the 10^7-particle halo, the 10^5-particle halo deviates from the EN21 tidal track and disrupts fully before its fourth apocentric passage. This deviation implies that lower resolution favours spuriously large values of r_{max} of order ~ 1 kpc, similar to those of the simulated Crater II-like candidates. This is confirmed by the results of Errani and Navarro (2021) for 10^5-particle halos (see their Fig. A1), shown by the blue circles. See text for further details.

A more likely explanation is that the large sizes reported for Crater II-like satellites by these authors result because the progenitor halos of Crater II-like systems are resolved with only $\sim 10^5$ dark matter particles, nearly 100 times fewer than in our runs. Indeed, limited resolution yields "tidal tracks" that deviate systematically from the "EN21" track shown in Fig. 3.4, resulting in artificially large values of r_{max} in the case of heavy mass loss.

We show this in Fig. 3.6, where we plot in grey the tidal track of a 10^5-particle NFW

halo otherwise identical to that used in our runs, placed on orbit 2. Solid black curves, as in Fig. 3.4, indicate the evolution of the 10^7-particle halo. Circles along each track indicate the values of r_{max} and V_{max} at subsequent orbital apocentres. The 10^5-particle halo follows a track that deviates from the EN21 track after the second pericentric passage, approaching a nearly constant value of $r_{max} \approx 1$ kpc before (spuriously) fully disrupting before the fourth apocentre. Such deviation is well understood as a result of insufficient resolution. Indeed, the blue circles in Fig. 3.6 show the result of the evolution of many 10^5-particle NFW halos undergoing tidal stripping, taken from Fig. A1 of Errani and Navarro (2021). These systems systematically deviate from the "EN21" track to yield overestimated values of r_{max}.

If, as discussed earlier, the size of "tidally limited" galaxies is dictated by r_{max}, then this would imply a typical size of about ~ 1 kpc for the remnants of $\sim 2 \times 10^9\,M_\odot$ halos such as those studied by Applebaum et al. (2021). The coincidence between this radius and the reported sizes of their Crater II-like candidates supports our view that the large reported sizes of those systems are unduly affected by limited numerical resolution.

Do our results then imply that Crater II's halo had a core? One problem with this interpretation is that core formation in LCDM halos usually results from vigorous inflows and outflows of gas during galaxy formation (Navarro et al., 1996a; Pontzen and Governato, 2012; Peñarrubia et al., 2012; Benítez-Llambay et al., 2019), which are expected to occur only in galaxies more luminous than Crater II (Di Cintio et al., 2014). The model of Peñarrubia et al. (2012) suggests that, for the initial stellar and virial mass of Crater II adopted in the present study study, supernova feedback can produce only a very small core in the dark matter distribution of order $\sim 0.05\, r_{max}$.

Indeed, according to Tollet et al. (2016) sizeable cores are only expected in galaxies whose stellar mass-to-virial mass ratio exceeds a minimum value of $\sim 3 \times 10^{-4}$. This corresponds to a minimum stellar mass of $\sim 10^6\,M_\odot$ for the progenitor halo considered here, roughly an order of magnitude higher than the stellar mass estimated for Crater II. This interpretation thus requires that the stellar component of Crater II was once much more massive than today, which seems unlikely given its low metallicity ($[Fe/H] = -2.10 \pm 0.08$, see; e.g., Fig.8 in Ji et al., 2021).

Finally, Fattahi et al. (2018) used the Errani et al. (2015) tidal tracks to infer the properties of potential progenitors of Crater II, and concluded that Fornax-like systems stripped of more than 99% of its stars could explain the unusual properties of Crater II. Those tracks, however, are applicable only for highly segregated stellar tracers and are not valid for systems as large and diffuse as Crater II. We present a detailed and updated discussion

of such tracks in a separate contribution (Errani et al., 2022), which concludes, as we do here, that the large size of the Crater II dSph is inconsistent with that expected for an equilibrium tidal remnant of such a massive NFW halo.

3.4.4 Comparison with other dwarfs

The structural properties of Crater II are unusual, but not unique. We compare them to other dwarf galaxies in the Local Group in Fig. 3.7, where we plot the deprojected (3D) half-light radii, $r_{1/2}$, and circular velocities at that radius, $V_{1/2}$, for Milky Way satellites (blue symbols), Andromeda satellites (cyan), as well as field dwarfs (brown). These were estimated from the observed projected half-light radius and line-of-sight velocity dispersion using the Wolf et al. (2010) mass estimator: $r_{1/2} = (4/3)R_{1/2}$ and $V_{1/2} \approx \sqrt{3}\sigma_{\rm los}$. Data for Local Group galaxies comes from the compilation of McConnachie (2012)(version January 2021), with the addition of more recent data for some dwarfs, namely Tucana, Antlia 2, Crater II, And XIX, and And XXI (Collins et al., 2020; Taibi et al., 2020; Collins et al., 2021; Ji et al., 2021).

Dark matter-dominated dwarfs inhabiting unstripped, cuspy LCDM halos with $V_{\rm max}$ in the range $(20, 40)\,{\rm km\,s^{-1}}$ (as expected for all dwarfs with $M_\star < 10^7\,{\rm M}_\odot$, regardless how faint) should lie roughly in the area highlighted in grey in Fig. 3.7 (Fattahi et al., 2018). Remarkably, the majority of Local Group dwarfs ($\sim 70\%$) have error bars overlapping that region, which suggests that many of these galaxies indeed follow the simple expectations from LCDM simulations, with little evidence for tidal stripping playing a major role in their structure.

Systems above the grey area would suggest halos more massive than $V_{\rm max} = 40\,{\rm km\,s^{-1}}$, but there are no dwarfs there, except for Bootes II, which has a remarkably high reported velocity dispersion for its size and luminosity (Koch et al., 2009). This has likely resulted from the inclusion of binary stars, which artificially inflated the estimate. Indeed, the analysis of Ji et al. (2016) concludes that Bootes II does not have a well constrained velocity dispersion, and that earlier estimates are best regarded as upper limits.

Systems well below the grey area could in principle reflect halos less massive than $V_{\rm max} = 20\,{\rm km\,s^{-1}}$ (marked by the bottom boundary of the grey region), but this interpretation is disfavoured because such systems would be below the minimum halo mass required for hydrogen to cool efficiently (Efstathiou, 1992; Gnedin, 2000; Okamoto and Frenk, 2009; Benitez-Llambay and Frenk, 2020). The most likely interpretation of such systems (all of which are MW or M31 satellites) is that their dark matter content has been

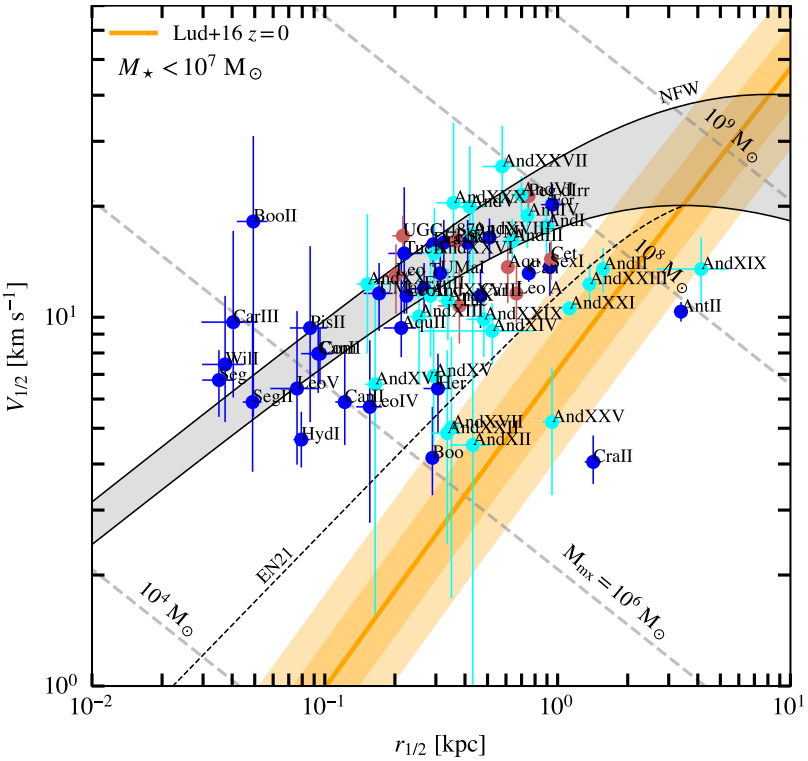

Figure 3.7: Satellites of the Milky Way (dark blue) and of Andromeda (cyan), as well as Local Group field dwarfs (red) with $M_\star < 10^7\,M_\odot$ (Fornax has also been added to the plot, for reference, although its stellar mass is slightly over the limit). 3D half-light radii, $r_{1/2}$, and circular velocities at that radius, $V_{1/2}$, are obtained using the mass estimator of Wolf et al. (2010) applied to the projected half-light radii and line-of-sight velocity dispersions of McConnachie (2012)(version January 2021), updated with recent velocity dispersions for Antlia II, Crater II (Ji et al., 2021), Tucana (Taibi et al., 2020), And XIX (Collins et al., 2020), and And XXI (Collins et al., 2021). Systems with $M_\star < 10^7\,M_\odot$ are expected to populate a narrow range of halo masses (Fattahi et al., 2018), shown schematically here by the grey band bracketing to NFW halos with $V_{\rm max} = 20$ and $40\,{\rm km\,s^{-1}}$ and average concentrations, taken from Ludlow et al. (2016, see orange line with 1σ and 2σ scatter bands). Field dwarfs and satellites unaffected by tides should fall within the grey band. Tidally affected systems can drift below the grey band, but, as discussed in our work here, should stay to the left of the tidal track (labelled "EN21") corresponding to that of the $V_{\rm max} = 20\,{\rm km\,s^{-1}}$ halo, the minimum mass of a halo likely to harbour a luminous dwarf (see; e.g., Benitez-Llambay and Frenk, 2020, and references therein).

reduced by tides. Our discussion above, however, indicates that tidal effects cannot push systems in NFW-like halos much below the dashed line labelled "EN21", which traces the "tidal track" of a $V_{\rm max} = 20\,{\rm km\,s^{-1}}$ halo of average concentration.

The boundary delineated by this tidal track is a bit fuzzy because of the scatter in

concentration around the mean value expected for LCDM (shown by the orange "error bands" in Fig. 3.7), but it is clear that there exist a number of systems whose properties seem at odds with being tidal remnants of NFW-like halos more massive than $V_{\rm max} \sim 20\,{\rm km\,s^{-1}}$. Besides Crater II and Antlia II, for example, the M31 satellites And XXV and And XIX also have unusual sizes and velocity dispersions that are inconsistent with being tidal remnants of massive, cuspy LCDM halos.

The interpretation of these outliers is not completely clear, but, if they are truly dark matter-dominated equilibrium systems, reconciling their properties with LCDM requires unpalatable choices. Going through all possible options in detail is beyond the scope of this contribution, but we note that the simplest option would be to just assume that these dSphs, despite their low stellar mass, had their dark matter cusp softened or removed by baryon effects. This could allow them to reach large sizes and low velocity dispersions, thus evading the boundary set by the "EN21" tidal track shown in Fig. 3.7.

This solution, however, would raise the question of why many other dwarfs show no obvious sign of such core and lie comfortably within the grey region expected for dwarfs in LCDM. What singles out some of these dwarfs, in particular, to develop such cores? There are other alternatives, such as appealing to dark matter self-interactions to explain the presence of a "core" rather than a "cusp", but they all face a similar question: why do only a few dwarfs (and not all, or even most) seem to require a "core" to explain their low dark matter densities?

In this sense, the wide spread in dark matter content between dSphs shown in Fig. 3.7 evokes the puzzle presented by the "diversity" in rotation curve shapes of dwarf irregular galaxies (dIrrs), rotationally dominated galaxies a couple of decades more luminous than the dSphs we consider here (Oman et al., 2015).

This diversity has not yet been fully explained, although it has elicited a number of proposed solutions, from baryon-induced modifications to the dark matter density profile (Navarro et al., 1996a; Pontzen and Governato, 2012; Di Cintio et al., 2014), to modifications to the nature of cold dark matter, such as the inclusion of self-interactions (Rocha et al., 2013; Ren et al., 2019), to alterations of the laws of gravity, such as MOND (McGaugh, 2016; Lelli et al., 2017), to, finally, the possibility that the data has been over-interpreted, and that the diversity is driven by underestimated uncertainties in the derivation of dIrr rotation curves (Oman et al., 2019). None of these proposed alternatives seems clearly favoured at present, as discussed by Santos-Santos et al. (2020b).

3.5 Summary and conclusions

We have used *N*-body simulations to study the effect of Galactic tides on the evolution of the Crater II dSph. The main aim of this work is to probe whether tidal effects may reconcile the unusual size and kinematics of Crater II with that expected from LCDM cosmological hydrodynamical simulations. Our model assumes (i) that Crater II formed as a dark matter-dominated stellar system initially embedded in a cuspy NFW halo; (ii) that Crater II's halo has initially a maximum circular velocity of $\sim 26\,\mathrm{km\,s^{-1}}$ and average concentration, as expected from recent LCDM cosmological hydrodynamical simulations of the Local Group; and (iii) that Crater II stars may be modelled as spherical system with no net rotation. Our main conclusions may be summarized as follows:

(i) The half-light radius of Crater II is poorly constrained due to the uncertain shape of the outer density profile. We therefore use the core radius when comparing simulation results against observations, which is less affected by assumptions about the outer profile shape.

(ii) The pericentric distance of Crater II on its orbit around the Milky Way is not well constrained. We use the latest available data on the sky position, distance, radial velocity, and proper motions of Crater II, together with a Galactic potential model that matches the observed circular velocity at the solar radius, to find that the allowed pericentric distance lies roughly between ~ 10 and $\sim 50\,\mathrm{kpc}$.

(iii) The negative Galactocentric radial velocity of Crater II, together with its large distance, imply that Crater II is just past its latest apocentric passage. More importantly, this also implies that the latest pericentric passage occurred roughly ~ 1 Gyr ago. This implies that the inner ~ 1 kpc of Crater II should be close to dynamical equilibrium, excluding models where its unusual properties are ascribed to substantial departures from equilibrium.

(iv) Assuming that Crater II initially formed in an NFW halo with virial mass $M_{200} = 2.7 \times 10^9\,\mathrm{M_\odot}$ (or $V_{\mathrm{max}} \approx 26\,\mathrm{km\,s^{-1}}$, as suggested by results of the APOSTLE suite of LCDM Local Group simulations), we find that Galactic tides are able to reduce, in a Hubble time, the characteristic velocity of the remnant to $\sim 6\,\mathrm{km\,s^{-1}}$ (as required to match Crater II's low σ_{los}) if placed on an orbit with $r_{\mathrm{peri}} \lesssim 15\,\mathrm{kpc}$.

(v) The stellar components of the halo remnants tidally stripped as described above have core radii of order $\sim 200\,\mathrm{pc}$ – almost a factor of 4 times smaller than observed.

This is a general result for stellar components of NFW halo remnants, regardless of their initial radial extent. Crater II's unusual size and velocity dispersion are thus inconsistent with the tidal evolution of a dwarf galaxy in cuspy NFW halos.

(vi) Crater II's unusual properties are shared by other satellite galaxies in the Local Group, like Antlia II, And XXV and And XXI. None of these galaxies are consistent with a tidal interpretation in the standard LCDM scenario.

Reconciling Crater II-like systems with LCDM requires therefore some additional assumptions, none of them particularly appealing. The least unpalatable is that Crater II's halo had a shallower cusp or inner density core formed during the assembly of the galaxy. It remains to be seen whether this is possible given the low stellar mass of the dwarf. Another possibility is that Crater II's unusual properties arise because the system is quite far from equilibrium. This seems unlikely, given that Crater II is past its latest apocentric passage, and therefore its main body should have relaxed to equilibrium.

A further option is that the estimated photometric parameters of Crater II are somehow in error. This is also unlikely, given that the parameters have been estimated by independent groups (see; e.g., the recent work of Moskowitz and Walker, 2020). Still, both these authors and the original Torrealba et al. (2016) discovery paper report a projected density profile that has an unexpected central *minimum* and a dynamic range of just a factor of ~ 2 in density. These limitations urge further work to rule out the possibility that Crater II's core radius could be perhaps substantially smaller than reported so far.

Should none of these possibilities pan out, one would be forced to consider other alternatives, such as a halo of much lower mass and concentration than assumed in our work, or even the possibility that Crater II's unusual properties signal the need to consider modifying one or more of the foundational assumptions of the LCDM paradigm.

Acknowledgements

RE acknowledges support provided by a CITA National Fellowship and by funding from the European Research Council (ERC) under the European Unions Horizon 2020 research and innovation programme (grant agreement No. 834148). AF is supported by a UKRI Future Leaders Fellowship (grant no MR/T042362/1). This work used the DiRAC@Durham facility managed by the Institute for Computational Cosmology on behalf of the STFC DiRAC HPC Facility (www.dirac.ac.uk). The equipment was funded by BEIS capital funding via STFC capital grants ST/K00042X/1, ST/P002293/1, ST/R002371/1 and

ST/S002502/1, Durham University and STFC operations grant ST/R000832/1. DiRAC is part of the National e-Infrastructure.

Appendix

Orbital Paths

This appendix presents the orbital paths of our Crater II halo on orbits 1, 2, and 3 as described in Sec. 3.3.3.

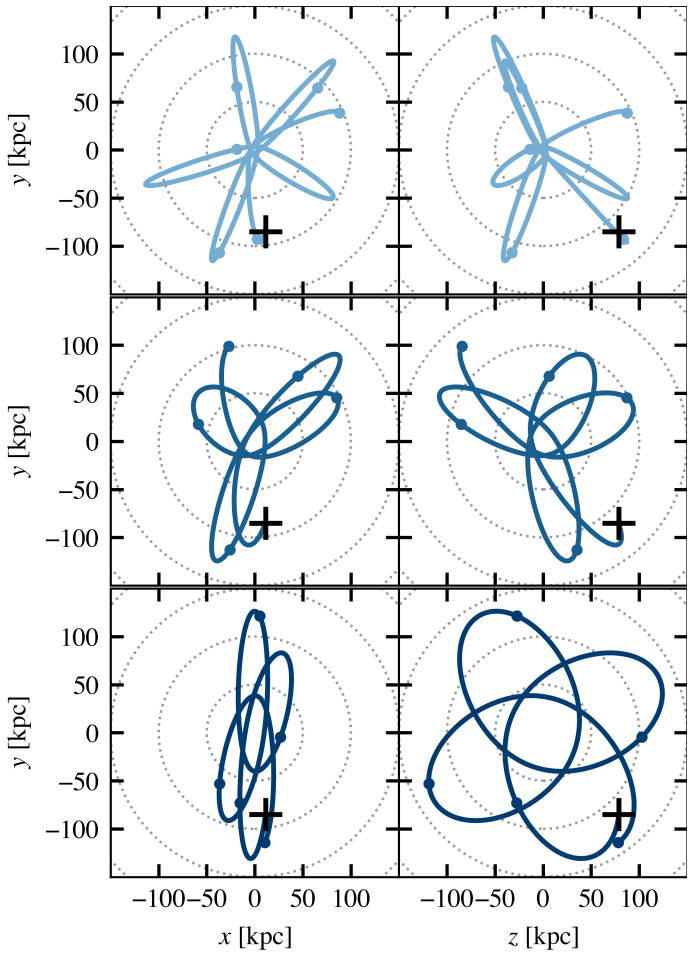

Figure 3.8: Projected trace on the X, Y (left column) and Z, Y (right column) planes of the three orbits considered in this study (see Table 3.1; the top row shows orbit 1, middle row – orbit 2, and bottom row – orbit 3). The current position of Crater II is indicated by a black cross. Intervals of 2 Gyr along the orbit are shown using filled circles. The Sun is at $(-8.3, 0, 0)$ in this coordinate system, with the velocity of the local standard of rest is in the positive Y direction.

Supplementary Tidal Tracks

This appendix presents the supplementary tidal tracks referenced in sections 3.4.2 and 3.4.3.

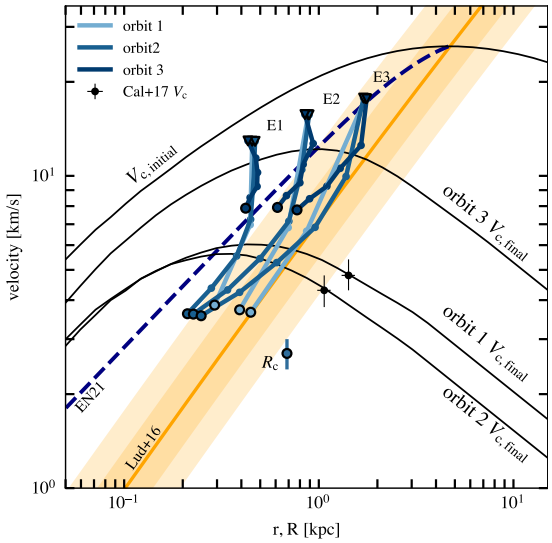

Figure 3.9: Like Fig. 3.4, but with the addition of stellar tracers (E1, E2, and E3 defined in section 3.4.2) tracked through orbits 1 and 3 for comparison.

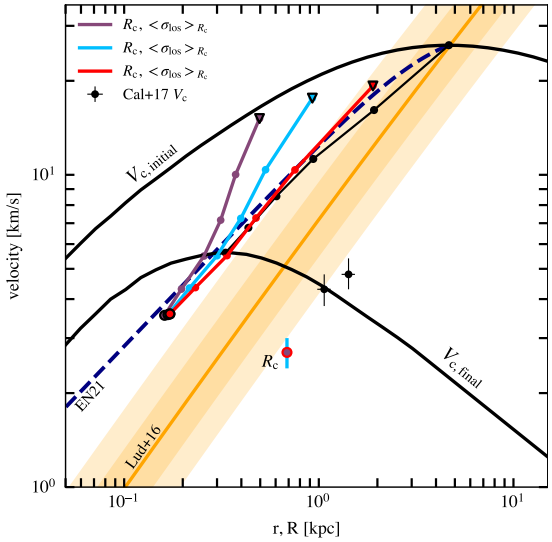

Figure 3.10: Like Fig. 3.4, but for stellar tracers which, at $t = 0$, have Einasto $\alpha = 0.5$ density profiles. The initial stellar core radii R_c are chosen to match those of the exponential tracers in Fig. 3.4. Also here, we observe that, in the limit of large tidal mass losses, the stellar core radii and velocity dispersions evolve in sync with the characteristic size and velocity of the underlying DM halo.

Chapter 4

Galactic tides and a possible explanation for the origin of Antlia II and other "feeble giant" dwarf galaxies

4.1 Abstract

"Feeble giant" galaxies are notable outliers to the relationship between half-light radius and line of sight velocity dispersion that is typically followed by other dwarf galaxies in the Local Group. The peculiar properties of these galaxies pose a problem for ΛCDM, as their low velocity dispersions indicate dark matter halos that are significantly less massive than expected. Such low velocity dispersions may be achieved through tidal stripping, yet reproducing the observed size and surface density profile of these galaxies through the effect of Galactic tides remains a challenge. Focusing on the particular case of the Antlia II dwarf spheroidal galaxy, we use *N*-body simulations to examine the tidal evolution of such galaxies in detail, assuming a Navarro-Frenk-White (NFW) profile for Antlia II's progenitor halo. Our main finding is that while it is indeed difficult to reproduce galaxies such as Antlia II under the assumption of an exponential stellar profile embedded in a cuspy dark matter halo, this tension may be alleviated by imposing a minimum limit on the initial stellar binding energy of the galaxy. Such a limit, which may have been imposed by baryonic effects during the formation of the galaxy, or by the presence of a constant density dark matter core, allows the galaxy to reach a large size while dropping in velocity dispersion as it evolves. Further, we find that the inclusion of some stars which have not yet had time to escape after becoming recently unbound is necessary to reproduce the

observed velocity gradient of Antlia II.

4.2 Introduction

The distant Antlia II dSph satellite of the Milky Way belongs to a population of very faint, and yet simultaneously very large, dwarf galaxies with extremely low velocity dispersions, termed 'feeble giants'. Antlia II was discovered by Torrealba et al. (2019) in data from the second data release of *Gaia* and confirmed with deep archival DECam imaging. Although one of the lowest surface brightness systems observed ($\langle\mu\rangle(r < r_{\rm h}) \sim 31.9\,{\rm mag/arcsec^2}$), Antlia II is similar in spatial extent ($R_{1/2} \sim 2.5\,{\rm kpc}$) to the Large Magellanic Cloud, a galaxy many orders of magnitude brighter.

The peculiar photometric properties of this population of galaxies (which includes, among others, Milky Way satellite Crater II and a couple of satellites of Andromeda: And XXV and And XXI) are compounded by equally unusual kinematics. The velocity dispersion of Antlia II is a mere 6 $\rm km\,s^{-1}$ (compared to roughly 14 $\rm km\,s^{-1}$ expected for dSphs of a similar size), suggesting a surprisingly underdense dark matter halo. Such a low velocity dispersion may arise as a result of severe stripping by Galactic tides, and indeed the case for a tidal formation scenario has been strengthened by the detection of a clear line-of-sight velocity gradient aligned with the orbital path determined from recently released *Gaia* proper motions (Ji et al., 2021).

Torrealba et al. (2019) and Ji et al. (2021) both favour a tidal interpretation, noting however the difficulties in reproducing Antlia II in the context of a cuspy dark matter halo, as predicted by the standard model of cosmology, ΛCDM. Similar difficulties were discussed in Borukhovetskaya et al. (2022b) for the analogous case of the Crater II dSph, where we find that in the late stages of tidal stripping, the size of bound stellar remnants cannot exceed the characteristic radius of the underlying dark matter halo as there is little bound mass left outside this radius. Matching simultaneously the low velocity dispersion and large projected density profile is therefore a challenge, at least for initially exponential stellar models embedded in a cuspy dark matter halo.

In addition, there remains still a lack of consensus on the amount of stellar mass loss experienced by Antlia II. Torrealba et al. (2019) and Sameie et al. (2020) estimate that the satellite has lost $\sim 99\%$ and $\sim 90\%$ of its stellar mass due to tides, respectively; however, the updated mean metallicity of Ji et al. (2021) places Antlia II firmly on the luminosity-metallicity relation (Kirby et al., 2013), leading the authors to disfavour such high degrees of mass loss at about 3σ. In contrast to previous studies, Ji et al. (2021) predict that the

galaxy is in the early stages of being stripped, and it is unlikely that it has lost more than roughly half its mass in stars.

Using detailed N-body simulations of the tidal evolution of subhalos around the Milky Way, we examine whether it is possible to account for the apparent low stellar mass loss as well as the observed structure and kinematics of Antlia II, assuming it inhabits a cuspy cold dark matter halo. Ultimately, our study suggests a possible mechanism that may explain the peculiar properties of galaxies such as Antlia II and Crater II as tidal remnants of LCDM halos.

This work is organised as follows. We begin by summarising observed properties of Antlia II and our numerical setup in section 4.3. Section 4.4 presents the results of our simulations, where section 4.4.1 outlines the difficulties of reproducing Antlia II with conventional stellar models in a cuspy dark matter halo, and sections 4.4.2 and 4.4.3 discuss alternative formation paths. We end with a brief summary and discussion of our results in section 4.5.

4.3 Observations and Simulations

This section summarises briefly the observed properties of Antlia II, and outlines the numerical setup of the N-body simulations used to model the tidal evolution of Antlia II in the gravitational potential of the Milky Way.

4.3.1 Observed properties of Antlia II

The physical properties of Antlia II were first estimated from *Gaia* DR2 by Torrealba et al. (2019), who quote the projected half-light radius to be $R_{1/2} \sim 2.92\,\mathrm{kpc}$, modelling the stellar spatial distribution as a mixture of a planar foreground and a Plummer profile. Incorporating the updated *Gaia* EDR3 proper motions, Ji et al. (2021) find a slightly smaller half-light radius, $R_{1/2} \sim 2.54\,\mathrm{kpc}$, likewise fitting Antlia II with a Plummer profile. In addition, Ji et al. (2021) detect a clear velocity gradient roughly aligned with the galaxy's major axis and proper motion. Such a velocity gradient could in principle arise from the presence of rotation, however Ji et al. (2021) emphasise its alignment with the orbital direction of Antlia II as favouring a tidal interpretation for the dSph. In this scenario, we now observe the galaxy right as it is being tidally disrupted but before it has lost most of its stars.

Table 4.1: Current observational constraints, as well as parameters of the three orbits explored using N-body simulations in this study. Orbits 1 and 2 are the orbits corresponding to the 16th and 84th percentile of the distribution in pericentres obtained with the proper motions of Torrealba et al. (2019). Orbits 3 and 4 are the same, obtained with the proper motions of McConnachie and Venn (2020). Pericentres and apocentres are computed for the Milky Way potential model discussed in section 4.3.2.

observation	α (deg)	δ (deg)	distance (kpc)	μ_{α^*} (mas yr^{-1})	μ_δ (mas yr^{-1})	v_r (km s^{-1})
	143.8868	−36.7673	132 ± 6 [1]	-0.095 ± 0.018 [1]	0.058 ± 0.024 [1]	290.7 ± 0.5 [1]
				-0.09 ± 0.01 [2]	0.12 ± 0.01 [2]	
				-0.094 ± 0.007 [3]	0.103 ± 0.008 [3]	

[1] Torrealba et al. (2019), [2] McConnachie and Venn (2020), [3] Ji et al. (2021)

model parameters	pericentre (kpc)	apocentre (kpc)	distance (kpc)	μ_{α^*} (mas yr^{-1})	μ_δ (mas yr^{-1})	v_r (km s^{-1})
orbit 1	32.8	140	132	-0.095	0.058	290.7
orbit 2	44.1	147	138	-0.077	0.082	291.2
orbit 3	57.9	143	132	-0.090	0.120	290.7
orbit 4	69.2	151	138	-0.080	0.130	291.2

4.3.2 Milky Way potential model

The Milky Way is modelled as an analytical, static potential, consisting of an axisymmetric two-component Miyamoto and Nagai (1975) disk, a Hernquist (1990) bulge and an NFW dark matter halo. These models and their parameters are as summarised in section 1.4.2.

4.3.3 Orbits

The orbit of Antlia II in the assumed Milky Way potential may be estimated from its present-day Galactocentric position and velocity, as inferred from its sky position, radial velocity, distance, and proper motion, assuming that the effects of dynamical friction can be neglected. Of the observed parameters, summarised in table 4.1, the proper motions contribute the majority of the uncertainty budget in determining the orbit.

As in the case of Crater II, detailed in Chapter 3, the uncertainties in the observed proper motions result in a fairly broad distribution of possible pericentric and apocentric distances, shown by the histograms in Fig. 4.1. Different estimates for the proper motion will, of course, yield different orbits. We show in figure 4.1 the pericentric and apocentric distributions corresponding to proper motion estimates from Torrealba et al. (2019), Ji

et al. (2021), and McConnachie and Venn (2020)[1], illustrating that a wide range of orbits ($20\,\mathrm{kpc} \lesssim r_{\mathrm{peri}} \lesssim 70\,\mathrm{kpc}$) are permissible given the various estimates of the proper motion quoted in the literature.

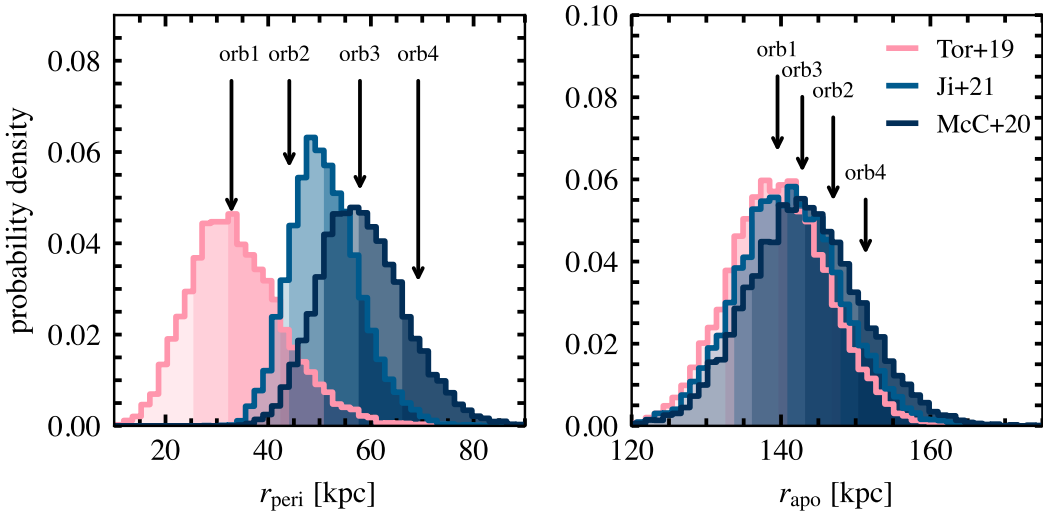

Figure 4.1: The probability distributions of Antlia II pericentric (left panel) and apocentric (right panel) distances obtained from varying the proper motions, distance, and radial velocity according to their respective reported uncertainties. Each colour corresponds to different proper motion estimates, from Torrealba et al. (2019, pink), Ji et al. (2021, blue), and McConnachie and Venn (2020, black), as listed in table 4.1. The three orbits selected to explore the available parameter space are shown with arrows pointing down. Regions beneath the histograms darken at the 16th, 50th, and 84th percentile..

4.3.4 Antlia II model

4.3.4.1 Dark matter component

The Antlia II dark matter halo is modelled as an equilibrium N-body realisation of the NFW density profile,

$$\rho_{\mathrm{NFW}}(r) = \frac{\rho_{\mathrm{s}}}{(r/r_{\mathrm{s}})(1+r/r_{\mathrm{s}})^2}. \tag{4.1}$$

This profile is fully specified by two parameters; e.g., a scale density, ρ_{s}, and scale radius, r_{s}, or, alternatively, by a maximum circular velocity, V_{max}, and the radius at which it is reached, r_{max}.

[1]Note that Torrealba et al. (2019) proper motions are found using *Gaia* DR2, while Ji et al. (2021) and McConnachie and Venn (2020) use the updated *Gaia* EDR3.

Among other cosmological hydrodynamical simulations, the APOSTLE suite, which simulates the dynamics of galaxies in the Local Group, has demonstrated a strong correlation between $V_{\rm max}$ and the stellar mass of galaxies, $M_\star$. We adopt a stellar mass for Antlia II of $8.8 \times 10^5\,{\rm M}_\odot$ (Torrealba et al., 2019) and estimate $V_{\rm max}$ (before tidal effects) using the empirical fit[2] to the $M_\star$-$V_{\rm max}$ correlation in APOSTLE from Fattahi et al. (2018). The characteristic radius $r_{\rm max}$ then follows from the Ludlow et al. (2016) parametrisations of the ΛCDM halo mass-concentration relation at redshift $z = 0$. The resulting NFW profile has $V_{\rm max} = 28.4\,{\rm km\,s^{-1}}$ and $r_{\rm max} = 5.24\,{\rm kpc}$, or in terms of virial mass and concentration, $M_{200} = 3.60 \times 10^9\,{\rm M}_\odot$ and $c = 13.3$.

In section 4.4.3, the NFW dark matter profile is amended to include a constant density central core; in this case, instead of a divergent density cusp with slope −1, we have $\mathrm{d}\log\rho/\mathrm{d}\log r \to 0$ for $r \to 0$. In practice, we adopt the parametrisation of Peñarrubia et al. (2012), which adds a core size parameter, $r_{\rm c}$, to the original NFW equation:

$$\rho_{\rm c}(r) = \frac{\rho_{\rm s}}{(r_{\rm c}/r_{\rm s} + r/r_{\rm s})(1 + r/r_{\rm s})^2}. \tag{4.2}$$

In section 4.4.3, we implement a halo with core size $r_{\rm c} = r_{\rm s}/3 = 0.6\,{\rm kpc}$.

4.3.4.2 Stellar component

We model the stellar component of Antlia II using the method described in section 1.4.3. We assume that it only negligibly contributes to the total gravitational potential of the dwarf, and, more specifically, stellar components are modelled as Einasto profiles (Einasto, 1965),

$$\rho_{\rm E}(r) = \rho_{\rm E0} \exp[-(r/r_{\rm E})^\alpha], \tag{4.3}$$

with $\alpha = 1$ (i.e. exponential spheres) and two different initial half light radii, $R_{1/2} = 1.5$ and 3.0 kpc. In practice, stars are modelled[3] by attaching a stellar probability to each dark matter particle, following the appropriate distribution function (see; e.g., Bullock and Johnston, 2005). With this method, the probability of each N-body particle to represent a star is proportional to the ratio of the dark matter and stellar energy distributions:

$$\mathscr{P}_\star(E) \propto (\mathrm{d}N/\mathrm{d}E)_\star / (\mathrm{d}N/\mathrm{d}E)_{\rm DM}. \tag{4.4}$$

[2] $M_\star = M_0 v^\alpha \exp(-v^\gamma)$, where $v = V_{\rm max}/50\,{\rm km\,s^{-1}}$, and $(M_0, \alpha, \gamma) = (3.0 \times 10^8\,M_\odot, 3.36, -2.4)$.

[3] For details see the publicly available implementation of Errani and Peñarrubia (2020): https://github.com/rerrani/nbopy

The underlying energy distributions are computed numerically as outlined in Errani and Peñarrubia (2020), allowing the probabilities to be computed at infall and tracked along the orbit. At any point the stellar structure and kinematics may be recovered from the dark matter distribution by applying the individual stellar probabilities as weights.

4.3.5 Simulation code

10^7-particle N-body realisations of NFW halos are computed using the ZENO[4] software package developed by Joshua Barnes at the University of Hawaii. ZENO uses Monte Carlo sampling of a given distribution function to generate systems in virial equilibrium.

A 10^7-particle N-body realization of a centrally cored halos with isotropic velocity dispersion is generated following the approach of Errani and Peñarrubia (2020): by (i) computing the corresponding distribution function through Eddington inversion and by (ii) sampling from this distribution function.

We allow halos to fully relax prior to introducing them into the Milky Way potential, by running them first in isolation for 5 Gyr using the publicly available GADGET-2 simulation code (Springel, 2005). After the halos have fully relaxed, they are evolved on the orbits described in section 4.3.3 and in the potential detailed in section 4.3.2 for ~ 10 Gyr. Forces between particles are smoothed with a Plummer-equivalent softening length of $\epsilon_{\rm P} = 8$ pc and we consider our results converged outside $r_{\rm conv} = 93$ pc.

4.4 Results

Having introduced our numerical setup, we turn next to the tidal evolution of Antlia II. In section 4.4.1, we examine first the evolution of an Antlia II model that assumes an exponential stellar density profile embeddded in a cuspy NFW halo, a scenario similar to that considered for Crater II in Borukhovetskaya et al. (2022b). Having identified the challenges this scenario faces to reproduce the observed properties of Antlia II, we next present possible means of alleviating this tension in section 4.4.2.

[4] http://www.ifa.hawaii.edu/faculty/barnes/zeno/

4.4.1 Evolution of a cuspy, exponential Antlia II

4.4.1.1 Tidal effects on the dark matter component

The evolution of the circular velocity within $r_{1/2} = 4/3R_{1/2} = 3.4\,\mathrm{kpc}$ of our Antlia II NFW halo models is shown in Fig. 4.2. Different colors correspond to different orbits. A horizontal black line indicates, for reference, the circular velocity at the same radius estimated by Ji et al. (2021) using the mass estimator of Wolf et al. (2010), and diamonds indicate the snapshots (at $t = t_{\mathrm{fin}}$) we identify for comparison with observational data.

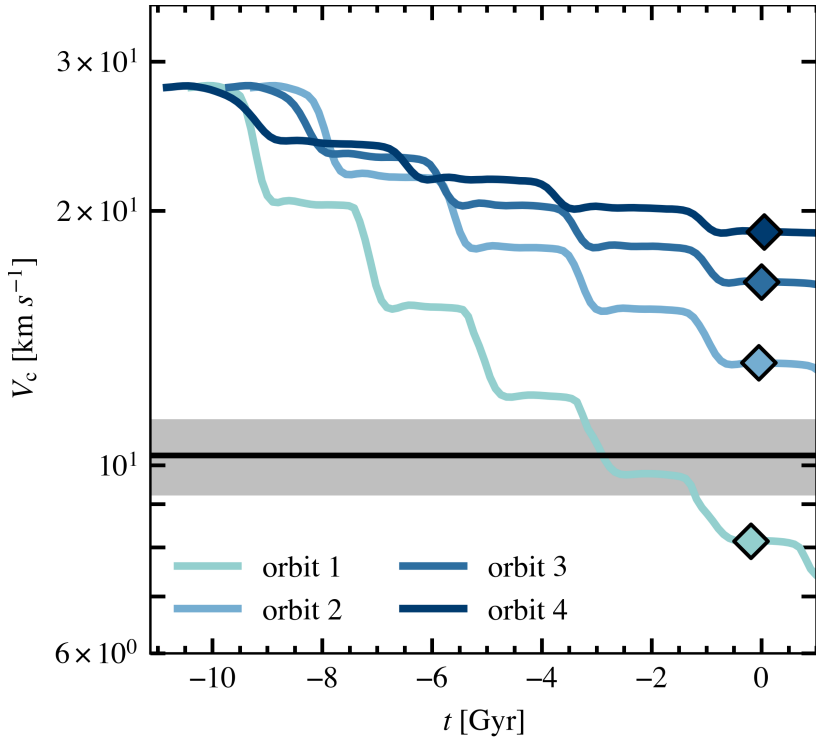

Figure 4.2: Evolution of the circular velocity at the half-light radius of Antlia II (i.e., V_c at $r_{1/2} = 4/3 \times R_{1/2} = 3.4\,\mathrm{kpc}$) for our halo model in each of the three different orbits explored in this work; lighter shades correspond to smaller pericentres. The horizontal black solid line and grey shaded region represent the observational constraint on V_c, as well as the $\pm1\sigma$ uncertainty interval, taken from Ji et al. (2021). Diamonds indicate the snapshot(s) at t_{fin} we identify for comparison with observational data. Note that, only on orbit 1 does our chosen halo get stripped enough to bring the system into agreement with the observed constraint after orbiting for $\sim 10\,\mathrm{Gyr}$.

As tidal forces gradually remove material from the system, the circular velocity experiences a continuous decline, marked by sudden drops at subsequent pericentric passages. The extent of this decrease strongly depends on the chosen pericentric distance. We see

that for a pericentre as large as 40 kpc, the effects of tidal forces alone are not enough to reduce the circular velocity to a level close to the observational estimate.

Orbit 1, however, with a pericentre of 30 kpc, exhibits substantial mass loss that appears sufficient to reconcile the circular velocity of the remnant with the observed estimate in less than 10 Gyr. We note that reducing the initial circular velocity to the observed V_c requires a significant amount of mass loss, with only 1.4% of the initial dark mass remaining bound as V_c approaches the observed estimate of 10 km s^{-1} .

We conclude that the unusually low velocity of Antlia II could in principle be explained if its orbit had a pericentric distance of 30 kpc or smaller. This value is not ruled out according to current observational estimates; however, tighter constraints on allowed pericentres could possibly rule out this scenario if larger pericentres are found to be more favourable.

4.4.1.2 Tidal effects on the stellar component

The stellar component is likewise affected by tidal losses. We focus here in turn on the evolution of two possible exponential stellar models with differing initial half light radii (henceforth models E1 and E2) on orbit 1.

We begin by tracking the evolution of the projected half-light radius, $R_{1/2}$, and line of sight velocity dispersion, σ_{los}, averaged within 2.3 kpc from the centre (approximately 1 deg on the sky at the observed position of Antlia II) in figure 4.3. Only particles still bound to the tidal remnant are included in this calculation and we shall call the corresponding models E1b and E2b. Results for the two stellar models are shown with different coloured tracks, starting with the initial conditions and ending, after 5 pericentric passages, on the upward triangles highlighted in black. Each circle along the two tracks indicates a subsequent apocentric passage. The observed Antlia II half-light radius and velocity dispersion are shown, with errorbars, by the yellow triangle.

We note that similarly to the case of Crater II, as detailed in Borukhovetskaya et al. (2022b), neither of the stellar tracks approaches the observed location of the dSph in the $R_{1/2}$-σ_{los} plane. As mass is gradually lost from the system, the stellar velocity dispersions decrease, but so do their half-light radii. Indeed by the time the velocities begin to approach the observed value, the remnant half-light radius is nearly three times smaller than the observed half-light radius. This outcome applies to both stellar models, irrespective of their initial radii.

As discussed in Borukhovetskaya et al. (2022b) and Errani et al. (2022), after substantial

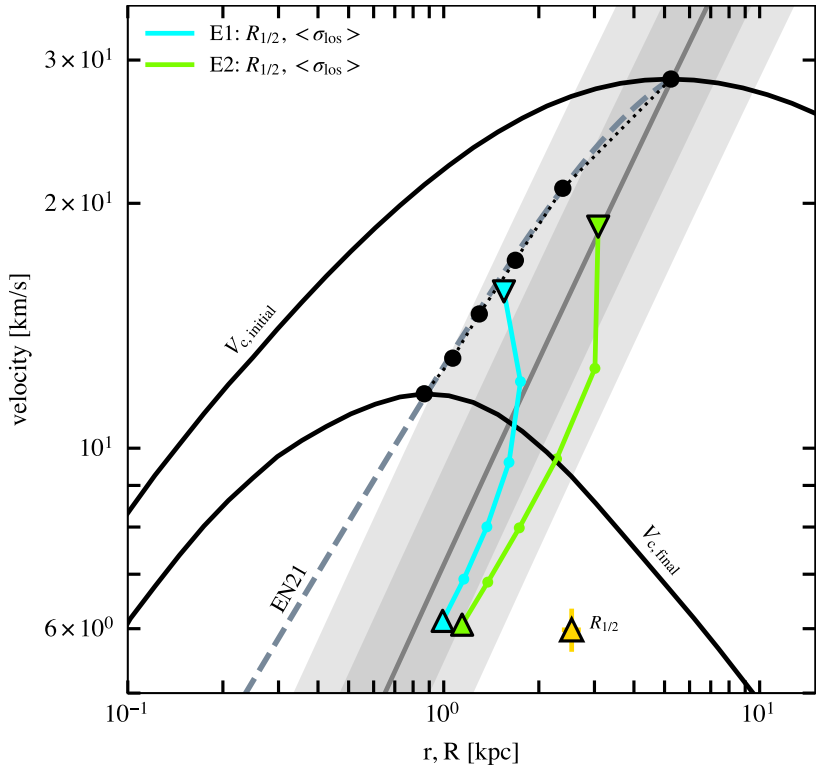

Figure 4.3: Evolution of the projected half light radius, $R_{1/2}$, and line-of-sight velocity dispersion, σ_{los}, for two different exponential stellar component models, using only bound particles, on orbit 1. Downward triangles indicate the initial values, and upward triangles the values at the final snapshot. The coloured lines trace the evolution of these parameters as a function of time; each small circle marks subsequent apocentric passages. The red track corresponds to model E1b, and the blue track to model E2b. The grey line shows the r_{max}-V_{max} relation (plus 1σ and 2σ scatter bands in concentration) expected for ΛCDM halos at $z = 0$ (Ludlow et al., 2016, in grey). The initial and final circular velocity of the assumed Antlia II progenitor halo is shown by the solid black curves. A black circle with error bars shows the observed V_c constraint from Ji et al. (2021). The yellow circle indicates the observed values of $R_{1/2}$ and σ_{los} for Antlia II. The dashed pink curve shows the "tidal track" of Errani and Navarro (2021), which traces quite well the evolution of r_{max} and V_{max} of the halo (shown as a solid black line with circles at each apocentric passage) as a function of time.

mass loss, the size of bound, initially exponential stellar remnants are expected to closely match the characteristic size of their dark matter halo, indicated by the dashed pink line in figure 4.3 (solid black lines in this figure show the halo circular velocity profile at the beginning of the simulation and at the final snapshot considered). This is because r_{max} marks the 'tidal truncation' radius, beyond which little bound mass remains, and is there-

fore an upper limit to the stellar half-light radius of the remnant (see, also, Kravtsov, 2010; Errani et al., 2022).

Thus, in the late stages of tidal stripping, the size of the bound stellar components E1b and E2b cannot exceed $r_{\rm max} = 0.9\,\rm kpc$. As a result, the size of the remnants is too small, and the density profile cannot reproduce the observed surface density profile (solid yellow), as illustrated in the left panel of figure 4.5.

In further conflict with observations, no appreciable velocity gradient, such as discussed in section 4.3.1, is detected when considering only remaining bound particles. The light purple line in the right panel of figure 4.5 shows the velocity gradient of our model E1b measured along the major axis of the Antlia II remnant at the chosen final snapshot. Unlike the observed gradient from Ji et al. (2021), plotted here in grey and black and showing a clear trend of decreasing radial velocity towards the direction of motion, the radial velocities of E1b remain relatively constant along the major axis.

We consider next the possibility that the observed structure of Antlia II may be affected by stars which are, at that snapshot, unbound but have not yet had time to leave the system. Rather than considering only bound particles as members of the Antlia II remnant, we expand then our selection to include all particles in a square that is centred on Antlia II and $10 \times 10\,\rm deg$ on the sky as well as within 20 kpc along the line of sight. To differentiate from the two bound exponential models discussed up to this point, we will call these new models "mixture models" E1m and E2m.

At this stage of the orbit, just prior to apocentre, the two tidal tails extending from Antlia II are oriented nearly perpendicular to the orbital path. Figure 4.4 shows the projection of Antlia II on the orbital plane, with dark matter in grey and our selection of bound and unbound stars (E1m) coloured by their radial velocity. Stars located in the inner regions are close to equilibrium. On the other hand, stars located past the break radius, $R_{\rm b} \approx 2\,\rm kpc$, marked here as a small black circle, are still moving outwards along the tidal tails. Viewing this outward motion from our point of view ($i = 0, j = -8\,\rm kpc$), illustrated by the angle outlined in yellow, gives the appearance of a velocity gradient along the direction of motion. When considering an Antlia II composed only of bound particles, we are essentially limiting our selection to members roughly within the black circle and therefore the velocity gradient is not observed. However, including some unbound particles allows us to sample regions of outward motion and thus better reproduce the observed velocity gradient.

The resulting velocity gradient (dark purple) is shown in the right panel of figure 4.5 along with the corresponding final surface density profiles (solid curves) in the left panel.

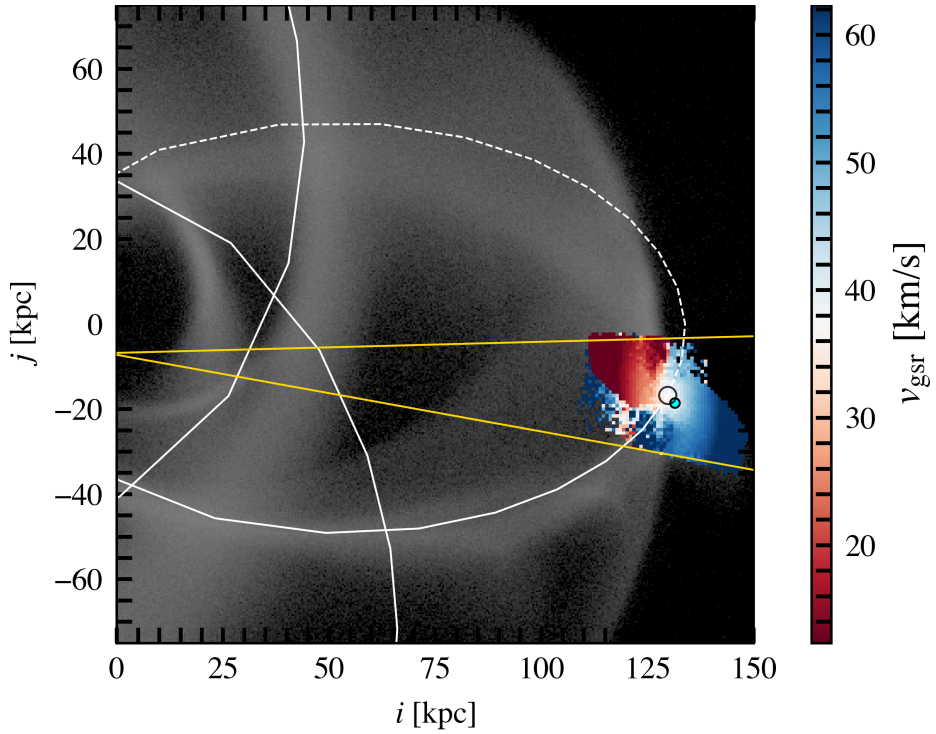

Figure 4.4: Projection of Antlia II onto the plane of its orbit. Dark matter is in grey and stellar selection E1m, consisting of both bound and unbound particles, is coloured by its radial velocity. The past orbital path is shown in solid white and the future orbit in dashed white. Cone of 5 deg radius centred on Antlia II, which is used as a selection criterion for E1m, is illustrated in yellow. The unfilled black circle shows the break radius and the filled cyan circle shows the true observed position of Antlia II (Ji et al., 2021).

Importantly, figure 4.5 shows that although the observed strength of the velocity gradient is better reproduced, the density profiles remain too centrally concentrated to match observations, despite the inclusion of unbound material along the line of sight. Matching simultaneously the projected density profile and velocity gradient is therefore a challenge, at least for initially exponential stellar models embedded in a cuspy dark matter halo. We explore next how such models may be modified to attempt to match the data. One possibility is to consider different initial stellar models (described in section 4.4.2 below). A separate possibility is that the dark matter halo is not cuspy but cored, which may yield larger remnants when tidally disrupted (see, e.g., Sanders et al., 2018). We explore this second possibility in section 4.4.3.

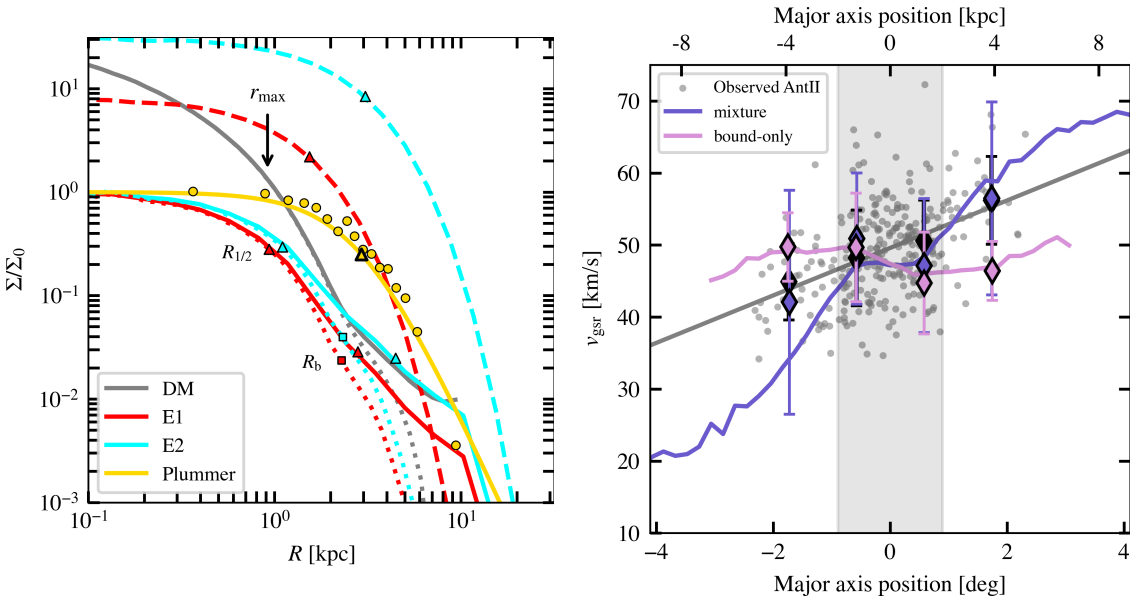

Figure 4.5: *Left:* Surface density profiles of the remnants of mixture exponential stellar component models E1m and E2m, initially (dashed) and at the final snapshot identified for orbit 1 (solid), normalized to match the observed central density, Σ_0. Note that the half light radii are much smaller than observed, despite the initial half light radii ranging from 1.5 kpc to 3 kpc for the E1 and E2 model respectively. The characteristic radius of the remnant halo, r_{max}, shown by an arrow, is a good indicator of the tidal truncation radius of the system. The dark matter halo projected density is drawn for reference in dotted grey. *Right:* At t_{fin}, radial velocities of stellar component models E1b (pink) and E1m (purple) measured along the major axis, plotted against observed radial velocities of Antlia II members from Ji et al. (2021). Diamond errorbars indicate mean values of N-body particles with high probability (as defined in section 4.3.4.2) of representing a star and which on the sky lie near to members of Ji et al. (2021), while the solid lines reflect the entire Antlia II selection. A grey shaded band depicts the region within the break radius. Note that outside the break radius, the observed velocity gradient is reproduced far better when considering a mixture of bound and unbound particles – model E1m.

4.4.2 Alternative evolutions

The structural evolution of a satellite driven by tides is most easily characterised in terms of the initial binding energies of its particles (see, e.g., Choi et al., 2009; Errani et al., 2022). Relative to the potential minimum, Φ_0, binding energies may be expressed as

$$\mathscr{E} = 1 - E/\Phi_0, \tag{4.5}$$

where E is simply $v^2/2 + \Phi(r)$. This definition scales the energies so that the most bound particles, then, lie at $\mathscr{E} = 0$, and the most weakly bound particles lie at the boundary

between bound and unbound, $\mathscr{E} = 1$.

The initial binding energy distribution for a NFW dark matter halo is shown in solid black in the left panel of figure 4.6. As tides act on the system, the least bound particles are the most likely to be stripped away first; thus, the energy distribution is gradually trimmed off from right to left (Errani et al., 2022). The initial binding energies of the group of Antlia II dark matter particles which on orbit 1 will remain bound until the last apocentre is drawn in the left panel of figure 4.6 in dotted grey, and this group comprises only particles with energies more bound (further to the left in figure 4.6) than $\log(\mathscr{E}) \sim -0.4$.

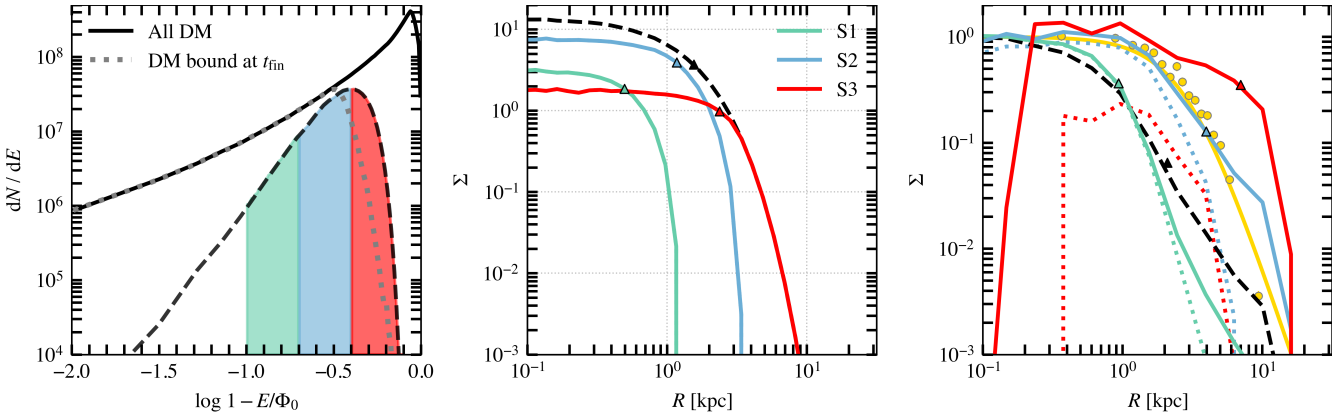

Figure 4.6: *Left:* Initial binding energy distribution of particles: NFW halo in solid black, dark matter which remains bound to the subhalo at the last apocentre in dotted grey, and stellar model E1 in dashed black. Initial energies are measured relative to the initial potential minimum, where for NFW halos $\Phi_0 \approx -4.63\, V_{\rm mx}^2$. Green, blue, and red bands show stellar selections where stars are chosen to occupy only a narrow region of initial binding energies. *Centre:* Initial surface brightness profiles corresponding to the stellar selections chosen in the left hand panel. For reference, the exponential stellar model E1 is shown in dashed black. *Right:* Surface brightness profiles of the three slice models at $t_{\rm fin}$, with solid lines showing the entire stellar component and dotted lines highlighting only the bound subsection of each. For comparison, the observed Antlia II surface brightness profile is shown in yellow. Note, the blue selection reproduces the observed surface brightness profile reasonably well.

Particles which are very strongly bound tend to populate the central cusp of a halo, whereas less bound particles tend to occupy regions further from the centre. When attempting to reproduce a highly extended galaxy such as Antlia II, one possibility is to choose an initial distribution that favours more weakly bound particles, while minimising the number of particles on strongly bound orbits. A simple way of achieving this would be to posit that stars have a well defined *minimum* energy. In the case of figure 4.6,

choosing that minimum to be just below the tidal boundary ($\log(\mathscr{E}) \sim -0.4$) would result in a system which, at the snapshot we are analysing, will have a much lower ratio of bound to unbound stars than the original exponential profile. This could, in principle, result in a larger stellar system, at least temporarily, before the unbound stars leave the system. Because particles with energies much larger than $\log(\mathscr{E}) \sim -0.4$ are stripped from the system before the last apocentre, they would no longer be close enough to the remaining bound remnant to contribute stars to the analysis, and there is no need to impose an upper energy limit on stars. The larger the upper energy boundary, however, the more stars the system would have lost by the time of analysis, implying the need for more massive initial stellar systems to match the luminosity of Antlia II today.

We show this in figure 4.6 by slicing the initial energy distribution of the E1m exponential model (shown with a dashed black line) into three different energy bins, coloured in green, blue and red, in order of decreasing binding energy. The red shaded region (stellar model S3) contains the most weakly bound particles in the initial conditions, while the green region (S1) contains more strongly bound particles, with blue (S2) an intermediate choice. The central panel shows, at infall, the initial density profiles of the three stellar energy slices selected in the left panel, and the right panel shows the corresponding density profiles at $t_{\rm fin}$. The green density profile in the central panel is normalised such that at $t_{\rm fin}$ its central density is 1, and the remaining density profiles use the same normalisation.

As expected, we see that with fewer strongly bound particles in the initial selection of binding energies, the overall size of the remnant increases. Furthermore, the final density profiles are able to approach and even surpass the observed density profile in size. Model S2 (blue slice in figure 4.6), in particular, at final snapshot reproduces reasonably well the observed surface brightness profile of Antlia II. Furthermore, S2 also reproduces reasonably well the observed velocity gradient, as shown in figure 4.7.

This exercise demonstrates that it is possible to reconcile the observed density profile, velocity dispersion, and gradient of Antlia II with the tidal remnant of a cuspy NFW halo, at the expense of choosing carefully the initial energy distribution of the stellar component (model S2, for example).

Does S2 constitute a viable stellar model for Antlia II? We begin by considering how S2 compares with other dSphs regarding its structural parameters. Figure 4.8 shows with blue stars the initial stellar mass, central line-of-sight velocity dispersion, and half-light radius of S2 prior to any tidal effects, compared against field dwarfs and satellites of the Milky Way and Andromeda in grey. From this comparison, at least, it would appear that S2 is a viable progenitor of Antlia II. S2's initial stellar mass is $8 \times 10^6\,\mathrm{M}_\odot$, implying that

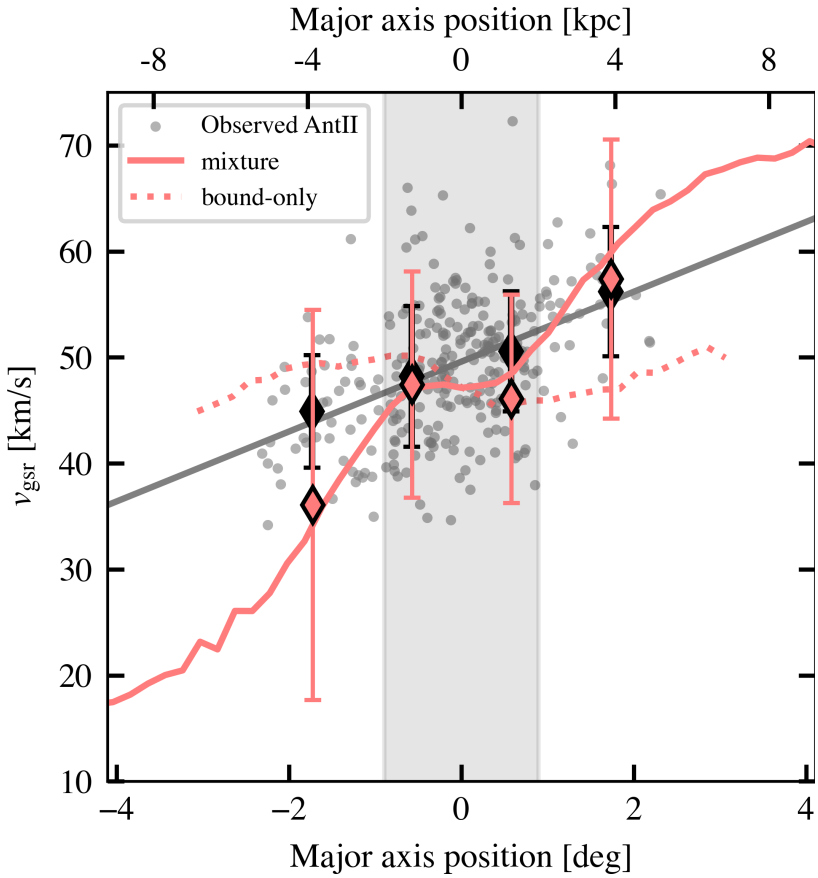

Figure 4.7: At final snapshot, radial velocities of stellar component model S2, depicted in figure 4.6, measured along the major axis and plotted against observed radial velocities of Antlia II members from Ji et al. (2021). Diamond errorbars indicate mean values of high probability stellar particles which on the sky lie near to members of Ji et al. (2021), while the purple line reflects the entire Antlia II selection. In pink is the subsection of S2 that is bound. A grey shaded band depicts the region within the break radius.

Antlia II has already lost nearly 90% of its initial stellar content, though we emphasize that the mass loss can easily be reduced to levels predicted by Ji et al. (2021) by simply lowering the maximum selected binding energy. In terms of luminosity, size ($R_{1/2} \sim 1.2$ kpc), and velocity dispersion (16 $\mathrm{km\,s^{-1}}$), S2 resembles the Peg dwarf irregular, or perhaps the And VII dSph.

Although S2 appears to be a viable progenitor for Antlia II, its density profile and velocity dispersion profiles would be different from those of an exponential model, which has often been used successfully to fit dSphs. We examine this in figure 4.9, where we plot the surface density profile, its logarithmic slope, $\Gamma = \mathrm{d}\log\Sigma/\mathrm{d}\log R$, and the velocity dispersion profile for different maximum and minimum cuts in the initial binding energy of

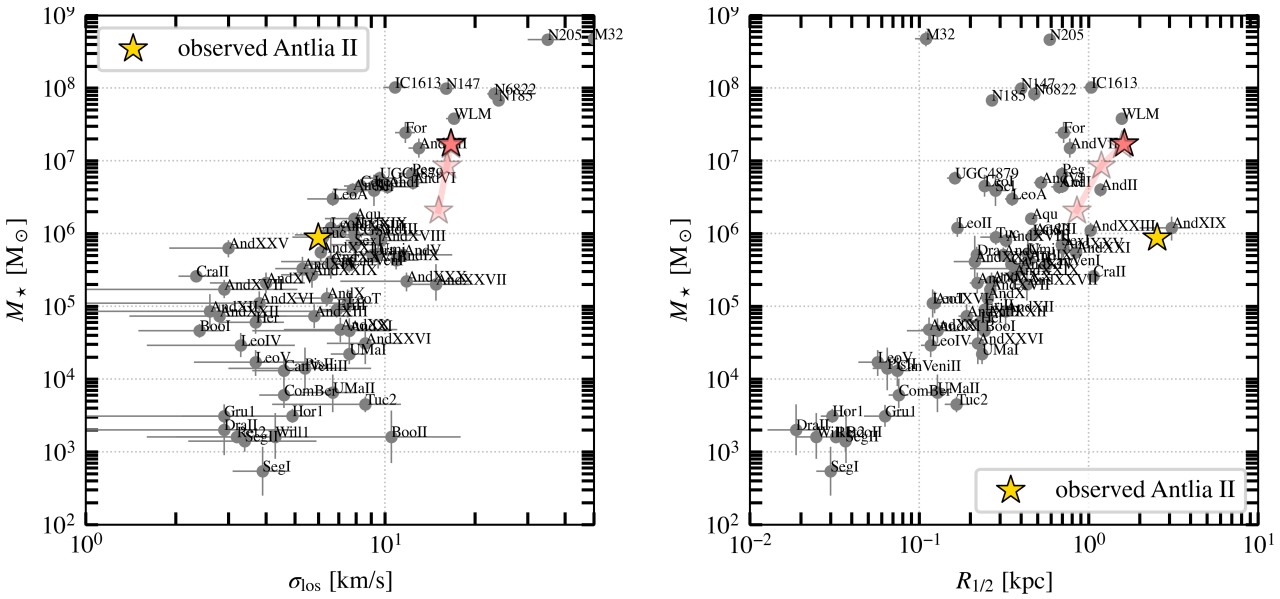

Figure 4.8: Stellar mass, central velocity dispersion, and half light radius of the progenitor of stellar component model S2 shown in figure 4.6 (blue star) and of the observed Antlia II (yellow star). Plotted in grey are isolated field dwarfs, satellites of the Milky Way, and satellites of Andromeda (Fattahi et al., 2018).

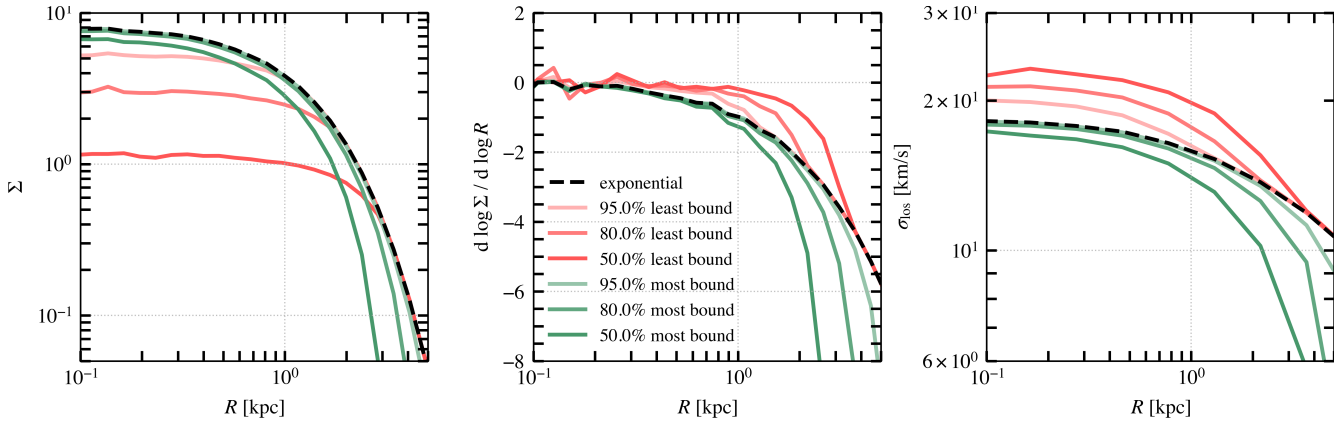

Figure 4.9: Properties of stellar populations resulting from strict limits imposed on the initial energy distribution. Red lines show the result of enforcing a minimum cut on $\mathscr{E}$ and green lines show the result of enforcing a maximum. The dashed black line corresponds to the exponential profile E1 depicted in figure 4.6.

an exponential model. Red lines show selections with a limit on the minimum energy and green lines show selections with a limit on the maximum energy applied to the E1m exponential model shown in figure 4.6. The chosen values of the energy minima or maxima are illustrated in figures 4.16 and 4.17 of the appendix.

Selecting only the most bound particles in the system (i.e., imposing an energy maxi-

mum) results in an increasingly steep truncation of the outer density profile, while selecting only the least bound particles (i.e., imposing an energy minimum) effectively removes mass from the centre, resulting in a constant density core of increasing prominence. As may be seen in figure 4.9, these changes are reflected in the corresponding Γ profiles with the transition from inner to outer slope more abrupt in the red curves and more gradual in the green profiles. Limiting the initial binding energies also has an effect on the velocity dispersion profile of the galaxy; imposing an energy minimum results in an increase to the central velocity dispersion, whereas imposing an energy maximum results in a steeper drop in velocity dispersion in the outer regions.

The result of adopting both a minimum and maximum energy cut (i.e., a slice in energy) is shown in figure 4.10, where we show these three profiles for the matching S2 model and compare it to a scaled version of the Fornax dwarf spheroidal, a galaxy which is thought to have been only marginally affected by tides (Borukhovetskaya et al., 2022a) and is fairly well approximated by an exponential profile in projection (Sestito et al., 2023). The S2 model is slightly more cored and steeply truncated than Fornax, resulting in a

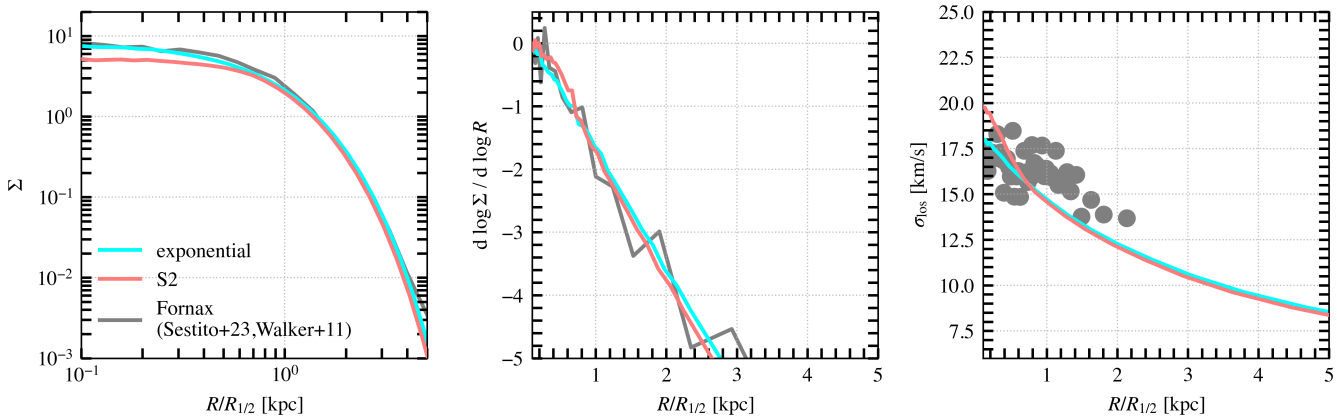

Figure 4.10: Properties of S2, our matching Antlia II model, (blue) compared to the Fornax dwarf spheroidal galaxy (grey). The Fornax surface density profile (Sestito et al., 2023) and velocity dispersion profile (Walker and Peñarrubia, 2011) have been scaled to match the 3D exponential model E1, drawn in dashed black. Panels as in figure 4.9.

centrally higher and steeper velocity dispersion profile, but it would be harsh to conclude from this comparison that S2 is inviable as a potential dSph model and, therefore, Antlia II's progenitor. Likewise, the Γ profiles align reasonably well out to twice the half-mass radius. Note as well that the deviations in the outer regions could be alleviated simply by choosing a higher energy maximum for S2. This would not change the structure of the tidal remnant, except for increasing the total stellar mass of the initial progenitor, as

the extra stars allowed by the increased maximum would have been tidally stripped earlier. Further observations may be able to search for signs of such energetically restricted galaxies accordingly.

4.4.3 Constant density core

We have seen above that it is possible to match Antlia II's observations by imposing energy constraints on an otherwise exponential model, assuming that allowed star binding energies are restricted inside a cuspy NFW halo. In particular, the minimum energy is the most critical, and should be chosen carefully to be relatively close to the energy cut introduced by the tides at the time of analysis. An alternative way to introduce a minimum energy is to consider the introduction of a constant density core in the dark matter halo. Figure 4.11 shows the initial binding energy distributions of cored Antlia II dark matter halos, as described in section 4.3.4.1, with core size varying from 0 to ~ 2 kpc. With increasing core size, an energy minimum is introduced, implying that progressively fewer particles occupy highly bound states, which would otherwise contribute to a central cusp.

We model here the evolution of an Antlia II halo with core size $r_c \approx 580$ pc. Figure 4.12 shows the evolution of the circular velocity within $r = (4/3)R_{1/2}$ of this cored Antlia II halo on orbit 1, with the evolution of the cuspy halo studied hitherto shown for reference. Note that while cuspy halos are expected to always leave behind a bound remnant (Errani and Navarro, 2021), the cored halo is susceptible to disruption (Errani et al., 2023) and indeed fully disrupts after just four pericentric passages.

We attempt first to answer whether a dark matter core is in itself sufficient to limit the initial stellar binding energies to values high enough to form a stellar core of the observed size. Figure 4.13 shows the result of a stellar population with no minimum cutoff in stellar binding energy. In this figure, the energy distributions are normalised using the potential minimum of the NFW halo discussed in section 4.4.2. Note that in the NFW case, the tidal boundary depicted in figure 4.6 with a dotted grey line occurs at roughly $\log(\mathscr{E}) \sim -0.4$, whereas in the cored scenario described here, the tidal boundary depicted with dash dotted grey in figure 4.13, is at $\log(\mathscr{E}) \sim -0.6$, as in this scenario the dark matter halo's ability to retain its particles is weakened. As demonstrated in the right panel, the resulting final density profile remains too small to match the observations. This suggests that, despite the inclusion of a sizeable core, we still need to impose an energy minimum ($\log(\mathscr{E}) \sim -0.7$) to reproduce the observed properties of Antlia II. A cored

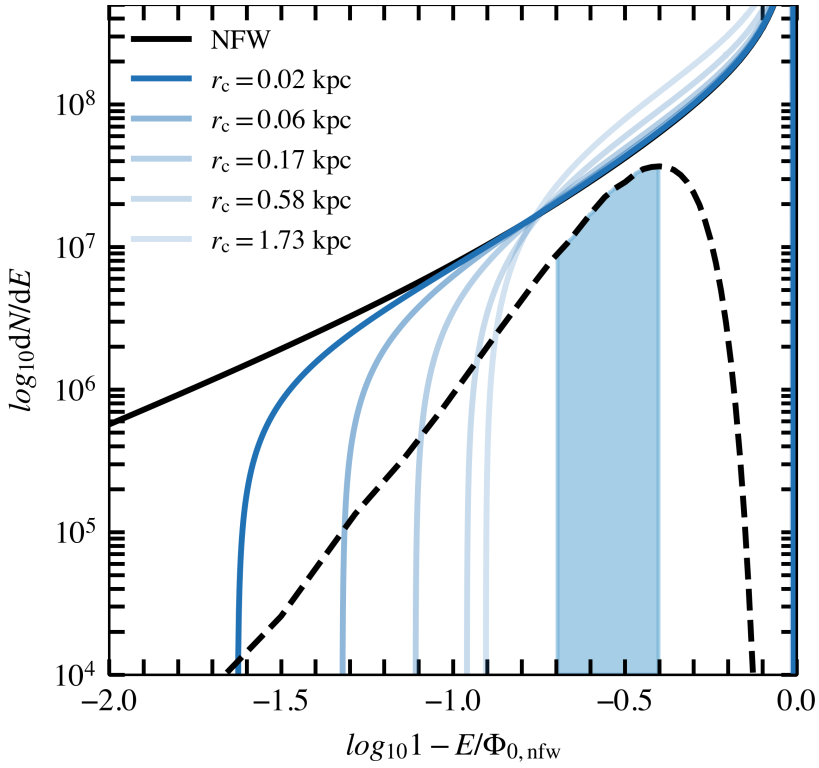

Figure 4.11: Binding energy distributions of cored Antlia II halos, with core size, r_c, ranging from 1/100 to 1 r_s. Initial energies are measured relative to the NFW potential minimum; the NFW energy distribution is shown for comparison in black. Plotted also for reference is the initial binding energy distribution of exponential model E1 in dashed black and of stellar component model S2 in shaded blue.

scenario without an imposed energy minimum may still be possible, but it would require a core larger than that adopted in our simulation.

Thus, we must partition the initial distribution of Antlia II stellar binding energies in a similar fashion as described for the case of a cuspy halo in section 4.4.2, though here following the underlying dark matter distribution rather than that of an exponential. The resulting stellar models are shown in figure 4.14.

Like in the case of a cuspy dark matter halo, the intermediate slice seems to reproduce fairly well the observed Antlia II surface density profile at $t_{\rm fin}$. Likewise, the velocity gradient for the matching blue slice in figure 4.14 is shown in figure 4.15 and appears consistent with the observed gradient. However, we emphasize again that the dark matter core modelled here is in itself insufficient to limit the initial stellar binding energies to values high enough to form a core of the observed size, requiring still a manually imposed

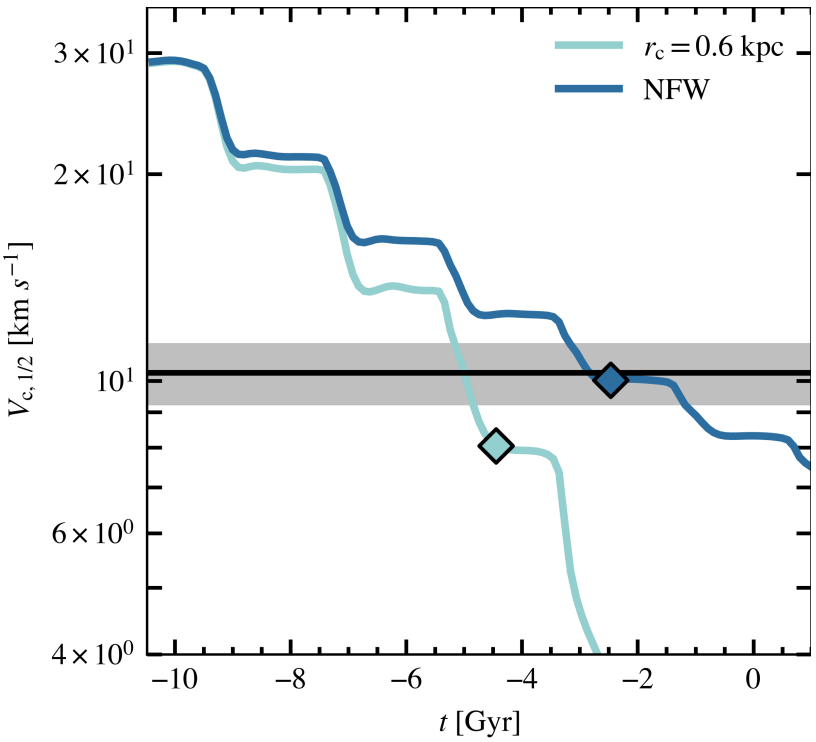

Figure 4.12: Evolution of the circular velocity at the estimated half-light radius of Antlia II (i.e., V_c at $r = 4/3 \times R_{1/2} = 3.4\,\mathrm{kpc}$) for our cuspy and cored halo model on two of the four different orbits explored for Antlia II. The horizontal black solid line and grey shaded region represent the observational constraint on V_c, as well as the $\pm 1\sigma$ uncertainty interval, taken from Ji et al. (2021). Diamonds indicate the snapshot(s) we identify for comparison with observational data.

minimum energy.

Torrealba et al. (2019) and Sameie et al. (2020) both similarly find that it is challenging to tidally produce a galaxy of similar size when embedded in a dark matter cusp, and hence argue that Antlia II likely resides in a cored halo. However further study is necessary to determine whether such large core sizes alone would be sufficient to form a stellar core as large as apparently needed to explain Antlia II; and moreover, whether the formation of such large cores is consistent with feedback mechanisms. In the `NewHorizon` hydrodynamical cosmological simulations, cores of the required size ($r_c \gtrsim 1.7\,\mathrm{kpc}$) are typically only found in galaxies with $M_\star \gtrsim 10^7\,\mathrm{M}_\odot$, compared to the $M_\star \approx 8.8 \times 10^5\,\mathrm{M}_\odot$ Torrealba et al. (2019) quote for Antlia II.

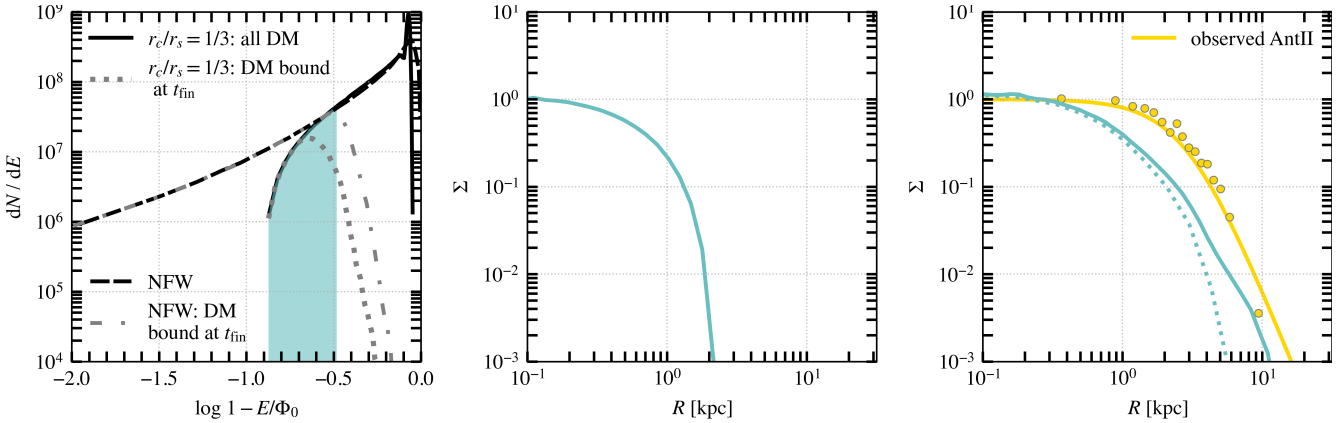

Figure 4.13: As in figure 4.6 but for a cored Antlia II model. The energy distribution of the NFW halo and bound portion shown in black and grey, respectively, in figure 4.6, are shown also here for reference in dashed black and dash dotted grey. The curve in the central panel is normalised such that the final central density is $\Sigma_0 = 1$. As evidenced in the right panel, a dark matter halo core in itself is insufficient to limit the initial stellar binding energies to values high enough to in the final stellar density profiles form a core of the observed size.

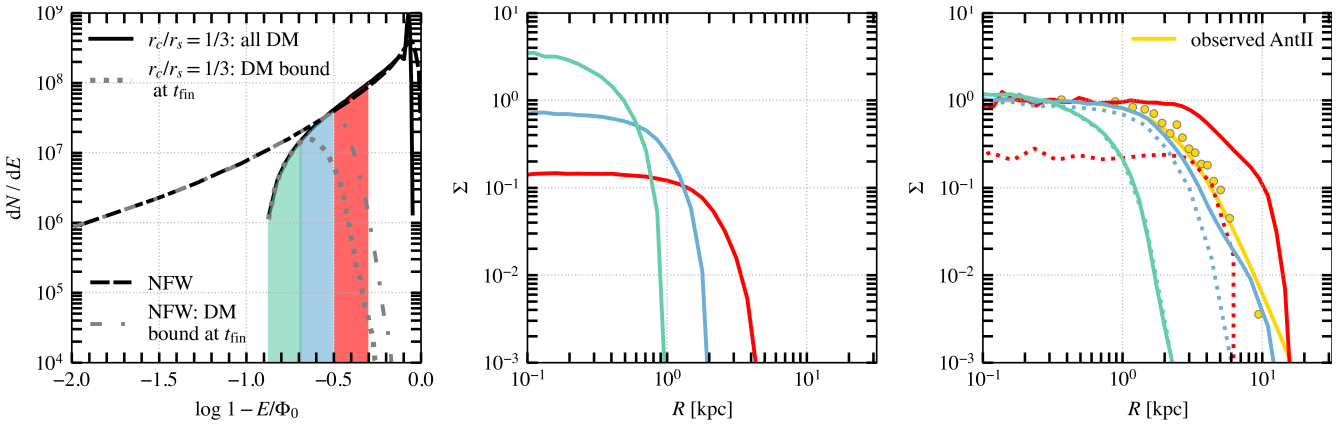

Figure 4.14: As in figure 4.6 but for a cored Antlia II model. The energy distribution of the NFW halo and bound portion shown in black and grey, respectively, in figure 4.6, are shown also here for reference in dashed black and dash dotted grey. The green curve in the central panel is normalised such that the final central density is $\Sigma_0 = 1$, and the blue and red curves use the same normalisation. With a similar cutoff in energy as implemented in figure 4.6, the blue selection in the left panel seems to reproduce reasonably well in the right panel the observed Antlia II surface density profile.

4.5 Summary and conclusions

Using N-body simulations, we have examined how Galactic tides impact the evolution of possible models for the progenitor of the Antlia II dwarf spheroidal galaxy. The pri-

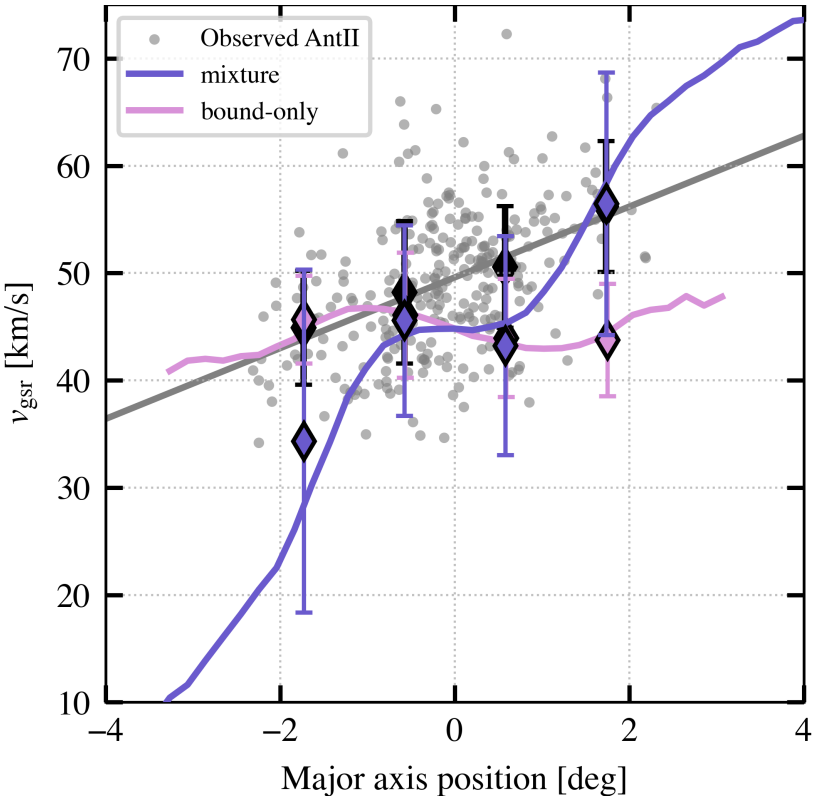

Figure 4.15: At final snapshot, radial velocities of blue selection depicted in figure 4.14 measured along the major axis, plotted against observed radial velocities of Antlia II members from Ji et al. (2021). Diamond errorbars indicate mean values of the illustrated points (selected as high probability stellar particles which on the sky lie near to members of Ji et al. (2021)), while the purple line reflects the entire Antlia II selection.

mary objective of this work is to investigate whether tidal effects can bring into agreement the peculiar size and kinematics of Antlia II with predictions from LCDM cosmological hydrodynamical simulations. Our model assumes the following: (i) Antlia II initially formed as a dark matter-dominated spherical stellar system with no net rotation, and (ii) the maximum circular velocity of Antlia II at infall is 28.4 $\mathrm{km\,s^{-1}}$, with an average concentration in line with recent LCDM cosmological hydrodynamical simulations of the Local Group. The key findings of our study may be summarized as follows:

(i) The pericentric distance of Antlia II is not well determined. We use the latest available data for the sky position, distance, radial velocity, and proper motions of Antlia II from various authors, together with a Galactic potential model that matches the observed circular velocity at the solar radius, to find that the allowed pericentric distance lies roughly between ~ 20 and ~ 70 kpc.

(ii) Assuming that Antlia II initially formed in an NFW halo with maximum circular velocity $V_{\rm max} \approx 28$ km s^{-1}, as suggested by results of the APOSTLE suite of LCDM Local Group simulations, we find that Galactic tides are able to reduce, in a Hubble time, the characteristic circular velocity of the remnant to ~ 10 km s^{-1} (as required to match Antlia II's low $\sigma_{\rm los} \sim 6$ km s^{-1}) if placed on an orbit with $r_{\rm peri} \lesssim 35$ kpc.

(iii) After being tidally stripped, the bound component of an initially exponential stellar component is unable match the surface density profile or the observed velocity gradient of Antlia II. A model including both bound and unbound particles is able to reproduce the velocity gradient by including unbound stars which have not yet had time to escape after being unbound by tidal forces during the most recent pericentric passage. The inclusion of unbound material, however, is unable to fix the disagreement between the model and the observed surface density profiles. The observed profiles have core radii and half-light radii that much larger than may be explained by tidally truncating exponential stellar models.

(iv) The disagreement is likely to persist for any stellar models with a substantial number of stars at low values (i.e., very bound) of the initial binding energy $\mathscr{E}$. Reproducing the large observed size of Antlia II in a cuspy dark matter halo requires imposing a minimum limit on the initial stellar binding energy. This limit may have been imposed by baryonic effects during the formation of the galaxy, or by the presence of a constant density core in the underlying dark matter distribution. Further study is needed to determine whether the formation of such large core sizes in Antlia II is consistent with feedback mechanisms. As only the minimum limit is crucial to reproducing the large size of the dwarf, the maximum limit may be adjusted such that the stellar mass lost by the system is in line with the predictions of Ji et al. (2021) (roughly 50% or less) based off the dSph's position on the mass-metallicity relation.

The unusual properties of Antlia II are shared by other satellite galaxies in the Local Group, such as Crater II, And XXV and And XXI. Each of these galaxies is similarly difficult to reproduce with a tidal interpretation in the standard LCDM scenario. An energetically restricted galaxy at infall could in principle reconcile these galaxies with predictions from LCDM. Detailed observations of galaxies' density, Γ, and velocity dispersion profiles may help provide insight into the likelihood of such a formation scenario.

4.6 Appendix

This appendix presents the binding energy distributions along with initial and final density profiles of stellar populations resulting from strict limits imposed on the initial energy distribution.

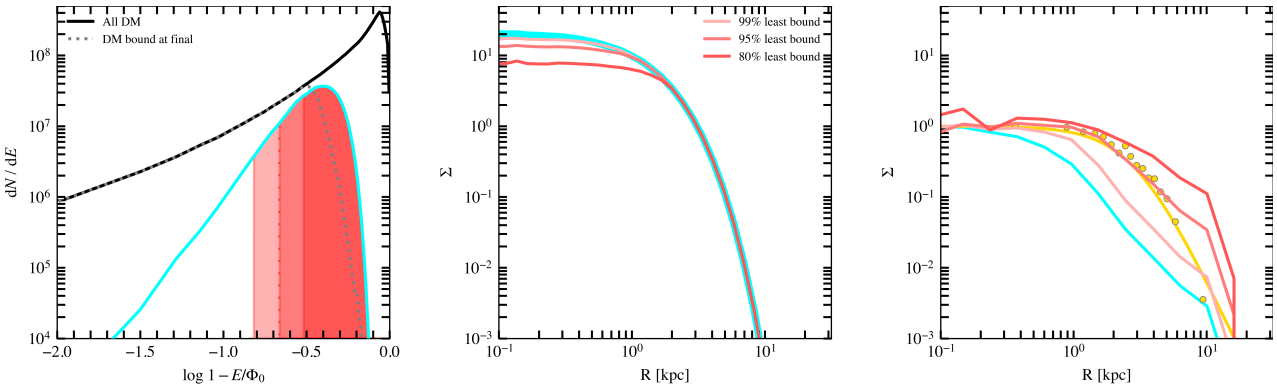

Figure 4.16: Properties of stellar populations resulting from strict limits imposed on the initial energy distribution. Red lines show the result of enforcing a minimum cut on $\log(\mathscr{E})$ at around —0.65 (95% least bound particles), —0.5 (80% least bound particles), and —0.4 (50% least bound particles). The central panel shows the corresponding initial density profiles, and the right panel shows the density profiles at $t_{\rm fin}$. The dashed black line corresponds to the exponential profile E1m depicted in figure 4.6.

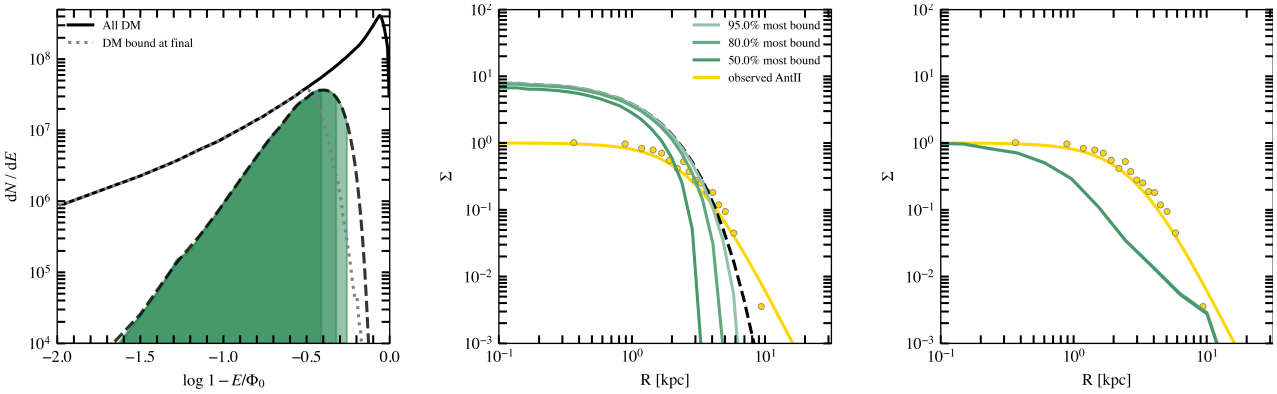

Figure 4.17: Properties of stellar populations resulting from strict limits imposed on the initial energy distribution. Green lines show the result of enforcing a maximum cut on $\log(\mathscr{E})$ at around —0.25 (95% most bound particles), —0.3 (80% most bound particles), and —0.4 (50% most bound particles). The central panel shows the corresponding initial density profiles, and the right panel shows the density profiles at $t_{\rm fin}$. The dashed black line corresponds to the exponential profile E1m depicted in figure 4.6.

Chapter 5

Summary and Conclusions

Lying at the faintest end of the galaxy luminosity function, dwarf spheroidal galaxies are remarkably dark matter dominated, exhibiting dynamical mass-to-light ratios which may reach values as high as $M/L \sim 10^4$. It is this quality that makes them well suited for studying the properties of dark matter on small scales.

In this dissertation I have discussed the effects of Galactic tides on the evolution of dwarf spheroidal galaxies embedded in cuspy cold dark matter subhaloes which orbit under the tidal effects of the Milky Way. In particular, I present detailed N-body models and analysis of the evolution of Fornax, Crater II, and Antlia II within this context. I summarize below briefly the main results presented here.

I. The low dark matter content of Fornax results from the effect of Galactic tides

As inferred from its kinematics, the dark matter content of Fornax, one of the most studied nearby dwarf spheroidal galaxies, is substantially lower than expected from ΛCDM cosmological simulations. In addition, the spatial distribution of its globular clusters seems inconsistent with the fact that their dynamical friction orbital decay timescales appear to be much shorter than their ages. We investigated both these problems in the context of Galactic tides and found the following:

(i) Using the latest available data for the sky position, distance, radial velocity and proper motion of Fornax, together with a Galactic potential model that matches the most recent Milky Way dynamical constraints, we conclude that the pericentric distance of Fornax's orbit is only loosely constrained - ranging between 50 and 130 kpc.

(ii) Despite losing an appreciable quantity of dark mass to tides on an eccentric orbit with $r_{\rm peri} \sim 50\,{\rm kpc}$ (as required to lower the velocity dispersion to the observed value), the stellar component of Fornax remains relatively unaffected, losing less than 5% of its mass and exhibiting only very faint observable tidal signatures.

(iii) Similarly, the effect of Galactic tides on the decay times of Fornax's population of globular clusters due to dynamical friction is minor compared with models run in isolation. A population of globular clusters with initial orbital radii between 1 and 2 kpc is consistent with their present-day spatial distribution.

II. Feeble giants present a challenge to ΛCDM

The unusually low velocity dispersions and large sizes of feeble giants, such as Crater II and Antlia II, pose a challenge to our understanding of dwarf galaxies in ΛCDM. Their low velocity dispersions suggest dark matter haloes that are in the late stages of extreme tidal stripping, however their large sizes seem inconsistent with this scenario. We investigate whether it is possible to reproduce such peculiar galaxies under the effect of Galactic tides and find the following:

(iv) Because only roughly a decade in surface brightness in the Crater II surface brightness profile has been resolved, the half-light radius of Crater II is poorly constrained due to the uncertain shape of the outer density profile. For such cases, we emphasize the need to use a more reliable size measure, such as the core radius, which is less affected by assumptions about the outer profile shape when comparing simulation results against observations.

(v) As for Fornax, the pericentric distances of Crater II and Antlia II are not well constrained and can range from 10 to 50 kpc and from 20 to 70 kpc, respectively.

(vi) The low Galactocentric radial velocities of Crater II and Antlia II, together with their large distances, imply that the two dSphs are just past and just prior to their current apocentric passages, respectively. More importantly, their latest pericentric passages occurred roughly ~ 1 Gyr ago, meaning that the inner regions of Crater II and Antlia II should be close to dynamical equilibrium.

(vii) Like for Fornax, we take the initial mass of the Crater II and Antlia II progenitor halos from the $M_\star - M_{\rm halo}$ relation of the APOSTLE suite of Local Group simula-

tions, and find that tides are able to reduce their characteristic velocities to values consistent with the observed line-of-sight velocity dispersions.

(viii) The large sizes of Crater II and Antlia II are much more difficult to reproduce in a tidal scenario where the initial stellar components are assumed to be exponential. This is because stellar models which extend to low values of initial binding energy $\mathscr{E}$ (such as an exponential) will inevitably evolve to core radii far smaller than observed when stripped enough to match the observed velocity dispersions. Reproducing the large observed sizes of feeble giants such as Crater II and Antlia II apparently requires imposing a minimum limit on the initial stellar binding energy. This may result from baryonic processes during galaxy formation, or may also arise as a natural consequence of a large constant density core in the underlying dark matter distribution.

(ix) Reproducing the observed velocity gradient of Antlia II requires including in its member population both bound and unbound particles. Only then are the tidal tails sampled sufficiently to form an significant velocity gradient in line with what is observed.

III. Future prospects

In light of continued discoveries of increasingly faint Milky Way satellites, many of which show no clear evidence of tidal perturbation, it is vital to assess the tidal impact on the Milky Way satellites at large and what, if any, the observable consequences of such tidal effects are. Aside from puzzling objects such as Crater II and Antlia II, as discussed in this dissertation, many other dSphs pose unique challenges to our understanding of the tidal evolution of our satellite neighbours.

For example, Tucana III is found to be orbiting with a tiny pericentre of only $\sim 2\,\mathrm{kpc}$ and a very short orbital time, raising the question of how such a satellite has managed to survive without disrupting to this day (Erkal et al., 2018). By means of dynamical modelling, such as the framework that is used in this thesis, it should be possible to identify tidal signatures and to quantify the strength of such features. For example, computations of break radii (described in section 1.3), as performed in chapters 3 and 4, may provide insight into whether breaks or bumps in the outer profiles of dSphs are tidal in origin. The recent third data release from the *Gaia* satellite and similar emerging surveys have enabled the study of the dynamics of nearby galaxies at an unprecedented level of accu-

racy, and by turning our attention to our neighbouring dSph satellites, we may move closer to understanding the nature of dark matter and the Universe itself.

Bibliography

L. A. Aguilar and S. D. M. White. The Density Profiles of Tidally Stripped Galaxies. *ApJ*, 307:97, Aug. 1986. doi: 10.1086/164396.

N. C. Amorisco. Giant cold satellites from low-concentration haloes. *MNRAS*, 489(1): L22–L27, Oct. 2019. doi: 10.1093/mnrasl/slz121.

N. C. Amorisco, A. Agnello, and N. W. Evans. The core size of the Fornax dwarf spheroidal. *MNRAS*, 429:L89–L93, Feb. 2013. doi: 10.1093/mnrasl/sls031.

G. W. Angus and A. Diaferio. Resolving the timing problem of the globular clusters orbiting the Fornax dwarf galaxy. *MNRAS*, 396(2):887–893, June 2009. doi: 10.1111/j.1365-2966.2009.14745.x.

E. Applebaum, A. M. Brooks, C. R. Christensen, F. Munshi, T. R. Quinn, S. Shen, and M. Tremmel. Ultrafaint Dwarfs in a Milky Way Context: Introducing the Mint Condition DC Justice League Simulations. *ApJ*, 906(2):96, Jan. 2021. doi: 10.3847/1538-4357/abcafa.

J. Barnes and P. Hut. A hierarchical O(N log N) force-calculation algorithm. *Nature*, 324 (6096):446–449, Dec. 1986. doi: 10.1038/324446a0.

G. Battaglia, A. Sollima, and C. Nipoti. The effect of tides on the Fornax dwarf spheroidal galaxy. *MNRAS*, 454(3):2401–2415, Dec. 2015. doi: 10.1093/mnras/stv2096.

P. S. Behroozi, R. H. Wechsler, and C. Conroy. The Average Star Formation Histories of Galaxies in Dark Matter Halos from z = 0-8. *ApJ*, 770(1):57, June 2013. doi: 10.1088/0004-637X/770/1/57.

A. Benitez-Llambay and C. Frenk. The detailed structure and the onset of galaxy formation in low-mass gaseous dark matter haloes. *MNRAS*, 498(4):4887–4900, Nov. 2020. doi: 10.1093/mnras/staa2698.

A. Benítez-Llambay, C. S. Frenk, A. D. Ludlow, and J. F. Navarro. Baryon-induced dark matter cores in the EAGLE simulations. *MNRAS*, 488(2):2387–2404, Sept. 2019. doi: 10.1093/mnras/stz1890.

A. J. Benson, C. G. Lacey, C. M. Baugh, S. Cole, and C. S. Frenk. The effects of photoionization on galaxy formation - I. Model and results at z=0. *MNRAS*, 333(1):156–176, June 2002. doi: 10.1046/j.1365-8711.2002.05387.x.

P. Boldrini, R. Mohayaee, and J. Silk. Fornax globular cluster distributions: implications for the cusp-core problem. *MNRAS*, 485(2):2546–2557, May 2019. doi: 10.1093/mnras/stz573.

A. Borukhovetskaya, R. Errani, J. F. Navarro, A. Fattahi, and I. Santos-Santos. The tidal evolution of the Fornax dwarf spheroidal and its globular clusters. *MNRAS*, 509(4):5330–5339, Feb. 2022a. doi: 10.1093/mnras/stab2912.

A. Borukhovetskaya, J. F. Navarro, R. Errani, and A. Fattahi. Galactic tides and the Crater II dwarf spheroidal: a challenge to LCDM? *MNRAS*, 512(4):5247–5257, June 2022b. doi: 10.1093/mnras/stac653.

J. S. Bullock and K. V. Johnston. Tracing Galaxy Formation with Stellar Halos. I. Methods. *ApJ*, 635(2):931–949, Dec. 2005. doi: 10.1086/497422.

J. S. Bullock, A. V. Kravtsov, and D. H. Weinberg. Reionization and the Abundance of Galactic Satellites. *ApJ*, 539(2):517–521, Aug. 2000. doi: 10.1086/309279.

N. Caldwell, M. G. Walker, M. Mateo, E. W. Olszewski, S. Koposov, V. Belokurov, G. Torrealba, A. Geringer-Sameth, and C. I. Johnson. Crater 2: An Extremely Cold Dark Matter Halo. *ApJ*, 839(1):20, Apr. 2017. doi: 10.3847/1538-4357/aa688e.

S. Chandrasekhar. Dynamical Friction. I. General Considerations: the Coefficient of Dynamical Friction. . *ApJ*, 97:255, Mar. 1943. doi: 10.1086/144517.

J.-H. Choi, M. D. Weinberg, and N. Katz. The dynamics of satellite disruption in cold dark matter haloes. *MNRAS*, 400(3):1247–1263, Dec. 2009. doi: 10.1111/j.1365-2966.2009.15556.x.

D. R. Cole, W. Dehnen, J. I. Read, and M. I. Wilkinson. The mass distribution of the Fornax dSph: constraints from its globular cluster distribution. *MNRAS*, 426(1):601–613, Oct. 2012. doi: 10.1111/j.1365-2966.2012.21885.x.

M. G. Coleman, G. S. Da Costa, J. Bland-Hawthorn, and K. C. Freeman. A Wide-Field Survey of the Fornax Dwarf Spheroidal Galaxy. *AJ*, 129(3):1443–1464, Mar. 2005. doi: 10.1086/427966.

M. L. M. Collins, E. J. Tollerud, R. M. Rich, R. A. Ibata, N. F. Martin, S. C. Chapman, K. M. Gilbert, and J. Preston. A detailed study of Andromeda XIX, an extreme local analogue of ultradiffuse galaxies. *MNRAS*, 491(3):3496–3514, Jan. 2020. doi: 10.1093/mnras/stz3252.

M. L. M. Collins, J. I. Read, R. A. Ibata, R. M. Rich, N. F. Martin, J. Peñarrubia, S. C. Chapman, E. J. Tollerud, and D. R. Weisz. Andromeda XXI - a dwarf galaxy in a low-density dark matter halo. *MNRAS*, 505(4):5686–5701, Aug. 2021. doi: 10.1093/mnras/stab1624.

C. Conroy, R. H. Wechsler, and A. V. Kravtsov. Modeling Luminosity-dependent Galaxy Clustering through Cosmic Time. *ApJ*, 647(1):201–214, Aug. 2006. doi: 10.1086/503602.

A. J. Deason, D. Erkal, V. Belokurov, A. Fattahi, F. A. Gómez, R. J. J. Grand, R. Pakmor, X.-X. Xue, C. Liu, C. Yang, L. Zhang, and G. Zhao. The mass of the Milky Way out to 100 kpc using halo stars. *MNRAS*, 501(4):5964–5972, Mar. 2021. doi: 10.1093/mnras/staa3984.

W. Dehnen. A Hierarchical <E10>O</E10>(N) Force Calculation Algorithm. *Journal of Computational Physics*, 179(1):27–42, June 2002. doi: 10.1006/jcph.2002.7026.

A. Di Cintio, C. B. Brook, A. V. Macciò, G. S. Stinson, A. Knebe, A. A. Dutton, and J. Wadsley. The dependence of dark matter profiles on the stellar-to-halo mass ratio: a prediction for cusps versus cores. *MNRAS*, 437(1):415–423, Jan. 2014. doi: 10.1093/mnras/stt1891.

D. I. Dinescu, B. A. Keeney, S. R. Majewski, and T. M. Girard. Absolute Proper Motion of the Fornax Dwarf Spheroidal Galaxy from Photographic and Hubble Space Telescope WFPC2 Data. *AJ*, 128(2):687–699, Aug. 2004. doi: 10.1086/422491.

A. S. Eddington. The distribution of stars in globular clusters. *MNRAS*, 76:572–585, May 1916. doi: 10.1093/mnras/76.7.572.

G. Efstathiou. Suppressing the formation of dwarf galaxies via photoionization. *MNRAS*, 256:43P–47P, May 1992. doi: 10.1093/mnras/256.1.43P.

J. Einasto. On the Construction of a Composite Model for the Galaxy and on the Determination of the System of Galactic Parameters. *Trudy Astrofizicheskogo Instituta Alma-Ata*, 5:87–100, Jan. 1965.

D. Erkal, V. Belokurov, C. F. P. Laporte, S. E. Koposov, T. S. Li, C. J. Grillmair, N. Kallivayalil, A. M. Price-Whelan, N. W. Evans, K. Hawkins, D. Hendel, C. Mateu, J. F. Navarro, A. del Pino, C. T. Slater, S. T. Sohn, and Orphan Aspen Treasury Collaboration. The total mass of the Large Magellanic Cloud from its perturbation on the Orphan stream. *MNRAS*, 487(2):2685–2700, Aug. 2019. doi: 10.1093/mnras/stz1371.

Erkal et al. Modelling the Tucana III stream - a close passage with the LMC. *MNRAS*, 481 (3):3148–3159, Dec. 2018. doi: 10.1093/mnras/sty2518.

R. Errani and J. F. Navarro. The asymptotic tidal remnants of cold dark matter subhaloes. *MNRAS*, 505(1):18–32, July 2021. doi: 10.1093/mnras/stab1215.

R. Errani and J. Peñarrubia. Can tides disrupt cold dark matter subhaloes? *MNRAS*, 491 (4):4591–4601, Feb. 2020. doi: 10.1093/mnras/stz3349.

R. Errani, J. Peñarrubia, and G. Tormen. Constraining the distribution of dark matter in dwarf spheroidal galaxies with stellar tidal streams. *MNRAS*, 449:L46–L50, Apr. 2015. doi: 10.1093/mnrasl/slv012.

R. Errani, J. Peñarrubia, and M. G. Walker. Systematics in virial mass estimators for pressure-supported systems. *MNRAS*, 481(4):5073–5090, Dec. 2018. doi: 10.1093/mnras/sty2505.

R. Errani, J. F. Navarro, R. Ibata, and J. Peñarrubia. Structure and kinematics of tidally limited satellite galaxies in LCDM. *MNRAS*, 511(4):6001–6018, Apr. 2022. doi: 10.1093/mnras/stac476.

R. Errani, J. F. Navarro, J. Peñarrubia, B. Famaey, and R. Ibata. Dark matter halo cores and the tidal survival of Milky Way satellites. *MNRAS*, 519(1):384–396, Feb. 2023. doi: 10.1093/mnras/stac3499.

A. Fattahi, J. F. Navarro, T. Sawala, C. S. Frenk, K. A. Oman, R. A. Crain, M. Furlong, M. Schaller, J. Schaye, T. Theuns, and A. Jenkins. The APOSTLE project: Local Group kinematic mass constraints and simulation candidate selection. *MNRAS*, 457(1):844–856, Mar. 2016a. doi: 10.1093/mnras/stv2970.

A. Fattahi, J. F. Navarro, T. Sawala, C. S. Frenk, L. V. Sales, K. Oman, M. Schaller, and J. Wang. The cold dark matter content of Galactic dwarf spheroidals: no cores, no failures, no problem. *arXiv e-prints*, art. arXiv:1607.06479, July 2016b.

A. Fattahi, J. F. Navarro, C. S. Frenk, K. A. Oman, T. Sawala, and M. Schaller. Tidal stripping and the structure of dwarf galaxies in the Local Group. *MNRAS*, 476(3): 3816–3836, May 2018. doi: 10.1093/mnras/sty408.

D. A. Forbes, J. I. Read, M. Gieles, and M. L. M. Collins. Extending the globular cluster system-halo mass relation to the lowest galaxy masses. *MNRAS*, 481(4):5592–5605, Dec. 2018. doi: 10.1093/mnras/sty2584.

J. Frings, A. Macciò, T. Buck, C. Penzo, A. Dutton, M. Blank, and A. Obreja. The edge of galaxy formation - II. Evolution of Milky Way satellite analogues after infall. *MNRAS*, 472(3):3378–3389, Dec. 2017. doi: 10.1093/mnras/stx2171.

T. K. Fritz, G. Battaglia, M. S. Pawlowski, N. Kallivayalil, R. van der Marel, S. T. Sohn, C. Brook, and G. Besla. Gaia DR2 proper motions of dwarf galaxies within 420 kpc. Orbits, Milky Way mass, tidal influences, planar alignments, and group infall. *A&A*, 619:A103, Nov. 2018. doi: 10.1051/0004-6361/201833343.

S. W. Fu, J. D. Simon, and A. G. Alarcón Jara. Dynamical Histories of the Crater II and Hercules Dwarf Galaxies. *ApJ*, 883(1):11, Sept. 2019. doi: 10.3847/1538-4357/ab3658.

Gaia Collaboration, A. Helmi, F. van Leeuwen, P. J. McMillan, D. Massari, T. Antoja, A. C. Robin, L. Lindegren, U. Bastian, F. Arenou, C. Babusiaux, M. Biermann, M. A. Breddels, D. Hobbs, C. Jordi, E. Pancino, C. Reylé, J. Veljanoski, A. G. A. Brown, A. Vallenari, T. Prusti, J. H. J. de Bruijne, C. A. L. Bailer-Jones, D. W. Evans, L. Eyer, F. Jansen, S. A. Klioner, U. Lammers, X. Luri, F. Mignard, C. Panem, D. Pourbaix, S. Randich, P. Sartoretti, H. I. Siddiqui, C. Soubiran, N. A. Walton, M. Cropper, R. Drimmel, D. Katz, M. G. Lattanzi, J. Bakker, C. Cacciari, J. Castañeda, L. Chaoul, N. Cheek, F. De Angeli, C. Fabricius, R. Guerra, B. Holl, E. Masana, R. Messineo, N. Mowlavi, K. Nienartowicz, P. Panuzzo, J. Portell, M. Riello, G. M. Seabroke, P. Tanga, F. Thévenin, G. Gracia-Abril, G. Comoretto, M. Garcia-Reinaldos, D. Teyssier, M. Altmann, R. Andrae, M. Audard, I. Bellas-Velidis, K. Benson, J. Berthier, R. Blomme, P. Burgess, G. Busso, B. Carry, A. Cellino, G. Clementini, M. Clotet, O. Creevey, M. Davidson, J. De Ridder, L. Delchambre, A. Dell'Oro, C. Ducourant, J. Fernández-Hernández, M. Fouesneau, Y. Frémat,

L. Galluccio, M. García-Torres, J. González-Núñez, J. J. González-Vidal, E. Gosset, L. P. Guy, J. L. Halbwachs, N. C. Hambly, D. L. Harrison, J. Hernández, D. Hestroffer, S. T. Hodgkin, A. Hutton, G. Jasniewicz, A. Jean-Antoine-Piccolo, S. Jordan, A. J. Korn, A. Krone-Martins, A. C. Lanzafame, T. Lebzelter, W. Löffler, M. Manteiga, P. M. Marrese, J. M. Martín-Fleitas, A. Moitinho, A. Mora, K. Muinonen, J. Osinde, T. Pauwels, J. M. Petit, A. Recio-Blanco, P. J. Richards, L. Rimoldini, L. M. Sarro, C. Siopis, M. Smith, A. Sozzetti, M. Süveges, J. Torra, W. van Reeven, U. Abbas, A. Abreu Aramburu, S. Accart, C. Aerts, G. Altavilla, M. A. Álvarez, R. Alvarez, J. Alves, R. I. Anderson, A. H. Andrei, E. Anglada Varela, E. Antiche, B. Arcay, T. L. Astraatmadja, N. Bach, S. G. Baker, L. Balaguer-Núñez, P. Balm, C. Barache, C. Barata, D. Barbato, F. Barblan, P. S. Barklem, D. Barrado, M. Barros, M. A. Barstow, S. Bartholomé Muñoz, J. L. Bassilana, U. Becciani, M. Bellazzini, A. Berihuete, S. Bertone, L. Bianchi, O. Bienaymé, S. Blanco-Cuaresma, T. Boch, C. Boeche, A. Bombrun, R. Borrachero, D. Bossini, S. Bouquillon, G. Bourda, A. Bragaglia, L. Bramante, A. Bressan, N. Brouillet, T. Brüsemeister, E. Brugaletta, B. Bucciarelli, A. Burlacu, D. Busonero, A. G. Butkevich, R. Buzzi, E. Caffau, R. Cancelliere, G. Cannizzaro, T. Cantat-Gaudin, R. Carballo, T. Carlucci, J. M. Carrasco, L. Casamiquela, M. Castellani, A. Castro-Ginard, P. Charlot, L. Chemin, A. Chiavassa, G. Cocozza, G. Costigan, S. Cowell, F. Crifo, M. Crosta, C. Crowley, J. Cuypers, C. Dafonte, Y. Damerdji, A. Dapergolas, P. David, M. David, P. de Laverny, F. De Luise, R. De March, D. de Martino, R. de Souza, A. de Torres, J. Debosscher, E. del Pozo, M. Delbo, A. Delgado, H. E. Delgado, P. Di Matteo, S. Diakite, C. Diener, E. Distefano, C. Dolding, P. Drazinos, J. Durán, B. Edvardsson, H. Enke, K. Eriksson, P. Esquej, G. Eynard Bontemps, C. Fabre, M. Fabrizio, S. Faigler, A. J. Falcão, M. Farràs Casas, L. Federici, G. Fedorets, P. Fernique, F. Figueras, F. Filippi, K. Findeisen, A. Fonti, E. Fraile, M. Fraser, B. Frézouls, M. Gai, S. Galleti, D. Garabato, F. García-Sedano, A. Garofalo, N. Garralda, A. Gavel, P. Gavras, J. Gerssen, R. Geyer, P. Giacobbe, G. Gilmore, S. Girona, G. Giuffrida, F. Glass, M. Gomes, M. Granvik, A. Gueguen, A. Guerrier, J. Guiraud, R. Gutiérrez-Sánchez, W. Hofmann, G. Holland, H. E. Huckle, A. Hypki, V. Icardi, K. Janßen, G. Jevardat de Fombelle, P. G. Jonker, Á. L. Juhász, F. Julbe, A. Karampelas, A. Kewley, J. Klar, A. Kochoska, R. Kohley, K. Kolenberg, M. Kontizas, E. Kontizas, S. E. Koposov, G. Kordopatis, Z. Kostrzewa-Rutkowska, P. Koubsky, S. Lambert, A. F. Lanza, Y. Lasne, J. B. Lavigne, Y. Le Fustec, C. Le Poncin-Lafitte, Y. Lebreton, S. Leccia, N. Leclerc, I. Lecoeur-Taibi, H. Lenhardt, F. Leroux, S. Liao, E. Licata, H. E. P. Lindstrøm, T. A. Lister,

E. Livanou, A. Lobel, M. López, S. Managau, R. G. Mann, G. Mantelet, O. Marchal, J. M. Marchant, M. Marconi, S. Marinoni, G. Marschalkó, D. J. Marshall, M. Martino, G. Marton, N. Mary, G. Matijevič, T. Mazeh, S. Messina, D. Michalik, N. R. Millar, D. Molina, R. Molinaro, L. Molnár, P. Montegriffo, R. Mor, R. Morbidelli, T. Morel, D. Morris, A. F. Mulone, T. Muraveva, I. Musella, G. Nelemans, L. Nicastro, L. Noval, W. O'Mullane, C. Ordénovic, D. Ordóñez-Blanco, P. Osborne, C. Pagani, I. Pagano, F. Pailler, H. Palacin, L. Palaversa, A. Panahi, M. Pawlak, A. M. Piersimoni, F. X. Pineau, E. Plachy, G. Plum, E. Poggio, E. Poujoulet, A. Prša, L. Pulone, E. Racero, S. Ragaini, N. Rambaux, M. Ramos-Lerate, S. Regibo, F. Riclet, V. Ripepi, A. Riva, A. Rivard, G. Rixon, T. Roegiers, M. Roelens, M. Romero-Gómez, N. Rowell, F. Royer, L. Ruiz-Dern, G. Sadowski, T. Sagristà Sellés, J. Sahlmann, J. Salgado, E. Salguero, N. Sanna, T. Santana-Ros, M. Sarasso, H. Savietto, M. Schultheis, E. Sciacca, M. Segol, J. C. Segovia, D. Ségransan, I. C. Shih, L. Siltala, A. F. Silva, R. L. Smart, K. W. Smith, E. Solano, F. Solitro, R. Sordo, S. Soria Nieto, J. Souchay, A. Spagna, F. Spoto, U. Stampa, I. A. Steele, H. Steidelmüller, C. A. Stephenson, H. Stoev, F. F. Suess, J. Surdej, L. Szabados, E. Szegedi-Elek, D. Tapiador, F. Taris, G. Tauran, M. B. Taylor, R. Teixeira, D. Terrett, P. Teyssandier, W. Thuillot, A. Titarenko, F. Torra Clotet, C. Turon, A. Ulla, E. Utrilla, S. Uzzi, M. Vaillant, G. Valentini, V. Valette, A. van Elteren, E. Van Hemelryck, M. van Leeuwen, M. Vaschetto, A. Vecchiato, Y. Viala, D. Vicente, S. Vogt, C. von Essen, H. Voss, V. Votruba, S. Voutsinas, G. Walmsley, M. Weiler, O. Wertz, T. Wevems, Ł. Wyrzykowski, A. Yoldas, M. Žerjal, H. Ziaeepour, J. Zorec, S. Zschocke, S. Zucker, C. Zurbach, and T. Zwitter. Gaia Data Release 2. Kinematics of globular clusters and dwarf galaxies around the Milky Way. *A&A*, 616:A12, Aug. 2018. doi: 10.1051/0004-6361/201832698.

S. Garrison-Kimmel, P. F. Hopkins, A. Wetzel, J. S. Bullock, M. Boylan-Kolchin, D. Kereš, C.-A. Faucher-Giguère, K. El-Badry, A. Lamberts, E. Quataert, and R. Sanderson. The Local Group on FIRE: dwarf galaxy populations across a suite of hydrodynamic simulations. *MNRAS*, 487(1):1380–1399, July 2019. doi: 10.1093/mnras/stz1317.

A. Genina, J. I. Read, A. Fattahi, and C. S. Frenk. Can tides explain the low dark matter density in Fornax? *arXiv e-prints*, art. arXiv:2011.09482, Nov. 2020.

N. Y. Gnedin. Effect of Reionization on Structure Formation in the Universe. *ApJ*, 542: 535–541, Oct. 2000. doi: 10.1086/317042.

O. Y. Gnedin, A. V. Kravtsov, A. A. Klypin, and D. Nagai. Response of Dark Matter Halos to Condensation of Baryons: Cosmological Simulations and Improved Adiabatic Contraction Model. *ApJ*, 616(1):16–26, Nov. 2004. doi: 10.1086/424914.

T. Goerdt, B. Moore, J. I. Read, J. Stadel, and M. Zemp. Does the Fornax dwarf spheroidal have a central cusp or core? *MNRAS*, 368(3):1073–1077, May 2006. doi: 10.1111/j.1365-2966.2006.10182.x.

Q. Guo, S. White, C. Li, and M. Boylan-Kolchin. How do galaxies populate dark matter haloes? *MNRAS*, 404(3):1111–1120, May 2010. doi: 10.1111/j.1365-2966.2010.16341.x.

E. Hayashi, J. F. Navarro, J. E. Taylor, J. Stadel, and T. Quinn. The Structural Evolution of Substructure. *ApJ*, 584:541–558, Feb. 2003. doi: 10.1086/345788.

X. Hernandez and G. Gilmore. Dynamical friction in dwarf galaxies. *MNRAS*, 297(2):517–525, June 1998. doi: 10.1046/j.1365-8711.1998.01511.x.

L. Hernquist. An Analytical Model for Spherical Galaxies and Bulges. *ApJ*, 356:359, June 1990. doi: 10.1086/168845.

M. Irwin and D. Hatzidimitriou. Structural parameters for the Galactic dwarf spheroidals. *MNRAS*, 277(4):1354–1378, Dec. 1995. doi: 10.1093/mnras/277.4.1354.

A. P. Ji, A. Frebel, J. D. Simon, and M. Geha. High-resolution Spectroscopy of Extremely Metal-poor Stars in the Least-evolved Galaxies: Bootes II. *ApJ*, 817(1):41, Jan. 2016. doi: 10.3847/0004-637X/817/1/41.

A. P. Ji, S. E. Koposov, T. S. Li, D. Erkal, A. B. Pace, J. D. Simon, V. Belokurov, L. R. Cullinane, G. S. Da Costa, K. Kuehn, G. F. Lewis, D. Mackey, N. Shipp, J. D. Simpson, D. B. Zucker, T. T. Hansen, J. Bland-Hawthorn, and S5 Collaboration. Kinematics of Antlia 2 and Crater 2 from the Southern Stellar Stream Spectroscopic Survey (S^5). *ApJ*, 921(1):32, Nov. 2021. doi: 10.3847/1538-4357/ac1869.

N. Kallivayalil, L. V. Sales, P. Zivick, T. K. Fritz, A. Del Pino, S. T. Sohn, G. Besla, R. P. van der Marel, J. F. Navarro, and E. Sacchi. The Missing Satellites of the Magellanic Clouds? Gaia Proper Motions of the Recently Discovered Ultra-faint Galaxies. *ApJ*, 867(1):19, Nov. 2018. doi: 10.3847/1538-4357/aadfee.

E. N. Kirby, J. G. Cohen, P. Guhathakurta, L. Cheng, J. S. Bullock, and A. Gallazzi. The Universal Stellar Mass-Stellar Metallicity Relation for Dwarf Galaxies. *ApJ*, 779(2):102, Dec. 2013. doi: 10.1088/0004-637X/779/2/102.

A. Koch, M. I. Wilkinson, J. T. Kleyna, M. Irwin, D. B. Zucker, V. Belokurov, G. F. Gilmore, M. Fellhauer, and N. W. Evans. A Spectroscopic Confirmation of the Bootes II Dwarf Spheroidal. *ApJ*, 690(1):453–462, Jan. 2009. doi: 10.1088/0004-637X/690/1/453.

A. Kravtsov. The Dark Matter Annihilation Signal from Dwarf Galaxies and Subhalos. *Advances in Astronomy*, 2010:281913, Jan. 2010. doi: 10.1155/2010/281913.

F. Lelli, S. S. McGaugh, J. M. Schombert, and M. S. Pawlowski. One Law to Rule Them All: The Radial Acceleration Relation of Galaxies. *ApJ*, 836(2):152, Feb. 2017. doi: 10.3847/1538-4357/836/2/152.

Y.-S. Li and S. D. M. White. Masses for the Local Group and the Milky Way. *MNRAS*, 384(4):1459–1468, Mar. 2008. doi: 10.1111/j.1365-2966.2007.12748.x.

A. D. Ludlow, J. F. Navarro, V. Springel, A. Jenkins, C. S. Frenk, and A. Helmi. The Unorthodox Orbits of Substructure Halos. *ApJ*, 692(1):931–941, Feb. 2009. doi: 10.1088/0004-637X/692/1/931.

A. D. Ludlow, S. Bose, R. E. Angulo, L. Wang, W. A. Hellwing, J. F. Navarro, S. Cole, and C. S. Frenk. The mass-concentration-redshift relation of cold and warm dark matter haloes. *MNRAS*, 460(2):1214–1232, Aug. 2016. doi: 10.1093/mnras/stw1046.

A. V. Macciò, J. Frings, T. Buck, C. Penzo, A. A. Dutton, M. Blank, and A. Obreja. The edge of galaxy formation - I. Formation and evolution of MW-satellite analogues before accretion. *MNRAS*, 472(2):2356–2366, Dec. 2017. doi: 10.1093/mnras/stx2048.

A. D. Mackey and G. F. Gilmore. Surface brightness profiles and structural parameters for globular clusters in the Fornax and Sagittarius dwarf spheroidal galaxies. *MNRAS*, 340(1):175–190, Mar. 2003. doi: 10.1046/j.1365-8711.2003.06275.x.

A. W. McConnachie. The Observed Properties of Dwarf Galaxies in and around the Local Group. *AJ*, 144(1):4, July 2012. doi: 10.1088/0004-6256/144/1/4.

A. W. McConnachie and K. A. Venn. Updated Proper Motions for Local Group Dwarf Galaxies Using Gaia Early Data Release 3. *Research Notes of the American Astronomical Society*, 4(12):229, Dec. 2020. doi: 10.3847/2515-5172/abd18b.

S. S. McGaugh. MOND Prediction for the Velocity Dispersion of the "Feeble Giant" Crater II. *ApJ*, 832(1):L8, Nov. 2016. doi: 10.3847/2041-8205/832/1/L8.

P. J. McMillan. Mass models of the Milky Way. *MNRAS*, 414(3):2446–2457, July 2011. doi: 10.1111/j.1365-2966.2011.18564.x.

N. Meadows, J. F. Navarro, I. Santos-Santos, A. Benítez-Llambay, and C. Frenk. Cusp or core? Revisiting the globular cluster timing problem in Fornax. *MNRAS*, 491(3): 3336–3342, Jan. 2020. doi: 10.1093/mnras/stz3280.

M. Miyamoto and R. Nagai. Three-dimensional models for the distribution of mass in galaxies. *PASJ*, 27:533–543, Jan. 1975.

A. G. Moskowitz and M. G. Walker. Stellar Density Profiles of Dwarf Spheroidal Galaxies. *ApJ*, 892(1):27, Mar. 2020. doi: 10.3847/1538-4357/ab7459.

B. P. Moster, T. Naab, and S. D. M. White. Galactic star formation and accretion histories from matching galaxies to dark matter haloes. *MNRAS*, 428(4):3121–3138, Feb. 2013. doi: 10.1093/mnras/sts261.

F. Munshi, A. Brooks, E. Applebaum, C. Christensen, J. P. Sligh, and T. Quinn. Quantifying scatter in galaxy formation at the lowest masses. *arXiv e-prints*, art. arXiv:2101.05822, Jan. 2021.

J. F. Navarro. On the density structure of galaxy merger remnants. *MNRAS*, 242:311–317, Jan. 1990. doi: 10.1093/mnras/242.3.311.

J. F. Navarro, V. R. Eke, and C. S. Frenk. The cores of dwarf galaxy haloes. *MNRAS*, 283 (3):L72–L78, Dec. 1996a. doi: 10.1093/mnras/283.3.L72.

J. F. Navarro, C. S. Frenk, and S. D. M. White. The Structure of Cold Dark Matter Halos. *ApJ*, 462:563, May 1996b. doi: 10.1086/177173.

J. F. Navarro, C. S. Frenk, and S. D. M. White. A Universal Density Profile from Hierarchical Clustering. *ApJ*, 490(2):493–508, Dec. 1997. doi: 10.1086/304888.

C. Nipoti and J. Binney. Early flattening of dark matter cusps in dwarf spheroidal galaxies. *MNRAS*, 446(2):1820–1828, Jan. 2015. doi: 10.1093/mnras/stu2217.

J. Oñorbe, M. Boylan-Kolchin, J. S. Bullock, P. F. Hopkins, D. Kereš, C.-A. Faucher-Giguère, E. Quataert, and N. Murray. Forged in FIRE: cusps, cores and baryons in low-mass dwarf galaxies. *MNRAS*, 454(2):2092–2106, Dec. 2015. doi: 10.1093/mnras/stv2072.

K. S. Oh, D. N. C. Lin, and H. B. Richer. Globular Clusters in the Fornax Dwarf Spheroidal Galaxy. *ApJ*, 531(2):727–738, Mar. 2000. doi: 10.1086/308477.

T. Okamoto and C. S. Frenk. The origin of failed subhaloes and the common mass scale of the Milky Way satellite galaxies. *MNRAS*, 399(1):L174–L178, Oct. 2009. doi: 10.1111/j.1745-3933.2009.00748.x.

K. A. Oman, J. F. Navarro, A. Fattahi, C. S. Frenk, T. Sawala, S. D. M. White, R. Bower, R. A. Crain, M. Furlong, M. Schaller, J. Schaye, and T. Theuns. The unexpected diversity of dwarf galaxy rotation curves. *MNRAS*, 452(4):3650–3665, Oct. 2015. doi: 10.1093/mnras/stv1504.

K. A. Oman, A. Marasco, J. F. Navarro, C. S. Frenk, J. Schaye, and A. Benítez-Llambay. Non-circular motions and the diversity of dwarf galaxy rotation curves. *MNRAS*, 482 (1):821–847, Jan. 2019. doi: 10.1093/mnras/sty2687.

E. Patel, N. Kallivayalil, N. Garavito-Camargo, G. Besla, D. R. Weisz, R. P. van der Marel, M. Boylan-Kolchin, M. S. Pawlowski, and F. A. Gómez. The Orbital Histories of Magellanic Satellites Using Gaia DR2 Proper Motions. *ApJ*, 893(2):121, Apr. 2020. doi: 10.3847/1538-4357/ab7b75.

J. Peñarrubia, J. F. Navarro, and A. W. McConnachie. The Tidal Evolution of Local Group Dwarf Spheroidals. *ApJ*, 673:226–240, Jan. 2008. doi: 10.1086/523686.

J. Peñarrubia, J. F. Navarro, A. W. McConnachie, and N. F. Martin. The Signature of Galactic Tides in Local Group Dwarf Spheroidals. *ApJ*, 698(1):222–232, June 2009. doi: 10.1088/0004-637X/698/1/222.

J. Peñarrubia, A. J. Benson, M. G. Walker, G. Gilmore, A. W. McConnachie, and L. Mayer. The impact of dark matter cusps and cores on the satellite galaxy population around spiral galaxies. *MNRAS*, 406(2):1290–1305, Aug. 2010. doi: 10.1111/j.1365-2966.2010.16762.x.

J. Peñarrubia, A. Pontzen, M. G. Walker, and S. E. Koposov. The Coupling between the Core/Cusp and Missing Satellite Problems. *ApJ*, 759(2):L42, Nov. 2012. doi: 10.1088/2041-8205/759/2/L42.

J. A. Petts, A. Gualandris, and J. I. Read. A semi-analytic dynamical friction model that reproduces core stalling. *MNRAS*, 454(4):3778–3791, Dec. 2015. doi: 10.1093/mnras/stv2235.

S. Piatek, C. Pryor, E. W. Olszewski, H. C. Harris, M. Mateo, D. Minniti, D. G. Monet, H. Morrison, and C. G. Tinney. Proper Motions of Dwarf Spheroidal Galaxies from Hubble Space Telescope Imaging. I. Method and a Preliminary Measurement for Fornax. *AJ*, 124(6):3198–3221, Dec. 2002. doi: 10.1086/344767.

G. Pietrzyński, M. Górski, W. Gieren, V. D. Ivanov, F. Bresolin, and R.-P. Kudritzki. The Araucaria Project. Infrared Tip of the Red Giant Branch Distances to the Carina and Fornax Dwarf Spheroidal Galaxies. *AJ*, 138(2):459–465, Aug. 2009. doi: 10.1088/0004-6256/138/2/459.

Planck Collaboration, P. A. R. Ade, N. Aghanim, M. Arnaud, M. Ashdown, J. Aumont, C. Baccigalupi, A. J. Banday, R. B. Barreiro, J. G. Bartlett, N. Bartolo, E. Battaner, R. Battye, K. Benabed, A. Benoît, A. Benoit-Lévy, J. P. Bernard, M. Bersanelli, P. Bielewicz, J. J. Bock, A. Bonaldi, L. Bonavera, J. R. Bond, J. Borrill, F. R. Bouchet, F. Boulanger, M. Bucher, C. Burigana, R. C. Butler, E. Calabrese, J. F. Cardoso, A. Catalano, A. Challinor, A. Chamballu, R. R. Chary, H. C. Chiang, J. Chluba, P. R. Christensen, S. Church, D. L. Clements, S. Colombi, L. P. L. Colombo, C. Combet, A. Coulais, B. P. Crill, A. Curto, F. Cuttaia, L. Danese, R. D. Davies, R. J. Davis, P. de Bernardis, A. de Rosa, G. de Zotti, J. Delabrouille, F. X. Désert, E. Di Valentino, C. Dickinson, J. M. Diego, K. Dolag, H. Dole, S. Donzelli, O. Doré, M. Douspis, A. Ducout, J. Dunkley, X. Dupac, G. Efstathiou, F. Elsner, T. A. Enßlin, H. K. Eriksen, M. Farhang, J. Fergusson, F. Finelli, O. Forni, M. Frailis, A. A. Fraisse, E. Franceschi, A. Frejsel, S. Galeotta, S. Galli, K. Ganga, C. Gauthier, M. Gerbino, T. Ghosh, M. Giard, Y. Giraud-Héraud, E. Giusarma, E. Gjerløw, J. González-Nuevo, K. M. Górski, S. Gratton, A. Gregorio, A. Gruppuso, J. E. Gudmundsson, J. Hamann, F. K. Hansen, D. Hanson, D. L. Harrison, G. Helou, S. Henrot-Versillé, C. Hernández-Monteagudo, D. Herranz, S. R. Hildebrandt, E. Hivon, M. Hobson, W. A. Holmes, A. Hornstrup, W. Hovest, Z. Huang, K. M. Huffenberger, G. Hurier, A. H. Jaffe, T. R. Jaffe, W. C. Jones, M. Juvela, E. Keihänen, R. Keskitalo, T. S. Kisner,

R. Kneissl, J. Knoche, L. Knox, M. Kunz, H. Kurki-Suonio, G. Lagache, A. Lähteenmäki, J. M. Lamarre, A. Lasenby, M. Lattanzi, C. R. Lawrence, J. P. Leahy, R. Leonardi, J. Lesgourgues, F. Levrier, A. Lewis, M. Liguori, P. B. Lilje, M. Linden-Vørnle, M. López-Caniego, P. M. Lubin, J. F. Macías-Pérez, G. Maggio, D. Maino, N. Mandolesi, A. Mangilli, A. Marchini, M. Maris, P. G. Martin, M. Martinelli, E. Martínez-González, S. Masi, S. Matarrese, P. McGehee, P. R. Meinhold, A. Melchiorri, J. B. Melin, L. Mendes, A. Mennella, M. Migliaccio, M. Millea, S. Mitra, M. A. Miville-Deschênes, A. Moneti, L. Montier, G. Morgante, D. Mortlock, A. Moss, D. Munshi, J. A. Murphy, P. Naselsky, F. Nati, P. Natoli, C. B. Netterfield, H. U. Nørgaard-Nielsen, F. Noviello, D. Novikov, I. Novikov, C. A. Oxborrow, F. Paci, L. Pagano, F. Pajot, R. Paladini, D. Paoletti, B. Partridge, F. Pasian, G. Patanchon, T. J. Pearson, O. Perdereau, L. Perotto, F. Perrotta, V. Pettorino, F. Piacentini, M. Piat, E. Pierpaoli, D. Pietrobon, S. Plaszczynski, E. Pointecouteau, G. Polenta, L. Popa, G. W. Pratt, G. Prézeau, S. Prunet, J. L. Puget, J. P. Rachen, W. T. Reach, R. Rebolo, M. Reinecke, M. Remazeilles, C. Renault, A. Renzi, I. Ristorcelli, G. Rocha, C. Rosset, M. Rossetti, G. Roudier, B. Rouillé d'Orfeuil, M. Rowan-Robinson, J. A. Rubiño-Martín, B. Rusholme, N. Said, V. Salvatelli, L. Salvati, M. Sandri, D. Santos, M. Savelainen, G. Savini, D. Scott, M. D. Seiffert, P. Serra, E. P. S. Shellard, L. D. Spencer, M. Spinelli, V. Stolyarov, R. Stompor, R. Sudiwala, R. Sunyaev, D. Sutton, A. S. Suur-Uski, J. F. Sygnet, J. A. Tauber, L. Terenzi, L. Toffolatti, M. Tomasi, M. Tristram, T. Trombetti, M. Tucci, J. Tuovinen, M. Türler, G. Umana, L. Valenziano, J. Valiviita, F. Van Tent, P. Vielva, F. Villa, L. A. Wade, B. D. Wandelt, I. K. Wehus, M. White, S. D. M. White, A. Wilkinson, D. Yvon, A. Zacchei, and A. Zonca. Planck 2015 results. XIII. Cosmological parameters. *A&A*, 594:A13, Sept. 2016. doi: 10.1051/0004-6361/201525830.

H. C. Plummer. On the problem of distribution in globular star clusters. *MNRAS*, 71: 460–470, Mar. 1911. doi: 10.1093/mnras/71.5.460.

A. Pontzen and F. Governato. How supernova feedback turns dark matter cusps into cores. *MNRAS*, 421:3464–3471, Apr. 2012. doi: 10.1111/j.1365-2966.2012.20571.x.

J. I. Read and G. Gilmore. Mass loss from dwarf spheroidal galaxies: the origins of shallow dark matter cores and exponential surface brightness profiles. *MNRAS*, 356(1):107–124, Jan. 2005a. doi: 10.1111/j.1365-2966.2004.08424.x.

J. I. Read and G. Gilmore. Mass loss from dwarf spheroidal galaxies: the origins of shallow

dark matter cores and exponential surface brightness profiles. *MNRAS*, 356(1):107–124, Jan. 2005b. doi: 10.1111/j.1365-2966.2004.08424.x.

J. I. Read, T. Goerdt, B. Moore, A. P. Pontzen, J. Stadel, and G. Lake. Dynamical friction in constant density cores: a failure of the Chandrasekhar formula. *MNRAS*, 373(4): 1451–1460, Dec. 2006. doi: 10.1111/j.1365-2966.2006.11022.x.

J. I. Read, M. G. Walker, and P. Steger. Dark matter heats up in dwarf galaxies. *MNRAS*, 484(1):1401–1420, Mar. 2019. doi: 10.1093/mnras/sty3404.

T. Ren, A. Kwa, M. Kaplinghat, and H.-B. Yu. Reconciling the Diversity and Uniformity of Galactic Rotation Curves with Self-Interacting Dark Matter. *Physical Review X*, 9 (3):031020, July 2019. doi: 10.1103/PhysRevX.9.031020.

M. Rocha, A. H. G. Peter, J. S. Bullock, M. Kaplinghat, S. Garrison-Kimmel, J. Oñorbe, and L. A. Moustakas. Cosmological simulations with self-interacting dark matter - I. Constant-density cores and substructure. *MNRAS*, 430:81–104, Mar. 2013. doi: 10.1093/mnras/sts514.

L. V. Sales, J. F. Navarro, M. G. Abadi, and M. Steinmetz. Cosmic ménage à trois: the origin of satellite galaxies on extreme orbits. *MNRAS*, 379(4):1475–1483, Aug. 2007. doi: 10.1111/j.1365-2966.2007.12026.x.

O. Sameie, S. Chakrabarti, H.-B. Yu, M. Boylan-Kolchin, M. Vogelsberger, J. Zavala, and L. Hernquist. Simulating the “hidden giant” in cold and self-interacting dark matter models. *arXiv e-prints*, art. arXiv:2006.06681, June 2020. doi: 10.48550/arXiv.2006.06681.

J. L. Sanders, N. W. Evans, and W. Dehnen. Tidal disruption of dwarf spheroidal galaxies: the strange case of Crater II. *MNRAS*, 478:3879–3889, Aug. 2018. doi: 10.1093/mnras/sty1278.

I. M. E. Santos-Santos, A. Fattahi, L. V. Sales, and J. F. Navarro. Magellanic satellites in ΛCDM cosmological hydrodynamical simulations of the Local Group. *arXiv e-prints*, art. arXiv:2011.13500, Nov. 2020a.

I. M. E. Santos-Santos, J. F. Navarro, A. Robertson, A. Benítez-Llambay, K. A. Oman, M. R. Lovell, C. S. Frenk, A. D. Ludlow, A. Fattahi, and A. Ritz. Baryonic clues to the puzzling diversity of dwarf galaxy rotation curves. *MNRAS*, 495(1):58–77, June 2020b. doi: 10.1093/mnras/staa1072.

I. M. E. Santos-Santos, L. V. Sales, A. Fattahi, and J. F. Navarro. Satellite mass functions and the faint end of the galaxy mass-halo mass relation in LCDM. *arXiv e-prints*, art. arXiv:2111.01158, Nov. 2021.

I. M. E. Santos-Santos, J. F. Navarro, and A. McConnachie. The Tucana dwarf spheroidal: a distant backsplash galaxy of M31? *MNRAS*, 520(1):55–62, Mar. 2023. doi: 10.1093/mnras/stad085.

T. Sawala, C. S. Frenk, A. Fattahi, J. F. Navarro, R. G. Bower, R. A. Crain, C. Dalla Vecchia, M. Furlong, J. C. Helly, A. Jenkins, K. A. Oman, M. Schaller, J. Schaye, T. Theuns, J. Trayford, and S. D. M. White. The APOSTLE simulations: solutions to the Local Group's cosmic puzzles. *MNRAS*, 457(2):1931–1943, Apr. 2016. doi: 10.1093/mnras/stw145.

J. Schaye, R. A. Crain, R. G. Bower, M. Furlong, M. Schaller, T. Theuns, C. Dalla Vecchia, C. S. Frenk, I. G. McCarthy, J. C. Helly, A. Jenkins, Y. M. Rosas-Guevara, S. D. M. White, M. Baes, C. M. Booth, P. Camps, J. F. Navarro, Y. Qu, A. Rahmati, T. Sawala, P. A. Thomas, and J. Trayford. The EAGLE project: simulating the evolution and assembly of galaxies and their environments. *MNRAS*, 446(1):521–554, Jan. 2015. doi: 10.1093/mnras/stu2058.

R. Schönrich, J. Binney, and W. Dehnen. Local kinematics and the local standard of rest. *MNRAS*, 403(4):1829–1833, Apr. 2010. doi: 10.1111/j.1365-2966.2010.16253.x.

J. L. Sersic. *Atlas de Galaxias Australes*. 1968.

F. Sestito, J. Roediger, J. F. Navarro, J. Jensen, K. A. Venn, S. E. T. Smith, C. Hayes, and A. W. McConnachie. Stars on the edge: Galactic tides and the outskirts of the Sculptor dwarf spheroidal. *MNRAS*, 523(1):123–131, July 2023. doi: 10.1093/mnras/stad1417.

S. Shao, M. Cautun, C. S. Frenk, M. Reina-Campos, A. J. Deason, R. A. Crain, J. M. D. Kruijssen, and J. Pfeffer. The survival of globular clusters in a cuspy Fornax. *arXiv e-prints*, art. arXiv:2012.08058, Dec. 2020.

J. D. Simon. The Faintest Dwarf Galaxies. *ARA&A*, 57:375–415, Aug. 2019. doi: 10.1146/annurev-astro-091918-104453.

R. S. Somerville. Can Photoionization Squelching Resolve the Substructure Crisis? *ApJ*, 572(1):L23–L26, June 2002. doi: 10.1086/341444.

V. Springel. The cosmological simulation code GADGET-2. *MNRAS*, 364(4):1105–1134, Dec. 2005. doi: 10.1111/j.1365-2966.2005.09655.x.

S. Taibi, G. Battaglia, M. Rejkuba, R. Leaman, N. Kacharov, G. Iorio, P. Jablonka, and M. Zoccali. The Tucana dwarf spheroidal galaxy: not such a massive failure after all. *A&A*, 635:A152, Mar. 2020. doi: 10.1051/0004-6361/201937240.

E. Tollet, A. V. Macciò, A. A. Dutton, G. S. Stinson, L. Wang, C. Penzo, T. A. Gutcke, T. Buck, X. Kang, C. Brook, A. Di Cintio, B. W. Keller, and J. Wadsley. NIHAO - IV: core creation and destruction in dark matter density profiles across cosmic time. *MNRAS*, 456(4):3542–3552, Mar. 2016. doi: 10.1093/mnras/stv2856.

G. Torrealba, S. E. Koposov, V. Belokurov, and M. Irwin. The feeble giant. Discovery of a large and diffuse Milky Way dwarf galaxy in the constellation of Crater. *MNRAS*, 459(3):2370–2378, July 2016. doi: 10.1093/mnras/stw733.

G. Torrealba, V. Belokurov, S. E. Koposov, T. S. Li, M. G. Walker, J. L. Sanders, A. Geringer-Sameth, D. B. Zucker, K. Kuehn, N. W. Evans, and W. Dehnen. The hidden giant: discovery of an enormous Galactic dwarf satellite in Gaia DR2. *MNRAS*, 488(2):2743–2766, Sept. 2019. doi: 10.1093/mnras/stz1624.

S. D. Tremaine. The formation of the nuclei of galaxies. II. The local group. *ApJ*, 203: 345–351, Jan. 1976. doi: 10.1086/154085.

F. C. Van Bosch and G. Ogiya. Dark matter substructure in numerical simulations: a tale of discreteness noise, runaway instabilities, and artificial disruption. *MNRAS*, 475: 4066–4087, Apr. 2018. doi: 10.1093/mnras/sty084.

F. C. Van Bosch, G. Ogiya, O. Hahn, and A. Burkert. Disruption of dark matter substructure: fact or fiction? *MNRAS*, 474:3043–3066, Mar. 2018. doi: 10.1093/mnras/stx2956.

P. G. Van Dokkum, R. Abraham, A. Merritt, J. Zhang, M. Geha, and C. Conroy. Forty-seven Milky Way-sized, Extremely Diffuse Galaxies in the Coma Cluster. *ApJ*, 798(2): L45, Jan. 2015. doi: 10.1088/2041-8205/798/2/L45.

M. Vogelsberger, S. Genel, V. Springel, P. Torrey, D. Sijacki, D. Xu, G. Snyder, D. Nelson, and L. Hernquist. Introducing the Illustris Project: simulating the coevolution of dark and visible matter in the Universe. *MNRAS*, 444(2):1518–1547, Oct. 2014. doi: 10.1093/mnras/stu1536.

M. G. Walker and J. Peñarrubia. A Method for Measuring (Slopes of) the Mass Profiles of Dwarf Spheroidal Galaxies. *ApJ*, 742(1):20, Nov. 2011. doi: 10.1088/0004-637X/742/1/20.

M. G. Walker, M. Mateo, E. W. Olszewski, J. Peñarrubia, N. W. Evans, and G. Gilmore. A Universal Mass Profile for Dwarf Spheroidal Galaxies? *ApJ*, 704(2):1274–1287, Oct. 2009. doi: 10.1088/0004-637X/704/2/1274.

L. Wang, A. A. Dutton, G. S. Stinson, A. V. Macciò, C. Penzo, X. Kang, B. W. Keller, and J. Wadsley. NIHAO project - I. Reproducing the inefficiency of galaxy formation across cosmic time with a large sample of cosmological hydrodynamical simulations. *MNRAS*, 454(1):83–94, Nov. 2015. doi: 10.1093/mnras/stv1937.

M. Y. Wang, T. de Boer, A. Pieres, T. S. Li, A. Drlica-Wagner, S. E. Koposov, A. K. Vivas, A. B. Pace, B. Santiago, A. R. Walker, D. L. Tucker, L. Strigari, J. L. Marshall, B. Yanny, D. L. DePoy, K. Bechtol, A. Roodman, T. M. C. Abbott, F. B. Abdalla, S. Allam, J. Annis, S. Avila, E. Bertin, D. Brooks, D. L. Burke, A. Carnero Rosell, M. Carrasco Kind, C. E. Cunha, C. B. D'Andrea, L. N. da Costa, J. De Vicente, S. Desai, T. F. Eifler, J. Estrada, B. Flaugher, J. Frieman, J. García-Bellido, D. W. Gerdes, D. Gruen, R. A. Gruendl, G. Gutierrez, D. L. Hollowood, K. Honscheid, D. J. James, K. Kuehn, N. Kuropatkin, O. Lahav, M. A. G. Maia, R. Miquel, E. Sanchez, V. Scarpine, I. Sevilla-Noarbe, M. Smith, R. C. Smith, F. Sobreira, E. Suchyta, M. E. C. Swanson, G. Tarle, and DES Collaboration. The Morphology and Structure of Stellar Populations in the Fornax Dwarf Spheroidal Galaxy from Dark Energy Survey Data. *ApJ*, 881(2):118, Aug. 2019. doi: 10.3847/1538-4357/ab31a9.

S. D. M. White and M. J. Rees. Core condensation in heavy halos: a two-stage theory for galaxy formation and clustering. *MNRAS*, 183:341–358, May 1978. doi: 10.1093/mnras/183.3.341.

J. Wolf, G. D. Martinez, J. S. Bullock, M. Kaplinghat, M. Geha, R. R. Muñoz, J. D. Simon, and F. F. Avedo. Accurate masses for dispersion-supported galaxies. *MNRAS*, 406(2):1220–1237, Aug. 2010. doi: 10.1111/j.1365-2966.2010.16753.x.

J. Woo, S. Courteau, and A. Dekel. Scaling relations and the fundamental line of the local group dwarf galaxies. *MNRAS*, 390(4):1453–1469, Nov. 2008. doi: 10.1111/j.1365-2966.2008.13770.x.